Nanostructured materials for sustainable next generation organic solar cells

By

Rorisang Mabindisa

BSc Chemical Science (UWC), BSc (Hons) Chemical Science (UWC)

In fulfillment of the requirement for the degree of

Magister Scientiae in Chemical Science

Faculty of Sciences, University of the Western Cape

Bellville, Cape Town, South Africa

Supervisor: Dr Natasha Ross

Co-supervisor: Prof Wamwangi

November 2022

Acknowledgment

I would like to acknowledge my indebtedness and render my warmest thanks to my supervisor, Dr. Natasha Ross, who made this work possible through her tremendous support. Her friendly guidance and expert advice have been invaluable throughout all stages of the work. I would also wish to express my gratitude to FoodBev SETA for the financial support and extended discussions with my co-supervisor Prof Wamwangi and Dr Ramoroka on valuable suggestions which have contributed greatly to the improvement of the thesis. The thesis has also benefited from comments and suggestions made by Kevin Tambwe who has read through the manuscript. I take this opportunity to thank them. Special thanks are due to my colleagues from the chemistry department, Dr Masande Yalo and Dr Masixole Makhaba for their continuous support and understanding, but also for more concrete things like commenting on earlier versions of the thesis, helping with the figures and the final preparation of the manuscript. My thanks are extended to my parents Makhotso and Moeketsi Mabindisa for supporting me both financially and emotionally during these two years. The person with the greatest indirect contribution to this work is my mother, who has taught me a love of mathematics and science in general. I want to thank her, my siblings, Khotso and Tumelo Mabindisa for their constant encouragement. I finally would like to thank everyone with whom I have worked in the Sensor Lab, Organometallics and Nanoscience group supervised by Prof Onani and Organic A research group supervised by Prof Mabusela for their kindness and support during the completion of my degree.

Cape Town, November 2022, Rorisang Mabindisa

Declaration

I, hereby declare that **"*Nanostructured materials for sustainable next generation organic solar cells*"** is the result of my own work that was done by me under the supervision of Dr. Natasha Ross and co-supervision of Prof Wamwangi, and that it has not been previously submitted for any degree or examination in any other university or higher education; and that all the sources and quotations have been indicated and acknowledged by complete references.

Rorisang Mabindisa November 2022

Signed …… …… Date ……04-11-2022……

Research Output

Publications

[1] **R. Mabindisa**, K. Tambwe, L. McIteka, and N. Ross, "Organic nanostructured materials for sustainable application in next generation solar cells," *Appl. Sci.*, vol. 11, no. 23, 2021, doi: 10.3390/app112311324.

Workshops and Seminars

- ✓ Young chemists' symposium, *Sustainability in Chemistry*, Oral, Flash presentation, and Poster 8 – 9 July 2021, Virtual.
- ✓ Workshop, Division for Postgraduate Studies: Prof Rodney Duffett (CPUT), *PhD by Publication/Thesis by Articles*, 13 July 2021, Virtual.
- ✓ Workshop, Division for Postgraduate Studies, *Digital Literacy Workshops (ICT Packages)*, August – September 2021, Virtual.
- ✓ Seminar, Prof. Esidor Ntsoenzok (CNRS Orleans, France), *Photovoltaics: Perovskite and some innovative thin film silicon and plasmonic approaches*, 10 August 2022, Chemical Science Building, University of the Western Cape, Bellville, South Africa.
- ✓ Seminar, Amanda-Lee Manicum, *XRD and X-ray crystallography and its application to materials characterisation*, 06 July 2022, Chemical Science Building, University of the Western Cape, Bellville, South Africa.
- ✓ Workshop, ACS and ICCE 2022, *How to get published*, Prof Thomas Holme, 15 July 2022, UCT Department of Chemistry, Cape Town, South Africa.
- ✓ Webinar, The South African Grape and Wine Research Institute, Opportunities for graduates in Viticulture, Oenology, Food Science, Plant Pathology, Soil Science Applied Plant Science, 31 August 2022, JH Neethling Building, Room 1003 & Online on Teams.
- ✓ Proposal presentation, Kgabo Philipine Makhado, *Nickel heterojunctions photocatalysts for detoxification of pharmaceutical wastewater contaminated by antibiotics*, 30 August 2022, Chemical Science Building, University of the Western Cape, Bellville, South Africa.
- ✓ 44th South African Chemical Institute National Convention, chemistry for sustainable development in Africa, conference, Stellenbosch University (SU), 9-13 January 2023, Western Cape, South Africa.

Trainings

- ✓ Training, *Experience the Latest in Particle Characterization*, Polymer Science Building, 08 June 2022, De Beer Street, Stellenbosch, 7600
- ✓ Rheo Bootcamp - *Back to Basics*, Polymer Science Building, 09 June 2022, De Beer Street, Stellenbosch, 7600, South Africa.
- ✓ Training, *Microwave (Multiwave PRO)*, Anton Paar, 29 September 2022, Chemical Science Building, University of the Western Cape, Bellville, South Africa.

List of Abbreviations

AFM – Atomic Force Microscopy

BDTOEHSn – 4,8-Bis[(2-ethylhexyl)oxy]-2,6-bis(trimethylstannyl)benzo[1,2-b:4,5-b'] dithiophene

CV – Cyclic Voltammetry

D18 – Poly[(2,6-(4,8-bis(5-(2-ethylhexyl-3-fluoro)thiophen-2-yl)-benzo[1,2-b:4,5-b']dithiophene))-alt-5,5'-(5,8-bis(4-(2-butyloctyl)thiophen-2-yl)dithieno[3',2':3,4;2",3":5,6] benzo[1,2-c][1,2,5]thiadiazole)]

DSSCs – Dye-sensitized Solar Cells

DTBT-2Th48Br – 5,8-bis(5-bromo-4-(2-butyloctyl)thiophen-2-yl)dithieno[3',2':3,4;2",3":5,6] benzo[1,2-c][1,2,5]thiadiazole

EIS – Electrochemical Impedance Spectroscopy

FTIR – Fourier-transform infrared spectroscopy

IDIC – 2,2'-((2Z,2'Z)-((4,4,9,9- tetrahexyl-4,9-dihydro-s-indaceno[1,2-b:5,6-b']dithiophene-2,7-diyl)bis(methanylylidene)) bis(3-oxo-2,3-dihydro-1H-indene-2,1-diylidene) dimalononitrile

ITIC – 3,9-bis(2- methylene-(3-(1,1-dicyanomethylene)-indanone))-5,5,11,11-tetrakis(4-hexylphenyl)- dithieno[2,3-d:2',3'-d']-s-indaceno[1,2-b:5,6-b']dithiophene

IT-4F – 3,9-bis(2-methylene-((3-(1,1-dicyanomethylene)-6,7- difluoro)-indanone))-5,5,11,11-tetrakis(4-hexylphenyl)-dithieno[2,3-d:2',3'-d']-sindaceno[1,2-b:5,6-b']dithiophene

J_{SC} – Short-circuit current

NMR – Nuclear Magnetic Resonance

O-IDTBR – 5Z,5'Z)-5,5'-((7,7'- (4,4,9,9-tetraoctyl-4,9-dihydro-s-indaceno[1,2-b:5,6-b']dithiophene-2,7- diyl)bis(benzo[c][1,2,5]thiadiazole-7,4-diyl))bis(methanylylidene))bis(3-ethyl-2-thioxothiazolidin-4-one

OPVs – Organic Photovoltaic Cells

PCE – Power Conversion Efficiency

$Pd(PPh_3)_4$ – Tetrakis(triphenylphosphine)palladium(0)

PEDOT:PSS – poly(3,4-ethylenedioxythiophene) polystyrene sulfonate

PL – Photoluminescence Spectroscopy

PSCs – Perovskites Solar Cells

PV – Photovoltaic Cells

SEM – Scanning Electron Microscope

SWV – Square Wave Voltammetry

TEM – Transmission Electron Microscopy

TGA – Thermogravimetric Analysis

TTP-TTI – Thienothienopyrrolo-thienothienoindole

UV-Vis – Ultraviolet–Visible spectroscopy

Voc – Open-circuit voltage

XRD – X-ray Diffraction

Y6 – 2,2'-((2Z,2'Z)-((12,13-bis(2-ethylhexyl)-3,9- diundecyl-12,13-dihydro-[1,2,5] thiadiazolo[3,4-e]thieno[2",3'':4',5']thieno[2',3':4,5]pyrrolo[3,2-g]thieno[2',3':4,5]thieno[3,2-b]indole-2,10-diyl)bis(methanylylidene))bis(5,6-difluoro-3-oxo-2,3-dihydro-1H-indene-2,1-diylidene))dimalononitrile

Keywords

Solar energy

Photovoltaic cells

Organic photovoltaic cells

D18 donor

Bandgap

Stille coupling

Electron-Hole pair

Recombination processes

J-V characteristics

Power conversion efficiency

Abstract

Many researchers are conducting their studies that are centred on using solar energy to generate electricity due to the developing interest in solar energy. One of the most promising options to reduce the cost of manufacturing photovoltaic cells and increase power conversion efficiency in the framework of solar energy is hybrid photovoltaics, which combines organic molecules and nanomaterials. Photovoltaic cells become significant in this regard. Most of the commercially accessible photovoltaic cells currently are made of inorganic materials, which are expensive to produce and include harmful compounds. Because of these factors, organic photovoltaic cells have an advantage over their inorganic counterparts. In this research project, we concentrated on synthesising new donor nanostructured materials for use in organic photovoltaic cells. A range of characterisation techniques were used to confirm and analyse the compounds that are commercially available with the newly as-synthesised compound.

The successful synthesis of the nanostructured polymer material was carried out using the Stille coupling reaction and thereafter, it was confirmed with NMR, FTIR and XRD. The morphological analysis was studied using AFM, SEM and TEM. Flake-like structures with a cubic shape were confirmed by SEM images. The optical information about this novel donor nanostructured material was obtained using UV-Vis and PL, which the information about the band gap and quenching effect was confirmed by linking it to the information about HOMO and LUMO levels of the donor nanomaterial. The active layer was comprised of D18-RM donor and Y6 acceptor as a bulk heterojunction. Electrochemical bandgap of the the active layer was determined onset and found to be 2.24 and 1.57 eV respectively. The electrochemical techniques CV, SWV, EIS and Tafel plot analysis were employed to obtain the electrochemical properties of the synthesized polymer and the fabricated device. The thermal stability and viscosity properties were investigated using TGA and Rheological studies respectively. The OPV device was built outside glovebox using Sol-gel method, where the active layer was made up of a bulk heterojunction of donor D18-RM and acceptor Y6. The J-V characteristics were used to study the photovoltaic performance of the fabricated device. The maximum performance of the device gave PCE of 0.0022%, short circuit current (J_{SC}) of 21.04 mA/cm^2, fill factor (FF) of 27.7% and open circuit voltage (V_{OC}) of 0.024 V.

Although the outcomes of this project are not what was hypothetically anticipated in terms of improved efficiency, they have a promising potential of making the dream of implementing OPVs commercially come through. The morphological, electrochemical and photovoltaic analysis proved that the fabricated device that is made up of active layer D18-RM:Y6 has a great potential of breaking through in the future, however, there is still room for improvement for this device.

Table of Contents

List of Figures

List of Schemes

List of Tables

Chapter 1 – Introduction

This chapter provides a brief background information about the photovoltaic cells that discuss the problems faced by the current research and implementation into renewable energy and photovoltaic technologies. The motivation of the reasons behind the interest to pursue this specific field of work, a detailed information about photovoltaics is also laid out. The aims and objectives of this project are stated before the research framework and the thesis synopsis which gives a summary of the chapters is also provided.

1.1. Introduction

One of the most pressing concerns for human living in the twenty-first century is energy [1]. With the human population ever increasing globally, the economic costs of energy are also shooting up dramatically and the demand for sustainable renewable energy rises drastically around the world. By 2040, it is expected that the worldwide energy consumption would have increased by 50% [2]. According to Congcong and co, 80 percent of the world's energy comes from fossil fuels [3]. This heavy dependence on fossil fuels is associated with catastrophic disadvantages to the environment. Among these are greenhouse gases (GHGs) and chlorofluorocarbons (CFCs) which are the main sources of global warming. **Figure 1.1** below shows the smoke and steam that remains in the atmosphere in early mornings after business days in urban areas.

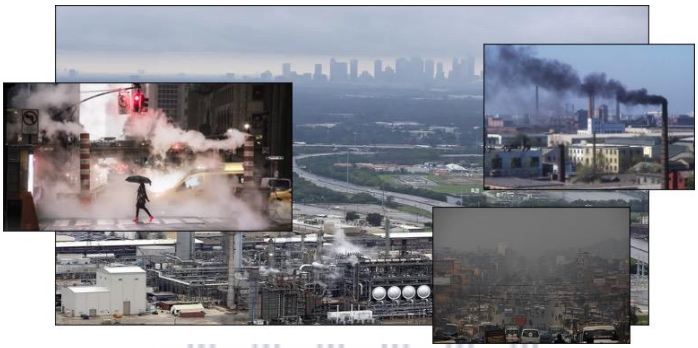

Figure 1.1 Combustion power plants and engines emitting smoke and steam to the atmosphere [4].

1.2. Realizable future of renewable energy

Renewable energy technology is currently one of the world's fastest-growing sectors, with the goal of meeting future energy demands while also addressing environmental issues and helping to mitigate climate change [5]. The development of clean, renewable energy sources that can replace conventional fossil fuels has become a necessity as the world as a whole is severely impacted by the issues of global warming and environmental pollution. Renewable energy sources like water, wind, and solar power are the best alternatives to address the world's ever-increasing energy demand. Leaving environmental concerns aside, it is critical to recognize that fossil fuels are scarce resources and cannot sustain the expanding energy demands of the global economy for much longer.

If the rising energy demand is not satisfied by alternative energy sources, the world's supplies of coal are anticipated to run out by the turn of the century, while those of oil and gas are predicted to run out within a few decades [6]. Renewable resources with no pollution are becoming more and more important. The quantity of renewable energy that can be harvested is, in theoretically, numerous orders of size greater than the energy that people use now. It is a well-worn adage that the quantity of sunshine

that enters the planet Earth in a single hour is sufficient to fuel the global economy for a whole year. The capacity, however, is only a small portion of that. Practical terms, sustainable energy must be cost-competitive with energy obtained from traditional sources in order to be completely adopted.

1.3. Problem statement

The fact that sources of renewable energy need highly specific areas to generate the required quantity of energy, as opposed to non-renewable energy sources like gas, coal, and oil, is a significant problem that arises from the use of renewable energy. Every renewable energy source has its drawbacks; for example, hydroelectricity is only available in certain parts of the world and is frequently concentrated in remote locations, making it expensive to transfer it to users. It also leaves a significant environmental impact because it relies heavily on precipitation and necessitates flooding vast tracts of land. Then again, the amount of geothermal, wave and biomass energy [7] theoretically available for harvesting is too little to realistically contribute a significant share into a global energy mix. This leaves wind and solar energy as the main contenders to substitute the fossil-fuel energy production and to satisfy the rising energy demand.

Despite being relatively expensive, they do have several drawbacks, including the fact that wind and sunshine are not constant sources of energy. Consequently, a power system that incorporates a significant quantity of wind and solar electricity will ultimately need to include storage space, a big amount of extra capacity that is backed up by traditional power plants, or a highly effective method of redistributing energy between remote places. But besides this, if wind and solar energy are combined, they will probably be able to provide the majority of the world's energy needs in the future. In this project, solar photovoltaics (PVs), which turn sunlight directly into electricity, are the primary energy conversion mechanism. These are silicon-free since there are further problems with the silicon-based PVs, these include cost of installation, weather dependence, environmental friendliness etc [8]. OPVs that are seen as alternatives still face, stability, environmentally benign solvents, large-scale printing, limited absorption

1.4. Rationale

Using nanostructured material for photovoltaics, harvesting solar energy has a lot of promise, but large-scale implementation has ran into a lot of roadblocks, the most significant ones are the high cost of technology, environmental instability [9], and low power conversion efficiencies [10]. Solar energy is the most plentiful, unlimited, and clean of all existing renewable energy sources, and because of that, researchers have designed photovoltaic cells to harvest this clean energy. One of the most important resources on earth is the sun, which supplies the energy needed for life to exist and develop. The purpose of solar cells, commonly referred to as photovoltaic cells (PV cells), is to collect solar energy

and transform it into useful energy. One of the main solar energy methods uses PV cells, which use photoelectric devices whose electrical characteristics, such as current, voltage, or resistance, change when subjected to radiation from the sun, to convert solar light gathered from the sun directly into electricity [11].

These devices need to accomplish mainly two tasks: photo-generation of charge carriers (electrons and holes) in a light-absorbing material, and separation of the charge carriers to a conductive contact that will transmit the electricity. This conversion is called the photovoltaic effect [12]. These solar devices are regarded as one of the main technologies towards a sustainable energy generation. Solar collectors can be used for a variety of purposes, but as was already noted, power generation is the most typical one. A solar cell may produce a current by trapping solar radiation, and this current is often fed into the electrical grid. A solar cell's primary role is to use sunlight to absorb photons. The absorber layer is constructed out of a semiconductor. The material's composition permits free electron flow as energy is applied.

Based on their band gaps the energy difference between an excited electron and an electron in its low energy state, certain materials are chosen for these layers. To guarantee that an electron will achieve a particular energy level when exposed to sunlight, the band gaps must be carefully chosen. More conductor layers are required to transport excited electrons out of the cell once they have reached a higher energy state. The electrons can leave the original layer through one layer, and the remaining positive charge, or "hole" for easier illustration, can also leave the original layer through the other layer. The output current that produces usable electrical power is produced by the interaction of moving electrons and holes. The electrical conductivity is essential for supplying enough current since these layers are conductors. One must be cautious to take into account the change in conductivity as both temperature and shape, which changes the cross-sectional region of a solar cell depending on the application [13].

1.5. Thesis Synopsis

The work of this project is based on the development of new OPV material that is polymer-based, with non-fullerenes type being the choice of interest due to their favorable characteristics, highly motivated by the ever-increasing attention of developing an improved power conversion efficiency of OPVs. Recent efforts have achieved quite remarkable power conversion efficiencies highlighting the potential of OPVs for large-scale commercial applications.

1.6. Aims and objectives

1.6.1. Aims:

a) This project aimed to develop a sustainable and cost-effective organic photovoltaic cell that is made up of nanostructured organic material.

b) The project was designed to address the issue of high costs and low efficiencies of conventional silicon-based photovoltaic cells thereby providing green synthetic method, suitable characterization techniques and the fabrication process.

1.6.2. Objectives:

- Synthesize a novel D18 derivative polymer using the Stille coupling reaction.
- Characterize the polymer using NMR for confirmation of the chemical structure and FTIR for active bonding configurations to further confirm the chemical structure.
- Study the morphological properties of the synthesized polymer using the following techniques, HR-SEM and AFM for surface morphology, HR-TEM for particle size distribution, XRD for crystallinity.
- Analyse the optical characteristics using UV-Vis and PL for absorbance and emission spectroscopy respectively.
- Measure the electrochemical properties using CV and EIS.
- Study the photovoltaic performance through application of the synthesized material using I-V curve measurements.

1.7. Research framework

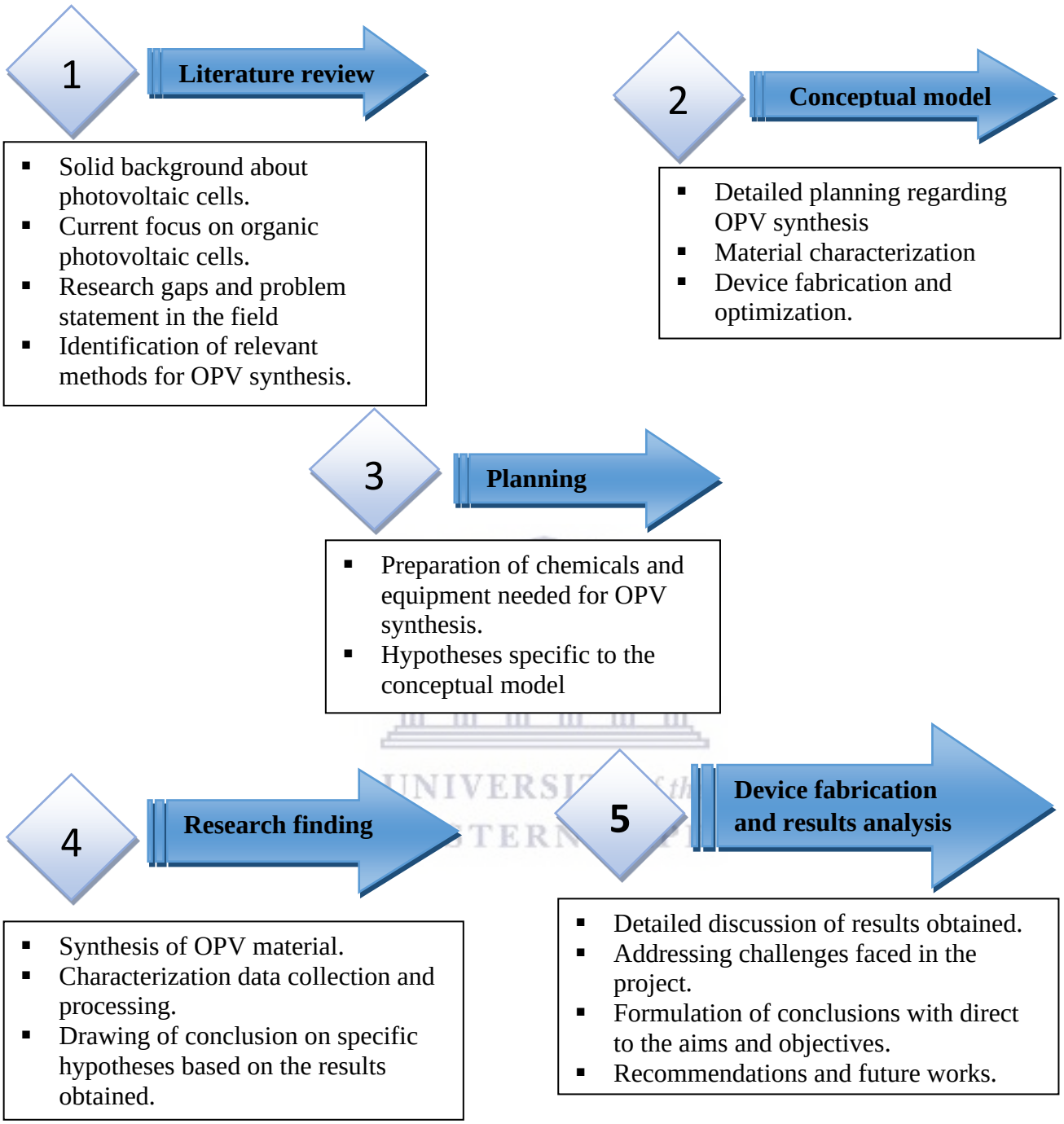

Scheme S 1-1 Research framework with detailed information of the project.

1.8. Thesis Outline

The research is essentially focused on the synthesis of donor nanomaterials and the application of various device characterization techniques to assess the morphology, chemical and physical characteristics, as well as the photovoltaic efficiency, of organic photovoltaic cells.

In **Chapter 1**, a thorough explanation of the motivations for research and development in photovoltaic and renewable energy technologies is provided. Particularly, background information on organic photovoltaic cells is provided, and the structural layout of the device and the cells' principle of operation are also covered. Finally, the project's aims, objectives and research framework are described.

In **Chapter 2**, an overview of photovoltaics, a background explanation of the theory underlying photovoltaic cells and how they work, a description of organic solar cells' characteristics, device architecture, and operational principle, as well as a list of issues related to organic photovoltaics, are provided. Further discussion is given on the various ways that organic photovoltaic films are made, as well as the various deposition techniques that are employed for maximum efficiency. The primary method for characterizing and evaluating photovoltaic cells is explained in the closing chapter.

In **Chapter 3**, following a list of all the materials and characterization tools used in this experiment, specific fabrication specifications for both donor and acceptor materials are provided. Along with extensive descriptions of the acceptor and device characterization methodologies, comprehensive solar cell characterization techniques are also offered.

In **Chapter 4**, results from the various characterization techniques used are presented together with their analysis and discussion. Detailed explanation of the equipment and set up used for the characterization techniques included ^{1}H NMR, C-13 NMR, AFM, PL, FTIR, UV-Vis, CV and I-V curve measurements. The most important conclusions made were based on calculated photovoltaic parameters.

In **Chapter 5**, The findings of the research conducted for this thesis are summarized. Recommendations are made regarding some of the goals that were not achieved and the best course of action for enhancing the outcomes of the J-V measurements of photovoltaic cells.

1.9. References

[1] A. Sharma, D. Pathak, and T. Wagner, "Organic photovoltaic materials: A review on synthesis, structure and properties," *J. Optoelectron. Adv. Mater.*, vol. 16, no. 11–12, pp. 1257–1268, 2014.

[2] D. Snoke, S. Denev, Y. Liu, L. N. Pfeiffer, and K. West, "Letters To Nature," *Nature*, vol. 418, no. August, pp. 754–757, 2002.

[3] C. Wu *et al.*, "Multifunctional nanostructured materials for next generation photovoltaics," *Nano Energy*, vol. 70, no. January, 2020, doi: 10.1016/j.nanoen.2020.104480.

[4] D. J. Phillip, "Fossil fuels are bad for your health and harmful in many ways besides climate change," *The conversation*. p. 1, 2019.

[5] T. Zhang and H. Yang, *High efficiency plants and building integrated renewable energy systems: Building-integrated photovoltaics (BIPV)*. 2018. doi: 10.1016/B978-0-12-812817-6.00040-1.

[6] K. Holmberg and A. Erdemir, "Influence of tribology on global energy consumption, costs and emissions," *Friction*, vol. 5, no. 3, pp. 263–284, 2017, doi: 10.1007/s40544-017-0183-5.

[7] M. Saghir, S. Zafar, A. Tahir, M. Ouadi, B. Siddique, and A. Hornung, "Unlocking the potential of biomass energy in Pakistan," *Front. Energy Res.*, vol. 7, no. MAR, pp. 1–18, 2019, doi: 10.3389/fenrg.2019.00024.

[8] G. S. Alzahrani, F. S. Alzahrani, and A. M. Nahhas, "Study of the Specific Factors Effecting the PV Solar Cell's Efficiency in Saudi Arabia," *Sustain. Energy, Vol. 8, 2020, Pages 6-11*, vol. 8, no. 1, pp. 6–11, 2020, doi: 10.12691/rse-8-1-2.

[9] E. M. Speller *et al.*, "Toward improved environmental stability of polymer: Fullerene and polymer:Nonfullerene organic solar cells: A common energetic origin of light- A nd oxygen-induced degradation," *ACS Energy Lett.*, vol. 4, no. 4, pp. 846–852, 2019, doi: 10.1021/acsenergylett.9b00109.

[10] J. J. Yoo *et al.*, "An interface stabilized perovskite solar cell with high stabilized efficiency and low voltage loss," *Energy Environ. Sci.*, vol. 12, no. 7, pp. 2192–2199, 2019, doi: 10.1039/c9ee00751b.

[11] C. Xiang *et al.*, "A solar tube: Efficiently converting sunlight into electricity and heat," *Nano Energy*, vol. 55, no. November 2018, pp. 269–276, 2019, doi: 10.1016/j.nanoen.2018.10.077.

[12] D. Li *et al.*, "Unprecedented Self-Powered Visible-Infrared Dual-Modal Photodetection

Induced by a Bulk Photovoltaic Effect in a Polar Perovskite," *ACS Appl. Mater. Interfaces*, vol. 14, no. 4, pp. 5608–5614, 2022, doi: 10.1021/acsami.1c21262.

[13] A. A. Akl, S. A. Mahmoud, S. M. AL-Shomar, and A. S. Hassanien, "Improving microstructural properties and minimizing crystal imperfections of nanocrystalline Cu2O thin films of different solution molarities for solar cell applications," *Mater. Sci. Semicond. Process.*, vol. 74, no. October 2017, pp. 183–192, 2018, doi: 10.1016/j.mssp.2017.10.007.

Chapter 2 – Literature review

This chapter summarizes the theory and literature already done behind organic photovoltaic solar cells. First, an overview of sustainability of the existing photovoltaic cells is summarized, followed by a definition of organic photovoltaic cells, their optical, chemical, and photovoltaic characteristics, device architecture, working principle and then some challenges are also enumerated. The recent fabrication processes of donor materials are then described, together with the different deposition method used for optimal efficiencies. Finally, the main techniques for the evaluation and the characterization of the active layer are described.

2.1. Overview of existing photovoltaics

The energy supplied on the earth by the solar radiation in the form of photons is an efficient and feasible source to harvest and convert into electricity. Photovoltaic cells are designed to convert solar energy directly into electrical energy, which is a promising alternative option to conventional fossil fuels that have potential to meet the entire world's energy demand [1]. The PV devices can be divided into three categories. (1) First generation solar cell, (2) second generation solar cell and (3) third generation photovoltaic cell frequently also termed as emerging future generation photovoltaic cells [2]. First generation solar cell mainly consists of silicon (Si) wafers (monocrystalline and polycrystalline). The monocrystalline Si homo-junction and heterojunction cells have 25.1% and 25.6% efficiencies in that order, whereas the polycrystalline Si cells have 20.8% efficiency [3].

The highest efficiency of silicon-based single junction solar cells (lack of non-radiative recombination) is limited to 33.5% for AM1.5G spectrum at 25 °C and is known as Shockley Queisser (SQ) limit under thermodynamic analysis of detailed balancing [4]. Two common terrestrial sun spectrum irradiance spectra are described by the AM 1.5 Standard Spectrum. The two spectra define a standard total (global, hemispherical, within a 2 steradian field of view of the inclined plane at 38° from horizontal) and a standard direct normal spectral irradiance of radiation [5]. At present, silicon solar cells (wafer technology) dominate and take up to 93% of the global PV installation market with power conversion efficiency (PCE) of commercial modules of around 20% and lifetime of around 20 years [6]. The cost of silicon modules was reduced significantly from around 70$/WP in 1970s [7] to ~0.36 $/WP in 2017 [8]. **Figure 2.1** shows the global cumulative photovoltaic installations from 2010 to 2019 [9].

The main challenge, though, is that Si technology demands costly components and greater processing temperatures, making the fabrication relatively expensive [10]. The construction of second-generation solar cells relies on "thin film" technology, which uses semiconductors with promising efficiencies as poly-crystalline cadmium telluride (CdTe-21.5%), single crystalline gallium arsenide (GaAs-28.8%), and copper indium gallium diselenide (CIGS-21.7%) [5]. Multi-junction solar cells exceed SQ limit due to several absorber layers for harvesting light in different regions of the solar spectrum and have reached highest PCE of 38.8% under one sun condition with a five junction (GaInAs/GaInP/GaAs/AlGaInAs/AlGaInP) tandem geometry [11].

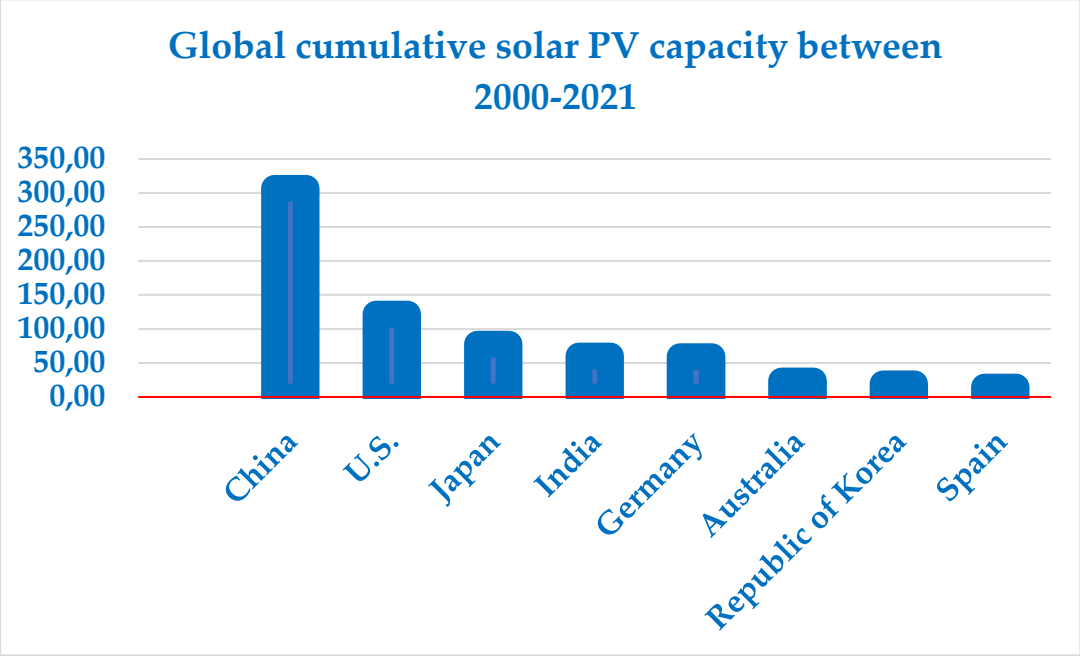

Figure 2.1 Cumulative photovoltaic installations from 2010 to 2019 [12].

Nevertheless, a big challenge for the PV community with these solar cells is the elevated manufacturing cost [5]. The second generation includes solar cells with even lower efficiency but reduced production costs (such as tin-thin film and Cadmium Telluride (CdTe) solar cells), resulting in lower cost per watt than first-generation cells. N. Oulmi and co. synthesized and characterized polycrystalline copper indium gallium selenide (CIGS) thin films using close-spaced vapor transport (CSVT) technique onto two different substrates namely SLG and SLG/FTO. Their area of interest was in the investigations of structural and electrical properties of CIGS1 and CIGS2 thin films. XRD spectra revealed that the films had a polycrystalline structure with a preferential orientation in the (112) plane.

In addition, the slight shift of the peaks towards lower angles they attributed to the slight energy bandgap variation. Furthermore, they reported that high-temperature range, the mobility of their two thin films increased, due to the predominant lattice scattering (phonons) mechanism. While, at low-temperature range, they obtained mobility average values of about 1.83 cm^2/Vs and 1.77 cm^2/Vs for CIGS1 and CIGS2, respectively. Th decrease in mobility they assigned mainly to the involved impurity scattering [13]. According to Green et al., CdTe has achieved similar efficiencies to CIGS. It also has a band gap close to ideal at 1.43eV, with advantages including good absorption and low energy losses. CdTe solar cells can be made through low-temperature processes, allowing flexible and affordable

production (as with OPVs) - which is preferable too expensive and time-consuming high-temperature processes.

CdTe currently has the largest market share of all thin-film technologies. However, cadmium is toxic, and tellurium is particularly rare (being 300,000,000 times less abundant than silicon). These factors may point to potential issues with long-term, large-scale production in future. However, there has been some introduction of CdTe PV recycling by manufacturers [14].

Researchers have pushed towards new types of solar cells and developed 'third generation' photovoltaic cells to overcome the limitations of the preceding solar cells and tried to decrease high production cost [4]. Even though, the efficiencies of third generation solar cells are relatively low as compared to Si/multi-junction and thin film based-solar cells, in terms of component toxicity and natural abundance, OPVs are advantageous compared to Si and CdTe PVs. They have low production cost due to cheap fabrication processing techniques. This makes third generation solar cells interesting to the PV community, so far the highest PCE for OPVs is 18% [15] and this shows that there's still a room for improvement.

Fairly recently, solution processed organic photovoltaics have started to attract major interest owing to their high-power conversion efficiency (PCE), cost effective fabrication, and added functionality such as flexibility, being aesthetic and light weight. In 1991, Kakiage et al produced the first development based on dye-sensitize solar cells (DSSCs) [16], which now demonstrate 14.3% efficiency [17]. The most recent advance in the field of third generation solar cells is the development of organic-inorganic halide perovskite solar cells that now demonstrate efficiencies of about 22% [18]. According to Yang et al. advancement of perovskite solar cells has been remarkable as these can be fabricated by solution processing at low temperatures and the production requires less energy than Si solar cell.

Coupling of PSCs with c-Si and/or CIGS solar cells in tandem geometry is considered a novel approach in order to reduce the overall cost of energy generation (cost-efficiency balance) and also to enhance the PCE of single junction solar cells beyond the SQ limit. Tandem solar cells is possible to be fabricated in three different ways: (1) Mechanically stacked solar cells, termed as 4-terminal (4T), (2) Monolithic solar cells, termed as 2-terminal (2T) and (3) optical splitting tandem solar cell [19]. Recently, 26.4% PCE has been reported by Duong et al. with mechanically stacked configuration [20]. A focus on tandem devices is due to their easy integration and printability on existing PV technology,

as PSCs can easily be printed via solution processing techniques. A possible additional market advantage of the PSCs is the use of flexible PV technology.

It is not only attracting a lot of attention due to the search for low-cost manufacturing and high throughput but also by taking into account its properties of being lightweight, flexible and thin, that would make it easy to integrate on any surface (e.g. building integrated photovoltaics (BIPV), automotive integrated photovoltaics (AIPV)) or structure (either curved, rigid, or flexible) and even in portable and indoor electronics [21]. Notwithstanding the high efficiency accounts, the PSCs still face issues such as: long-term operational stability, toxicity (the most efficient devices employ lead, Pb), and reproducibility. The reproducibility of the performance arises from their rapid crystallization, which largely depends on the fabrication conditions and also the substrate or the selective contacts below them [22].

For a highly efficient device, the choice of selective contacts is important for effective charge extractions as well as its stability as perovskite deposition on metal oxides such as ZnO and TiO_2 has displayed degradation problems due to a possible interfacial reaction [23]. Based on various favourable properties, organic solar devices have the capacity to overcome the difficulties faced by silicon-based and organic-inorganic hybrid solar cells [24]. The purpose of this project is to address some of the barriers behind high-cost traditional silicon-based photovoltaic solar cells and recent innovations in low-cost nanostructured organic photovoltaics.

2.2. Types of photovoltaic cells

Up until recently, solar cells are split into three primary kinds known as generations [25]. Solar cells of the first generation are highly expensive to develop (single crystal, multi crystal solar cells, etc.) and have a poor efficiency. The second generation includes solar cells with even lower efficiency but reduced production costs (such as tin-thin film and Cadmium Telluride (CdTe) solar cells), resulting in lower cost per watt than first generation cells. Next-generation photovoltaic solar cells, popularly known as "third generation PVs," are low-cost but high-performance solar cells [26]. Simple production, minimal cost, and high performance are the major characteristics of these emerging solar cells. Additional advantages like flexibility and lightweight may promote new applications including portable power, interior light harvesters, and solar wings for drones [27].

There are four main types of emerging solar cells which seem to address the roadblocks towards large-scale implementation of solar cells, these emerging solar cells are organic photovoltaics perovskites (PSCs) [28] dye-sensitized (DSSCs) [29] and organic-inorganic hybrids solar cells [30] organic photovoltaic cells (OPVs)[31]. Before these technologies could emerge, solid-state silicon solar cells have been the primary driving factor in photovoltaic technology for a few decades due to silicon being relatively abundant, environmentally benign, having good material quality and the widespread technological know-how [14].

However, because solid-state silicon solar cells are fragile and tight, they are not suitable for transportation. Another problem is that the components are still quite expensive when compared to some of the other solar technology alternatives. Nonetheless, technological advancements are gradually permitting the use of lower-cost but lower-quality silicon. As a result, silicon solar cells are becoming more inexpensive, particularly with government subsidies. Therefore, it is worth further investigation which could result in new breakthroughs for solid-state photovoltaic solar cells.

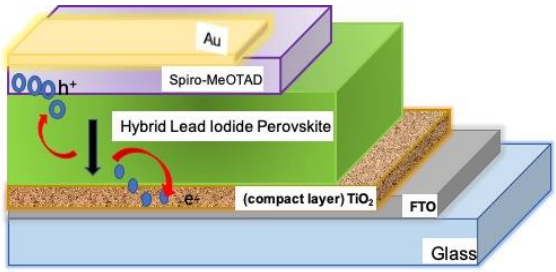

Figure 2.2 Illustration of charge transfer process in a hybrid organic-inorganic solar cell

Moreover, other disadvantages of crystalline silicon is that its electronic band gap is indirect in nature, making it a poor absorber of long wavelength sunlight [32]. Because of their high absorption coefficient, great carrier mobility, and easily adjustable band gaps. The stability of PSCs has attracted much well-deserved attention of late, and notable progress has been made in the past few years. PSCs

have recently exhibited lifetimes of 10,000 hours under 1 sun (1 kW/m^2) illumination with an ultraviolet filter at a stabilized temperature of 55°C and at short-circuit conditions for a printable triple mesoscopic PSC. This irradiation is equivalent to the total irradiation of 10 years of outdoor use in most of Europe.

However, within the PSC community, standard testing protocols require further development. In addition, transparency in reporting standards on stability tests needs to be improved. Dye-sensitized solar cells (DSSCs) belong to the group of thin-film solar cells which have been under extensive research for more than two decades due to their low cost, simple preparation methodology, low toxicity and ease of production. Still, there is lot of scope for the replacement of current DSSC materials due to their high cost, less abundance, and long-term stability. The efficiency of existing DSSCs reaches up to 12%, using Ru(II) dyes by optimizing material and structural properties which is still less than the efficiency offered by first- and second-generation solar cells [33]. Organic–inorganic hybrid solar cells (**Figure 2.2**) have arisen amongst the most promising light absorber layers essential for next-generation solar cells. They are multi-component molecules with at least one organic (typically the polymer) or inorganic material in the nanometre scale size domain, and they usually have substantially better performance than their non-hybrid counterparts.

However, organic cations' thermal and moisture sensitivity in the hybrid remains the major source of device instability [34]. The lateral charge transfer between the organic and inorganic layers is highly curtailed in a hybrid, but the active perpendicular layer orientation is thought to enable charge passage along the inorganic sheets to the substrates, as illustrated in **Figure 2** [35]. Based on various favourable properties, organic solar devices have the capacity to overcome the difficulties faced by silicon-based and organic-inorganic hybrid solar cells [24]. With this in mind, the purpose of this review is to highlight some of the barriers behind high-cost traditional silicon-based photovoltaic solar cells and recent innovations in low-cost nanostructured organic photovoltaics.

2.3. Organic photovoltaic cells

Organic photovoltaic materials primarily consist of conjugated small molecules and polymers. Organic photovoltaic devices based on semiconducting conjugated polymers have emerged as a viable alternative to traditional solid-state (silicon-based) solar systems, primarily due to their affordable production costs [36] for soluble organic molecules (produced via roll-to-roll processing techniques), abundant material (decreasing the supply and price constraints) as well as flexible substrates [37] (permitting a wide variety of uses). They cleared the path for Tang to claim in 1986 that he had developed the first thin film OSC that exceeded 1% efficiency. Despite the fact that they attracted a lot of interest for their ability to generate energy effectively even under dispersed light or interior illumination, solid-state dye-sensitized photovoltaic cells (DSSCs) still have low power conversion efficiency (11%) which still has to be improved [30].

Moreover, the light electrolyte causes a safety issue since the iodine and organic solvents can be volatized and leak, [30] affecting the cell's longevity. The all-solid perovskite solar cells counterparts, which are based on DSSC but overcomes DSSC's limitations, received a lot of interest from scientists as soon as they were disclosed. Despite the fact that the photoelectric conversion efficiency (PCE) of PSC has rapidly increased from 3.8 percent to 23.3 percent [38], device stability remains a challenge that has limited their applications. In general, each component of the technology has an impact on its performance by completing its assigned responsibilities. As a result, optimizing the device components is critical [39]. Therefore, OPVs provide an alternate solution to the problems that traditional cells confront, owing to their structural flexibility, ease of device fabrication, and quick energy recovery [40].

Based on the types of electron donor and electron acceptor, OSCs may be classified into two types namely, fullerene and non-fullerene. Furthermore, based on the types of electron donor and electron acceptor non-fullerene OPVs are classified into four types, including polymer donor/polymer acceptor blend (PD/PA), polymer donor/small molecule donor blend (PD/SA), small molecule donor/polymer acceptor blend (SD/PA), and small molecule donor/polymer acceptor blend (SD/SA) [41]. Non-fullerene acceptors such as ITIC, IDIC, O-IDTBR, IT-4F, Y6 etc have been employed in the device fabrication of OPVs. Donor materials matching these non-fullerene acceptors have also received considerable interest. Owing to the complementary light absorption, high hole-mobility and deep highest occupied molecular orbital (HOMO) levels, wide-bandgap (WBG) and conjugated polymers are ideal donor partners for the low-bandgap non-fullerene acceptors.

D18 and its derivatives are a class of non-fullerene conjugated polymers used in different research field such as energy storage [42], organic light-emitting diodes [43], organic transistors [44] and organic photovoltaic cells [45]. To date, there are several methods that have been used to synthesize D18 and its derivatives namely: Stille coupling [46], Suzuki coupling [47], oxidation polymerization [48], electrochemical method [49] and Grignard reaction [50]. Stille coupling is the most preferred synthetic method for D18 by researchers because of its mild reaction conditions. $Pd(PPh_3)_4$ is used as a main catalyst during major steps of the synthesis. The most attractive application of the Stille coupling reaction is in the synthesis of conjugated, polyaromatic semiconducting materials, which are an important class of materials for organic electronics.

These materials exhibit good solubility in various solvents, which allows them to be fabricated into devices using inexpensive solution-phase printing techniques [51]. Over the past several decades, the development of semiconducting polymers has led to the advent of new technologies for numerous applications, ranging from organic light-emitting diodes (OLEDs), field effect transistor (FET), and organic photovoltaic (OPV) solar cells. Among these semiconducting polymers, the majority of them, especially those containing thiophene moieties, can be synthesized via Stille polycondensation [52] from related monomers. These polymers bear a wide variety of functional groups, and their emergence is enabled by the power and broad scope of the Stille polycondensation.

Liu et al. reported two D-A copolymers, L1 and L2 that are based on 5H-dithieno [3,2-b:20 ,30 -d] pyran-5-one unit. Both copolymers displayed wide bandgaps and deep HOMO levels which are desirable characteristics for improved performance of an OPV device. The deep HOMO levels generally favour to produce high Voc in solar cells. The HOMO levels for L1 and L2 are -5.45 and -5.52 eV, respectively, and the LUMO levels are -2.79 and -2.91 eV, respectively they fabricated an inverted solar cell device with L1 and L2 as the donors and Y6 as the acceptor, their device gave decent PCEs up to 14.36% [53]. Xiong and co. developed a new copolymer D16 by using a thiolactone unit, 5H-dithieno [3,2-b:20 ,30 -d] thiopyran-5-one (DTTP).

From L1 to D16, the simple replacement of lactone with thiolactone enhanced p-p stacking, gifting D16 higher hole mobility. The hole mobilities (lh) for L1 and D16 were measured by using space charge limited current (SCLC) method. As expected, D16 film showed a hole mobility of $1.19x10^{-3}$ $cm^2\ V^{-1}\ s^{-1}$, which is higher than that of L1 ($7.20x10^{-4}$ $cm^2V^{-1}s^{-1}$) and their best cell device gave a PCE of 16.72%, with a Voc of 0.85 V, a Jsc of 26.61 mA cm^{-2} and a FF of 73.8% [54]. Compared with the lactone analogue L1, D16 presented enhanced p-p stacking and higher hole mobility. The solar cells

based on the D16:Y6 blend afforded >16% PCE. This work demonstrates the great potential of fused-ring aromatic lactone building block copolymer donors in organic solar cells. On the other hand, Liu at el. synthesized a new quinoxaline-containing non-fullerene, AQx^{-3}, with longer branched alkyl chains (2-butylhexyl) and introduced it into the PM6:Y6 host system as the guest component. AQx^{-3} exhibited slightly blue shifted light absorption, and higher HOMO and LUMO energy levels relative to Y6.

The LUMO energy level of AQx^{-3} is −3.86 eV, which is slightly higher than that of Y6 (−3.90 eV). The HOMO energy level of AQx^{-3} (−5.64 eV) lies between the HOMO of PM6 (−5.58 eV) and Y6 (−5.70 eV), forming a cascade energy structure, which is beneficial for producing a higher Voc, as well as facilitating charge transport. Moreover, the film of the Y6:AQx^{-3} (2:1) blend exhibits just one oxidation and one reduction peak with medium LUMO and HOMO energy levels of −3.88 and −5.69 eV, respectively, located between those of Y6 and AQx^{-3}, which further demonstrates the formation of an alloy-like composite. Here we report our findings on the synthesis of novel D18-RM derivative synthesized using Stille polycondensation method. The chemical, optical, thermal, morphological, electrochemical and photovoltaic properties were investigated [55].

2.4. The operation principle of OPVs

Rafique et al. [56] proposed a simpler operating principle for the BHJ OSC device, consisting of four basic steps: (i) photon absorption and exciton generation, (ii) exciton dissociation, (iii) charge transfer, and (iv) charge collection. Light was absorbed by the donor material, which is a conjugated polymer, in their BHJ OPV device. An electron is accelerated from the highest occupied molecular orbital (HOMO) to the lowest unoccupied molecular orbital (LUMO) when photons are absorbed (LUMO) [57]. The excitons diffused to the donor-acceptor interface, where there was enough potential energy drop to divide them into free charge carriers, such as electrons and holes [58]. After splitting into free charge carriers, each carrier was delivered to the appropriate electrode through a bicontinuous interpenetrating channel that prevented recombination and charge trapping.

Some limitations and losses could occur during these steps such as absorption loss [59] due to spectral mismatch, thermalization loss [60], the insufficient energy required for exciton splitting, and charge recombination, etc. Below is a full description of each of the step involved in the process, from light absorption to charge carrier collection.

2.4.1 Light absorption and exciton generation.

Increased efficiency is a near-linear driver for lowering the cost of PV power per kilowatt-hour since efficiency is a fundamental parameter in the development of (PV systems. Shockley and Queisser (S-Q) proposed a theoretical framework for calculating the limiting efficiency of a single junction solar cell in 1961, based on the notion of detailed balancing, which equates the incoming and outgoing photon fluxes for a device under open-circuit circumstances [61]. This Shockley–Queisser limit defines the maximum practicable solar energy conversion efficiency for applied active materials. The photoactive layer must absorb the maximum amount of incoming sunlight as this is the standard by which new photovoltaic technologies are compared (**see Figure 2.3(a)**). The limit is that the maximum solar conversion efficiency is around 33.7% for a single p-n junction photovoltaic cell, assuming typical sunlight conditions (unconcentrated, AM 1.5 solar spectrum), at a band gap of 1.34 eV. The multi-junction concept is the most relevant approach to overcome the Shockley–Queisser limit for single-junction photovoltaic cells.

Questions have been raised about whether or not nanostructured organic photovoltaic devices can exceed the Shockley-Queisser limit. As previously stated, for high efficiency, light is absorbed by both donor and acceptor component of the BHJ photoactive layer [56], and light with high sufficient energy levels is absorbed by the OPV. Unlike in the inorganic material where the exciton binding energy (E_b) is small enough to reduce the attraction between the electron and hole pairs, organic excitons have a large binding energy (typically 0.2–1.0 eV) that drives the electron and hole to recombine after photoexcitation. A solution to this problem was proposed by Tang et al. in 1986 [43] which has been working ever since. It involves combining two organic semiconductors with slightly offset HOMO and LUMO energies, such that the photoexcited electron in the first material (normally the donor) is transferred to the second material (acceptor), allowing for the charges to be separated at the junction between these two materials.

The maximum possible efficiency is achieved when non-radiative recombination is absent and all generated carriers are either collected as current in the leads or recombine, emitting a single photon per electron-hole pair. Conjugated polymers, in particular, with extremely thin photoactive layers (up to 100 nm), may absorb light at the maximum of their absorption spectrum with a high absorption coefficient, unlike their inorganic silicon-based equivalents, which need hundreds of micrometres. It is important to produce donor polymers that absorb light in the longer wavelength area for next-

generation organic photovoltaics, that is, the absorption border should fall at wavelengths larger than 700 nm. The band gap of such polymers should be smaller than 2 eV [62].

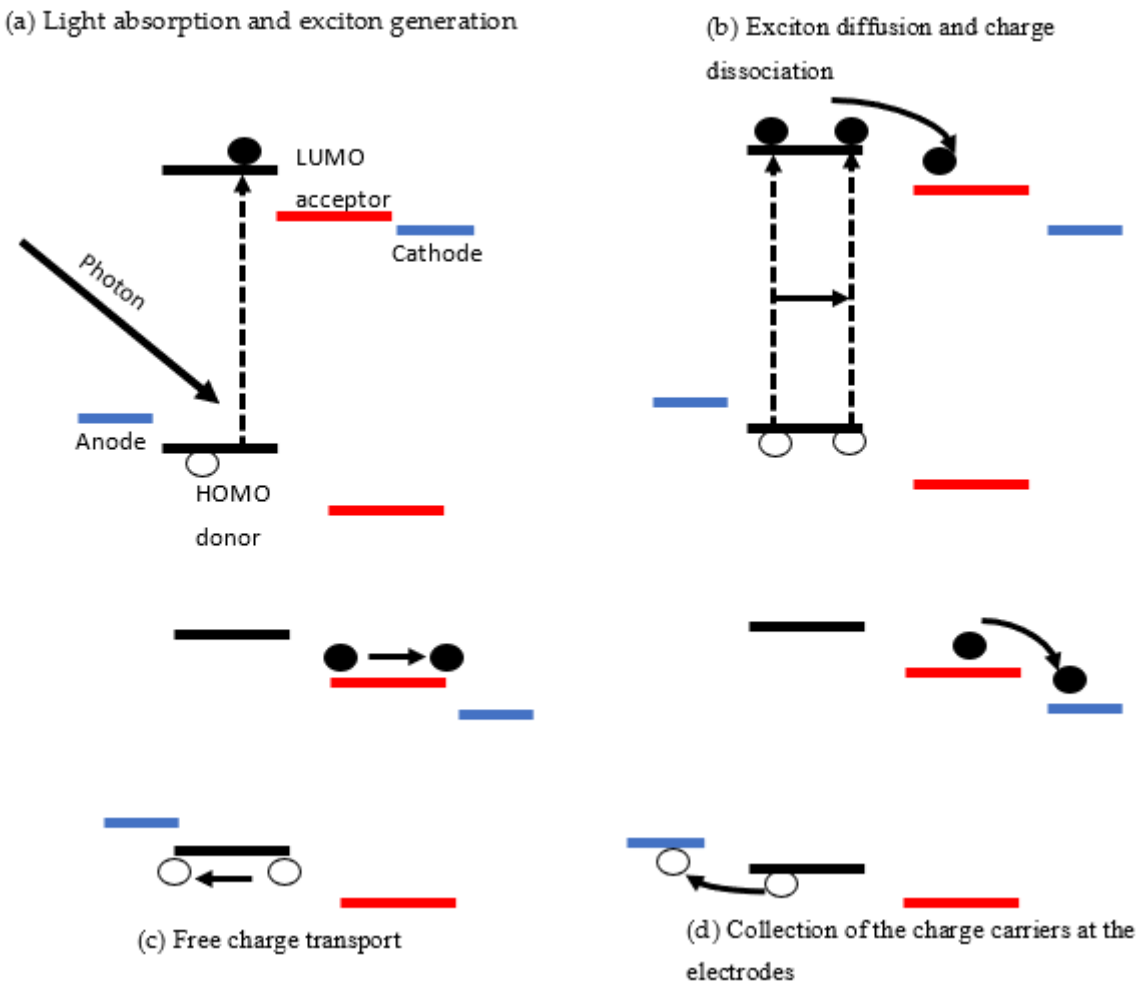

Figure 2.3 Illustration of the working principles of an OPV displaying the processes of (a) light absorption and exciton generation, (b) exciton diffusion and charge dissociation, (c) free charge transportation and lastly, (d) collection of charge carriers at the electrodes

2.4.2 Exciton diffusion and charge dissociation.

The second step involves the energy offset in LUMO between donor and acceptor materials which breaks the Coulomb attraction that ultimately causes the excitons to dissociate [63]. As most of the conjugated polymers exhibit a shorter lifetime of the excitons, the diffusion lengths are limited to a few nanometres, less than 20 nm, which is much shorter than the optical absorption pass length that is approximately 100–200 nm. It is, therefore, a prerequisite that excitons must be generated within their diffusion length (DL) for efficient charge generation [64]. Exciton diffusion length is defined as the distance travelled by an exciton before recombination (**see Figure 2.3(b)**) [65]. The reported excitons diffusion length for various conjugated polymers (of free carriers) significantly varies from 5 to 20 nm [56].

Thus, the thickness of the photoactive layer is very much critical for an efficient charge generation.Hoang and colleagues have recently demonstrated that single-material OPVs are being revived, not only because of their conceptual simplicity and considerably increased stability, but also because they may be used to learn about exciton dissociation and charge separation mechanisms. The production of intermediate inter-molecular charge-transfer (CT) excitons at the homojunction of a single p- and n-type doped organic semiconductor or at the interface of undoped domains with differing molecular orientation and packing has been shown to aid exciton dissociation in such devices [66].

2.4.3 Free charge carriers transport.

After the exciton dissociation into free charge carriers' step, the charges are transported towards the respective electrodes as shown in **Figure 3(c)** above. The transportation of charge carriers in organic semiconductors mostly takes place by hopping from one localized state to the next [67]. Separated holes and electrons are dispersed inside the donor and acceptor phases, respectively, after charge transfer occurs at the D/A contact. The transport of holes and electrons to their respective electrodes is then aided by an internal electric field derived from the Fermi level difference between the electrodes, with efficiency varying depending on their mobilities during the hopping process [68].

Concomitantly, nongeminate recombination (NGR) is typically in competition with collection of photogenerated charge carriers to each electrode not only at the short-circuit but also at the open-circuit conditions, and therefore impacts on both external quantum efficiency (EQE) and fill factor (FF). Therefore, optimised active layers should, in some cases, be kept as thin as possible (typically ∼100 nm) to avoid NGR loss. This, in return may decrease its effectiveness of solar light absorption. As

such, a key to efficient EQE and FF is suppressing NGR beyond limitations arising from the Langevin recombination.

2.4.4 Collection of the charge carriers at the electrodes.

Finally, charge carriers created by photons that do not recombine are removed from the photoactive layer and sent to the electrodes (see **Figure 2.3(d)**). There is a potential barrier at the photoactive layer/electrodes interface that is reduced to maximize the extraction of charges [57]. The barrier inhibits charge transport, resulting in significant charge accumulation at the interfaces. Charge accumulation increases the likelihood of recombination and reduces device performance. As a result, it is critical to boost charge separation and transfer efficiency. An interface buffer layer, which includes the anode and cathode buffer layers, is added in OPVs to overcome this problem. These buffer layers are frequently used to provide an ohmic contact between the active layer and the electrode, allowing for effective charge extraction and separation [69].

Therefore, the WF of the anode should match with the HOMO of the donor material, while the WF of the cathode must match with the LUMO of the acceptor material [70]. If the WFs match well as described, then the contacts are said to be Ohmic contacts. Contrary to this, if there is a mismatch between the anode and cathode with that of donor HOMO or acceptor LUMO, respectively, then no Ohmic contacts would be established. Ultimately, the performance of the solar cells will reduce [71]. The charge collection at the respective electrodes concludes the steps from absorption of light to generation of photocurrent [72].

2.5. References

[1] N. S. Lewis and D. G. Nocera, "Powering the planet: Chemical challenges in solar energy utilization," *Proc. Natl. Acad. Sci. U. S. A.*, vol. 103, no. 43, pp. 15729–15735, Oct. 2006, doi: 10.1073/PNAS.0603395103.

[2] J. Liu, M. Yao, and L. Shen, "Third generation photovoltaic cells based on photonic crystals," *J. Mater. Chem. C*, vol. 7, no. 11, pp. 3121–3145, Mar. 2019, doi: 10.1039/C8TC05461D.

[3] T. Burger, C. Sempere, B. Roy-Layinde, and A. Lenert, "Present Efficiencies and Future Opportunities in Thermophotovoltaics," *Joule*, vol. 4, no. 8, pp. 1660–1680, Aug. 2020, doi: 10.1016/J.JOULE.2020.06.021.

[4] A. Karani *et al.*, "Perovskite/Colloidal Quantum Dot Tandem Solar Cells: Theoretical Modeling and Monolithic Structure," *ACS Energy Lett.*, vol. 3, no. 4, pp. 869–874, Apr. 2018, doi: 10.1021/ACSENERGYLETT.8B00207/ASSET/IMAGES/LARGE/NZ-2018-00207F_0005.JPEG.

[5] N. Arora *et al.*, "Low-Cost and Highly Efficient Carbon-Based Perovskite Solar Cells Exhibiting Excellent Long-Term Operational and UV Stability," *Small*, vol. 15, no. 49, p. 1904746, Dec. 2019, doi: 10.1002/SMLL.201904746.

[6] F. M. van der Staaij, I. M. van Keulen, and E. von Hauff, "Organic Photovoltaics: Where Are We Headed?," *Sol. RRL*, vol. 5, no. 8, p. 2100167, Aug. 2021, doi: 10.1002/SOLR.202100167.

[7] J. Jean, M. Woodhouse, and V. Bulović, "Accelerating Photovoltaic Market Entry with Module Replacement," *Joule*, vol. 3, no. 11, pp. 2824–2841, Nov. 2019, doi: 10.1016/J.JOULE.2019.08.012.

[8] G. Kavlak, J. McNerney, and J. E. Trancik, "Evaluating the causes of cost reduction in photovoltaic modules," *Energy Policy*, vol. 123, pp. 700–710, Dec. 2018, doi: 10.1016/J.ENPOL.2018.08.015.

[9] A. Jäger-Waldau, "Snapshot of photovoltaics—February 2019," *Energies*, vol. 12, no. 5, 2019, doi: 10.3390/en12050769.

[10] M. Neukom, S. Züfle, S. Jenatsch, and B. Ruhstaller, "Opto-electronic characterization of third-generation solar cells," *http://www.tandfonline.com/action/journalInformation?show=aimsScope&journalCode=tsta20#.VmBmuzZFCUk*, vol. 19, no. 1, pp. 291–316, Dec. 2018, doi:

10.1080/14686996.2018.1442091.

[11] M. W. Wanlass *et al.*, “GaInP/GaAs/GaInAs Monolithic Tandem Cells for High-Performance Solar Concentrators,” 2005.

[12] J. F. Geisz *et al.*, “Six-junction III–V solar cells with 47.1% conversion efficiency under 143 Suns concentration,” *Nat. Energy 2020 54*, vol. 5, no. 4, pp. 326–335, Apr. 2020, doi: 10.1038/s41560-020-0598-5.

[13] N. Oulmi, A. Bouloufa, A. Benhaya, and R. Mayouche, “CuIn0.7Ga0.3Se2 thin films’ properties grown by close-spaced vapor transport technique for second-generation solar cells,” *Mater. Renew. Sustain. Energy*, vol. 8, no. 3, pp. 1–8, 2019, doi: 10.1007/s40243-019-0151-2.

[14] M. A. Green, Y. Hishikawa, E. D. Dunlop, D. H. Levi, J. Hohl-Ebinger, and A. W. Y. Ho-Baillie, “Solar cell efficiency tables (version 52),” *Prog. Photovoltaics Res. Appl.*, vol. 26, no. 7, pp. 427–436, Jul. 2018, doi: 10.1002/PIP.3040.

[15] Q. Liu *et al.*, “18% Efficiency organic solar cells,” *Sci. Bull.*, vol. 65, no. 4, pp. 272–275, Feb. 2020, doi: 10.1016/j.scib.2020.01.001.

[16] B. O’Regan and M. Grätzel, “A low-cost, high-efficiency solar cell based on dye-sensitized colloidal TiO2 films,” *Nat. 1991 3536346*, vol. 353, no. 6346, pp. 737–740, Oct. 1991, doi: 10.1038/353737a0.

[17] K. Kakiage, Y. Aoyama, T. Yano, K. Oya, J. I. Fujisawa, and M. Hanaya, “Highly-efficient dye-sensitized solar cells with collaborative sensitization by silyl-anchor and carboxy-anchor dyes,” *Chem. Commun.*, vol. 51, no. 88, pp. 15894–15897, Oct. 2015, doi: 10.1039/C5CC06759F.

[18] W. S. Yang *et al.*, “Iodide management in formamidinium-lead-halide-based perovskite layers for efficient solar cells,” *Science*, vol. 356, no. 6345, pp. 1376–1379, Jun. 2017, doi: 10.1126/SCIENCE.AAN2301.

[19] A. Singh and A. Gagliardi, “Efficiency of all-perovskite two-terminal tandem solar cells: A drift-diffusion study,” *Sol. Energy*, vol. 187, pp. 39–46, Jul. 2019, doi: 10.1016/J.SOLENER.2019.05.006.

[20] T. Duong *et al.*, “Rubidium Multication Perovskite with Optimized Bandgap for Perovskite-Silicon Tandem with over 26% Efficiency,” *Adv. Energy Mater.*, vol. 7, no. 14, p. 1700228, Jul. 2017, doi: 10.1002/AENM.201700228.

[21] N. G. Leonard, S. W. Lee, D. W. Chang, J. M. Hodgkiss, and D. Vak, “Organic Photovoltaic

New Renaissance: Advances Toward Roll-to-Roll Manufacturing of Non-Fullerene Acceptor Organic Photovoltaics," *Adv. Mater. Technol.*, vol. 2101556, 2022, doi: 10.1002/admt.202101556.

[22] A. Fakharuddin, F. De Rossi, T. M. Watson, L. Schmidt-Mende, and R. Jose, "Research Update: Behind the high efficiency of hybrid perovskite solar cells," *APL Mater.*, vol. 4, no. 9, p. 091505, Sep. 2016, doi: 10.1063/1.4962143.

[23] T. Leijtens, G. E. Eperon, S. Pathak, A. Abate, M. M. Lee, and H. J. Snaith, "Overcoming ultraviolet light instability of sensitized TiO2 with meso-superstructured organometal tri-halide perovskite solar cells," *Nat. Commun.*, vol. 4, Dec. 2013, doi: 10.1038/NCOMMS3885.

[24] R. Ilmi, A. Haque, and M. S. Khan, "High efficiency small molecule-based donor materials for organic solar cells," *Org. Electron.*, vol. 58, no. January, pp. 53–62, 2018, doi: 10.1016/j.orgel.2018.03.048.

[25] M. T. Kibria, A. Ahammed, S. M. Sony, and F. Hossain, "A Review : Comparative studies on different generation solar cells technology," *Int. Conf. Environ. Asp. Bangladesh*, pp. 51–53, 2014.

[26] D. L. Chandler, "Researchers improve efficiency of next-generation solar cell material," *MIT News*, 2021.

[27] P. K. Nayak, S. Mahesh, H. J. Snaith, and D. Cahen, "Photovoltaic solar cell technologies: analysing the state of the art," *Nat. Rev. Mater.*, vol. 4, no. 4, pp. 269–285, 2019, doi: 10.1038/s41578-019-0097-0.

[28] W. Liu *et al.*, "Perfection of Perovskite Grain Boundary Passivation by Rhodium Incorporation for Efficient and Stable Solar Cells," *Nano-Micro Lett.*, vol. 12, no. 1, pp. 1–11, 2020, doi: 10.1007/s40820-020-00457-7.

[29] K. Sharma, V. Sharma, and S. S. Sharma, "Dye-Sensitized Solar Cells: Fundamentals and Current Status," *Nanoscale Res. Lett.*, vol. 13, 2018, doi: 10.1186/s11671-018-2760-6.

[30] F. De Angelis, "Modeling materials and processes in hybrid/organic photovoltaics: From dye-sensitized to perovskite solar cells," *Acc. Chem. Res.*, vol. 47, no. 11, pp. 3349–3360, 2014, doi: 10.1021/ar500089n.

[31] N. Yeh and P. Yeh, "Organic solar cells: Their developments and potentials," *Renew. Sustain. Energy Rev.*, vol. 21, pp. 421–431, 2013, doi: 10.1016/j.rser.2012.12.046.

[32] S. Bhattacharya and S. John, "Beyond 30% Conversion Efficiency in Silicon Solar Cells: A

Numerical Demonstration," *Sci. Rep.*, vol. 9, no. 1, pp. 1–15, 2019, doi: 10.1038/s41598-019-48981-w.

[33] Y. Rong *et al.*, "Challenges for commercializing perovskite solar cells," *Science (80-.).*, vol. 361, no. 6408, Sep. 2018, doi: 10.1126/SCIENCE.AAT8235/ASSET/FA0D3D3C-9EC5-44B8-A024-C9EC9D4B5244/ASSETS/GRAPHIC/361_AAT8235_FA.JPEG.

[34] M. D. Archer, R. Hill, and K. Firm, *Clean Electricity*, vol. 1. 2001. [Online]. Available: http://scholar.google.com/scholar?hl=en&btnG=Search&q=intitle:Clean+Electricity+from+Photovoltaics#0

[35] X. Gan, O. Wang, K. Liu, X. Du, L. Guo, and H. Liu, "2D homologous organic-inorganic hybrids as light-absorbers for planer and nanorod-based perovskite solar cells," *Sol. Energy Mater. Sol. Cells*, vol. 162, no. December 2016, pp. 93–102, 2017, doi: 10.1016/j.solmat.2016.12.047.

[36] J. Kalowekamo and E. Baker, "Estimating the manufacturing cost of purely organic solar cells," *Sol. Energy*, vol. 83, no. 8, pp. 1224–1231, 2009, doi: 10.1016/j.solener.2009.02.003.

[37] M. A. Saeed, S. H. Kim, S. Y. Lee, and J. W. Shim, "High indoor performance of flexible organic photovoltaics using polymer electrodes," *Thin Solid Films*, vol. 704, p. 138006, Jun. 2020, doi: 10.1016/J.TSF.2020.138006.

[38] F. Xie *et al.*, "Vertical recrystallization for highly efficient and stable formamidinium-based inverted-structure perovskite solar cells," *Energy Environ. Sci.*, vol. 10, no. 9, pp. 1942–1949, 2017, doi: 10.1039/c7ee01675a.

[39] B. Cao *et al.*, "How to optimize materials and devices via design of experiments and machine learning: Demonstration using organic photovoltaics," *ACS Nano*, vol. 12, no. 8, pp. 7434–7444, 2018, doi: 10.1021/acsnano.8b04726.

[40] W. Greenbank, L. Hirsch, and S. Chambon, "Electrode de-wetting as a failure mechanism in thermally-aged OPV devices," *Sol. Energy Mater. Sol. Cells*, vol. 178, no. August 2017, pp. 8–14, 2018, doi: 10.1016/j.solmat.2018.01.011.

[41] Z. Zhang, Z. Ding, X. Long, C. Dou, J. Liu, and L. Wang, "Organic solar cells based on a polymer acceptor and a small molecule donor with a high open-circuit voltage," *J. Mater. Chem. C*, vol. 5, no. 27, pp. 6812–6819, 2017, doi: 10.1039/c7tc01996c.

[42] N. S. M. Shariff, M. S. P. Sarah, and M. Rusop, "Optical properties of different graphene concentration in P3HT," *AIP Conf. Proc.*, vol. 1963, no. 1, p. 020019, May 2018, doi:

10.1063/1.5036865.

[43] W. Tang, L. Ke, L. Tan, T. Lin, T. Kietzke, and Z. K. Chen, “Conjugated copolymers based on fluorene-thieno[3,2-b]thiophene for light-emitting diodes and photovoltaic cells,” *Macromolecules*, vol. 40, no. 17, pp. 6164–6171, 2007, doi: 10.1021/ma070575h.

[44] S. Brixi, O. A. Melville, N. T. Boileau, and B. H. Lessard, “The influence of air and temperature on the performance of PBDB-T and P3HT in organic thin film transistors,” *J. Mater. Chem. C*, vol. 6, no. 44, pp. 11972–11979, Nov. 2018, doi: 10.1039/C8TC00734A.

[45] Z. Çaldıran, Erkem, A. Baltakesmez, and M. Biber, “Effects of the PENTACENE as doping material on the power conversion efficiency of P3HT:PCBM based ternary organic solar cells,” *Phys. B Condens. Matter*, vol. 607, p. 412859, Apr. 2021, doi: 10.1016/J.PHYSB.2021.412859.

[46] A. Akkuratov *et al.*, “New cyclopentadithiophene-based (X-DAD′AD) n conjugated polymers for organic solar cells,” *Sol. Energy Mater. Sol. Cells*, vol. 193, no. December 2018, pp. 66–72, 2019, doi: 10.1016/j.solmat.2018.12.035.

[47] S. K. Lee, Y. K. Jung, W. S. Shin, H. K. Shim, and S. J. Moon, “Synthesis and characterization of fluorene-based conjugated polymers containing thiophene derivatives in main chain,” *Mol. Cryst. Liq. Cryst.*, vol. 520, pp. 10/[286]-18/[294], 2010, doi: 10.1080/15421401003604286.

[48] Y. J. Cheng and T. Y. Luh, “Synthesizing optoelectronic heteroaromatic conjugated polymers by cross-coupling reactions,” *J. Organomet. Chem.*, vol. 689, no. 24 SPEC. ISS., pp. 4137–4148, 2004, doi: 10.1016/j.jorganchem.2004.08.011.

[49] M. Sulev, T. Observatory, and B. Frederic, “Photosynthetically Active Radiation: Measurement and Modeling,” *SpringerReference*, no. September 2015, 2012, doi: 10.1007/springerreference_310766.

[50] K. Nakabayashi and H. Mori, “Donor-acceptor block copolymers: Synthesis and solar cell applications,” *Materials (Basel).*, vol. 7, no. 4, pp. 3274–3290, 2014, doi: 10.3390/ma7043274.

[51] X. Gu, L. Shaw, K. Gu, M. F. Toney, and Z. Bao, “The meniscus-guided deposition of semiconducting polymers,” *Nat. Commun. 2018 91*, vol. 9, no. 1, pp. 1–16, Feb. 2018, doi: 10.1038/s41467-018-02833-9.

[52] T. Vandermeeren *et al.*, “A PDTPQx:PC61BM blend with pronounced charge-transfer

absorption for organic resonant cavity photodetectors – direct arylation polymerization vs. Stille polycondensation," *Dye. Pigment.*, vol. 200, p. 110130, Apr. 2022, doi: 10.1016/J.DYEPIG.2022.110130.

[53] J. Liu *et al.*, "5H-dithieno[3,2-b:2′,3′-d]pyran-5-one unit yields efficient wide-bandgap polymer donors," *Sci. Bull.*, vol. 64, no. 22, pp. 1655–1657, 2019, doi: 10.1016/j.scib.2019.09.001.

[54] J. Xiong *et al.*, "Thiolactone copolymer donor gifts organic solar cells a 16.72% efficiency," *Sci. Bull.*, vol. 64, no. 21, pp. 1573–1576, 2019, doi: 10.1016/j.scib.2019.10.002.

[55] T. Zheng, A. M. Schneider, and L. Yu, "Stille Polycondensation: A Versatile Synthetic Approach to Functional Polymers," *Synth. Methods Conjug. Polym. Carbon Mater.*, pp. 1–58, 2017, doi: 10.1002/9783527695959.ch1.

[56] S. Rafique, S. M. Abdullah, K. Sulaiman, and M. Iwamoto, "Fundamentals of bulk heterojunction organic solar cells: An overview of stability/degradation issues and strategies for improvement," *Renew. Sustain. Energy Rev.*, vol. 84, no. November 2017, pp. 43–53, 2018, doi: 10.1016/j.rser.2017.12.008.

[57] C. Deibel and V. Dyakonov, "Polymer-fullerene bulk heterojunction solar cells," *Reports Prog. Phys.*, vol. 73, no. 9, 2010, doi: 10.1088/0034-4885/73/9/096401.

[58] A. C. Mayer, S. R. Scully, B. E. Hardin, M. W. Rowell, and M. D. McGehee, "Polymer-based solar cells," *Mater. Today*, vol. 10, no. 11, pp. 28–33, 2007, doi: 10.1016/S1369-7021(07)70276-6.

[59] M. K. Siddiki, J. Li, D. Galipeau, and Q. Qiao, "A review of polymer multijunction solar cells," *Energy Environ. Sci.*, vol. 3, no. 7, pp. 867–883, 2010, doi: 10.1039/b926255p.

[60] V. N. S. n Meena Dhankhar, Om Pal Singh, "Power Plant Emitin Smoke Steam Stock Photo (Edit Now) 1555865300," *Research Gate*. https://www.shutterstock.com/image-photo/power-plant-emitin-smoke-steam-1555865300 (accessed Jun. 29, 2021).

[61] M. C. Scharber and N. S. Sariciftci, "Efficiency of bulk-heterojunction organic solar cells," *Prog. Polym. Sci.*, vol. 38, no. 12, pp. 1929–1940, 2013, doi: 10.1016/j.progpolymsci.2013.05.001.

[62] J. Wang *et al.*, "Highly efficient all-inorganic perovskite solar cells with suppressed non-radiative recombination by a Lewis base," *Nat. Commun.*, vol. 11, no. 1, pp. 1–9, 2020, doi: 10.1038/s41467-019-13909-5.

[63] K. A. Mazzio and C. K. Luscombe, “The future of organic photovoltaics,” *Chem. Soc. Rev.*, vol. 44, no. 1, pp. 78–90, 2015, doi: 10.1039/c4cs00227j.

[64] M. GREEN *et al.*, “Solar cell efficiency tables (version 40),” *Ieee Trans Fuzzy Syst*, vol. 20, no. 6, pp. 1114–1129, 2012, doi: 10.1002/pip.

[65] Y. Zhou, M. Eck, and M. Krüger, “Bulk-heterojunction hybrid solar cells based on colloidal nanocrystals and conjugated polymers,” *Energy Environ. Sci.*, vol. 3, no. 12, pp. 1851–1864, 2010, doi: 10.1039/c0ee00143k.

[66] N. V. Hoang, V. C. Nikolis, L. Baisinger, K. Vandewal, and M. S. Pshenichnikov, “Diffusion-enhanced exciton dissociation in single-material organic solar cells,” *Phys. Chem. Chem. Phys.*, pp. 20848–20853, 2021, doi: 10.1039/d1cp03328j.

[67] H. Huang and W. Deng, “Introduction to organic solar cells,” *Org. Hybrid Sol. Cells*, vol. 9783319108, no. 3, pp. 1–18, 2014, doi: 10.1007/978-3-319-10855-1_1.

[68] P. W. M. Blom, V. D. Mihailetchi, L. J. A. Koster, and D. E. Markov, “Device physics of polymer:Fullerene bulk heterojunction solar cells,” *Adv. Mater.*, vol. 19, no. 12, pp. 1551–1566, 2007, doi: 10.1002/adma.200601093.

[69] W. Hou, Y. Xiao, G. Han, and J. Y. Lin, “The applications of polymers in solar cells: A review,” *Polymers (Basel).*, vol. 11, no. 1, pp. 1–46, 2019, doi: 10.3390/polym11010143.

[70] C. I. Primrose Magama, Sekina Lebotsa, “Renewable energy and physics.” p. Agrucultural Research Council-Institute for Agri, 2017.

[71] C. B. P. & L. B. Pieter F. Janse Van Vuuren, “Solar Energ in Agri-processing,” 2016.

[72] R. Mabindisa, K. Tambwe, L. McIteka, and N. Ross, “Organic nanostructured materials for sustainable application in next generation solar cells,” *Appl. Sci.*, vol. 11, no. 23, 2021, doi: 10.3390/app112311324.

Chapter 3 – Research design and methodology

This chapter is based on the description of the methods and investigative techniques used in the development of the experiments of this project. In the first part a full description of the materials and chemicals used in this research work is given, followed by the synthetic route used to prepare the donor material. Preparation of the active layer as a bulk heterojunction and photovoltaic parameters for the organic photovoltaic cell are also provided. Beside the comprehensive photovoltaic cell characterization techniques explained, complete interface characterization techniques are also provided in this chapter.

3.1 Materials

The reagents used to prepare the donor polymer comprising of DTBT-2Th48Br and BDTOEHSn were purchased from Ossila. Catalysts: Potassium carbonate (K_2CO_3), Copper Iodide (CuI) and $Pd(PPh_3)_4$ together with solvents: toluene, methanol, acetone and 1,2-dichlorobenzene were purchased from Sigma Aldrich. Toluene was degassed with nitrogen gas to remove oxygen and water [1]; other commercially available materials were used as received. Thin-layer chromatography [2] was used to monitor the reaction at an interval of 2 hour for the duration of the experiment.

3.2 Synthesis of D18-RM

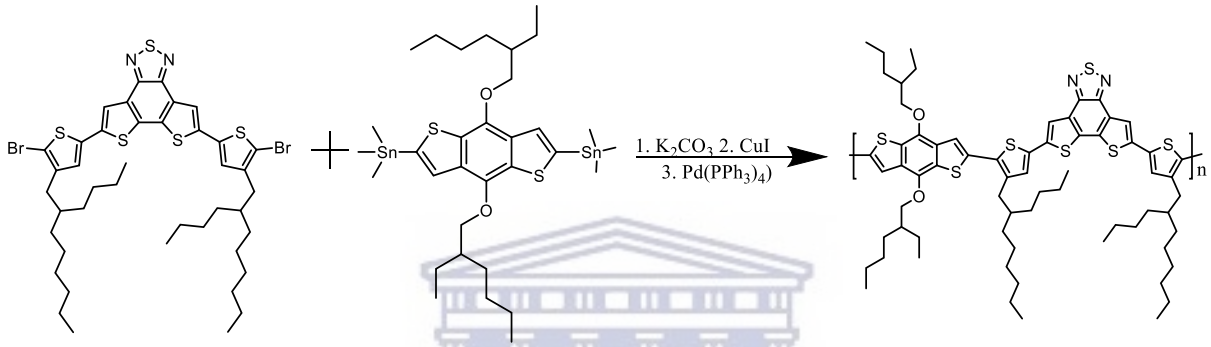

Scheme S 3-1 The synthetic route for D18-RM

Toluene (40 ml) solvent was initially degassed for 30 minutes before a mixture of DTBT-2Th48Br (100 mg, 0.11 mmol), BDTOEHSn (103.7 mg, 0.11 mmol) was introduced in a one-neck round bottom flask. The mixture of the two monomers (precursors) was subsequently followed by the addition of Potassium carbonate (K_2CO_3) (60.3 mg, 0.44 mmol), Copper Iodide (CuI) (83.8, 0.44 mmol) and $Pd(PPh_3)_4$ (50.4 mg, 0.22 mmol 20%) as catalysts for the reaction. The mixture was then constantly heated at 90 °C under reflux for 16 hours. After 16 hours has elapsed, the solution was allowed to cool down to room temperature before 150 mL of Methanol is added dropwise manner. The resulted precipitate was collected and further purified via filtration using 3 portions of 10 mL of Acetone $(CH_3)_2CO$ and Methanol (CH_3OH) each. Thereafter, precipitate was dried under vacuum overnight to give the final product D18-RM as a brown solid (123.3 mg, 96.3%) [3].

3.3 Mechanism of the synthetic method used in this study

Stille coupling reaction is a chemical reaction that involves the use of organotin compounds and halogenated compounds to form carbon−carbon bond in the presence of palladium-based catalyst [6]. A typical Stille coupling reaction is shown in **Scheme 3.2** below.

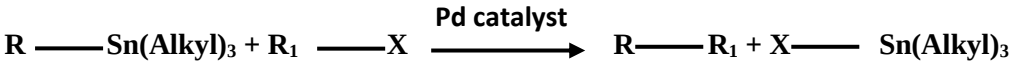

Scheme S 3-2 General Stille coupling reaction

R and R_1 can be either alkenyl, benzyl, allyl, aryl or acyl, while X represent the halogens (bromine, chlorine, and iodine). The cyclic reaction mechanism of this method is given in Scheme 3.3. In details, the first step is the oxidative addition of R−X to the palladium-based catalyst (Pd^0) resulting in an intermediate Pd^{II} with 16-electron transition state [7]. The second step is called trans-metalation. During this step, organotin compound is used as trans coupling reagent [8]. The organotin compound together with R_1 will form a four membered ring with the Pd^{II} intermediate and X forming transition state of 18-electron [9]. Then, organotin will leave with the X. This results in the intermediate of Pd^{II} bonded to R and R_1. Finally, R and R_1 will isomerize into cis-conformation before undergoing reductive elimination [10]. These steps are shown is scheme 3.3 below.

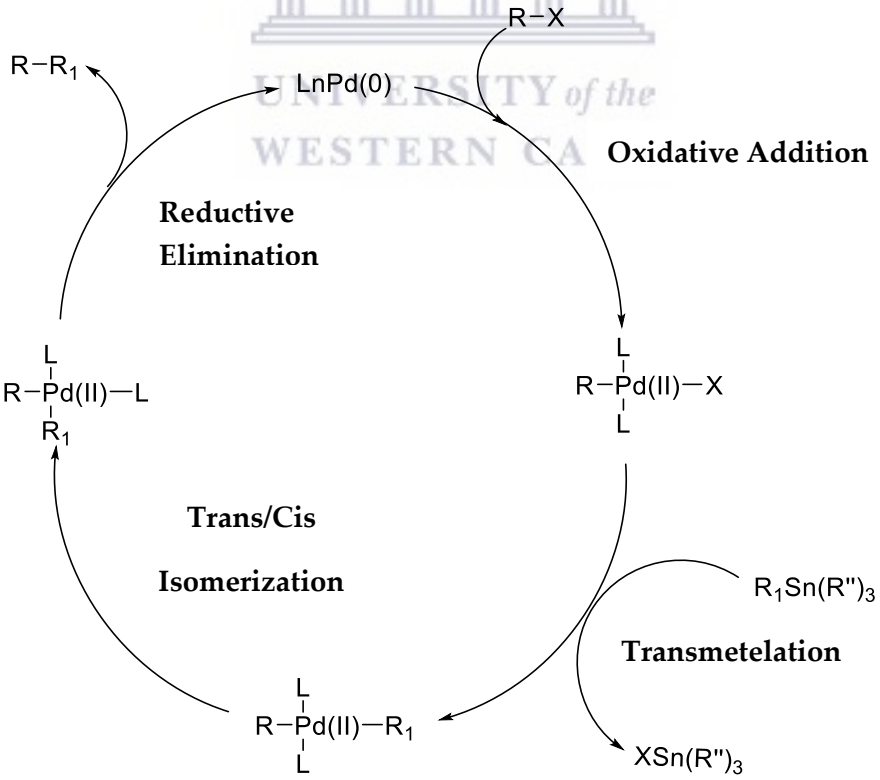

Scheme S 3-3 Stille Coupling Mechanism

3.4 Characterization and analytical measurements

Thin layer chromatography (TLC) was used to monitor the reaction progress. Silica gel coated plates (Merck (Pty) Ltd., Johannesburg, South Africa) were used for thin layer chromatography profiling. Three spots for DTBT-2Th48Br, BDTOEHSn and crude were plotted on the silica gel coated plate. The plate was then immersed into a development tank that contained a solution of dichloromethane and toluene (2:8). The spots on the silica gel coated plates were viewed using ultra-violet lamp (254 nm and 366 nm).

^{1}H and C-13 NMR spectra were obtained from Bruker AVANCE 500 spectrometer after 13 and 36 scans respectively. FTIR spectra were obtained on Perkin-Elmer Spectra One from 400-4000 cm^{-1} frequency using KBr as a blank. XRD was utilized to investigate the phase composition and crystallinity of the synthesized material. TGA data was obtained after heating the synthesized polymer from 30 ºC to 800 ºC. Rheometer was also employed in this study to analyze the flow behavior of the material at range of 10-100 s^{-1} shear rate. For this experiment a viscosity curve and flow curve were used in the analysis. UV–vis spectra and photoluminescence (PL) spectra were measured from 300-800 nm wavelength on PerkinElmer lambada 25 spectrometer and NanoLog with FluorEssenceTM V3 software from Horiba Jobin Yvon spectrometer, respectively using 1,2-dichlorobenzene as a solvent and a blank.

Non-tapping mode atomic force microscopy (AFM) was also utilized, at least 4 images from different areas of the sample coated on an ITO were taken for each sample individually and the average roughness was used. In the case of uneven films, the height was averaged over a range of positions in order to guarantee a more accurate reading. Cyclic voltammetry (CV) was conducted on an electrochemistry workstation (CHI660A, Chenhua Shanghai) with the polymer film with ITO substrate as the working electrode, Pt wire as the counter electrode, and Silver/Silver chloride as a reference electrode in a 0.1 M tetra-n-butylammonium hexafluorophosphate acetonitrile solution at a scan rate of 100 mV/s. The CV study was subsequently followed by Square-Wave voltammetry (SWV) at a potential window between -2 and 2 volts since sulfur (electron donating group) undergo redox reactions within that range. Scan rate study was also conducted for both CV and SWV. The oxidation and reduction maximum peaks were then used to run electrochemical impedance spectroscopy (EIS).

3.5 Substrates and Device Fabrication

The type of ITO substrates that were used to fabricate the devices are shown in **Figure 3.1.** Before deposition of the layers, the substrates were temporarily masked with Kapton tape on both ends to allow for only the central part to be uncovered as depicted in Figure 3.3 below:

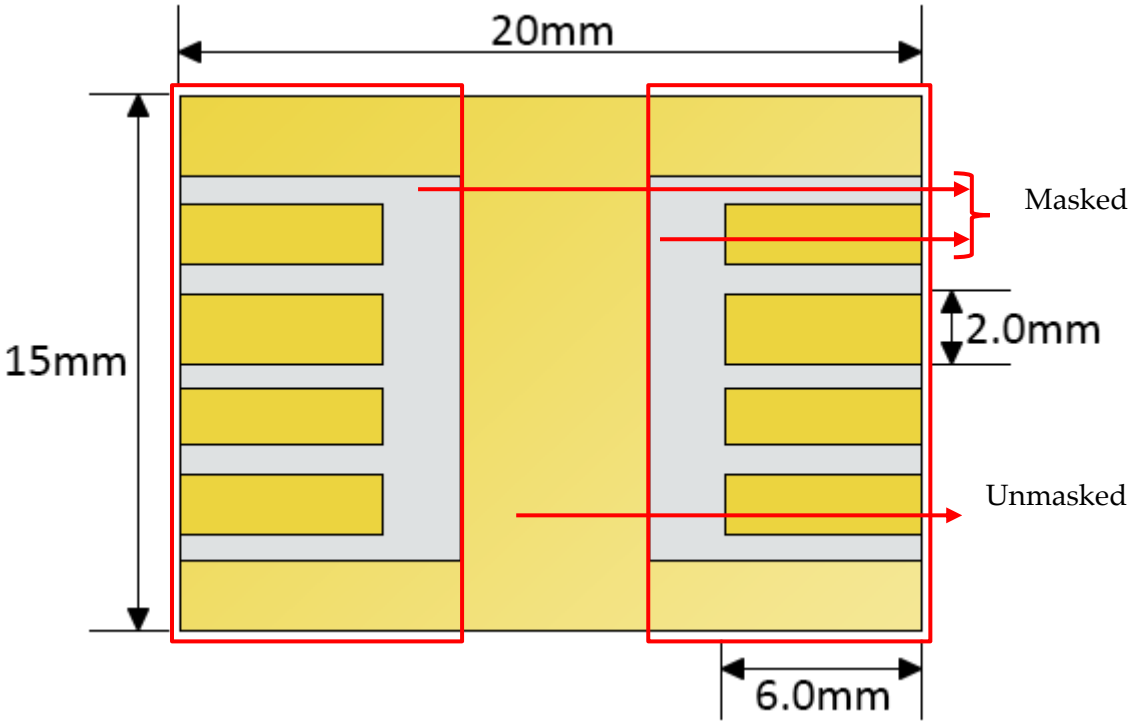

Figure 3.1: Schematic of the ITO substrates showing the areas that were masked before spin [4].

ITOs were purchased from Ossila with the specifications listed in the Table. 3.1. This particular type of patterned ITO substrates were used because it was better adapted to the type of metal deposition mask available in our labs (multi-electrode mask from Ossila).

Table 3.1 ITO substrate specification

Substrate size	20 mm x 15 mm
Thickness	1.1 mm
Glass type	Polished soda lime, float glass
Substrate coating	Fully oxidized ITO
ITO thickness	100 nm
ITO resistance	14 Ω / square
Glass roughness	< 1nm RMS (By AFM)
ITO roughness	1.8 nm RMS (By AFM)

3.5.1. ITO Cleaning

The method and solvents used to clean the substrates comprise of sonification with fractions of 1% hellmanex solution in hot deionized water, isopropanol (99%) and acetone (99%) at an interval of 10 minutes in between. Deionized water was prepared with Millipore filtration system. The cleaned ITOs were then dried using nitrogen gas.

3.5.2. Zinc Oxide (ZnO) seed layer

The ZnO seed layer was prepared by dissolving zinc acetate dihydrate (4.39 g, 0.02 mol) and monoethanol amine (1.22 g, 0.02 mol) in 2-methoxyethanol (40 ml). The solution was subsequently stirred and heated using oil bath under reflux at 60 °C for 1 hour [5].

3.5.3. Device Fabrication

The as-prepared ZnO was spun coated for 30 seconds at the rate of 4000 rpm using the amount of 40 μL. The thin film was wiped at the cathode using cotton bud and baked at 150 ℃ for 5 minutes. The donor and acceptor materials were blended (1:0.8), constantly stirred and heated at 60 ℃ for overnight. The solution was spin coated onto the ZnO coated ITO at the spin rate of 2000 rpm for 30 seconds. The film was annealed at 100 ℃ for 5 minutes. The final layer of silver paste was coated using micro-pipette tip. The photovoltaic parameters were determined from the current as a function of voltage obtained under light illumination of AM 1.5G, 100 $mW.cm^{-2}$ supplied by a solar simulator from Sciencetech Inc., London, ON, Canada, using a source meter (X200 Source Meter Unit from Ossila, Sheffield, UK).

3.6 References

[1] Z. Zhao, Z. Liu, Y. Xiang, M. Arowo, and L. Shao, "Removal of dissolved oxygen from water by nitrogen stripping coupled with vacuum degassing in a rotor–stator reactor," *Processes*, vol. 9, no. 8, 2021, doi: 10.3390/pr9081354.

[2] N. Wu *et al.*, "Adapting Meaningful Learning Strategies for an Introductory Laboratory Course: Using Thin-Layer Chromatography to Monitor Reaction Progress," *J. Chem. Educ.*, vol. 96, no. 9, pp. 1873–1880, 2019, doi: 10.1021/acs.jchemed.9b00256.

[3] Liu, Qishi, Yufan, Jiang, Ke, Jing, "18 % Efficiency organic solar cells," 2020.

[4] Ossila Group, "ITO Glass Substrates | PV and OLED, 20 x 15 mm | Ossila," *Ossila Ltd*, 2022. https://www.ossila.com/products/pv-substrates (accessed Oct. 03, 2022).

[5] M. E. Ramoroka, S. B. Mdluli, V. S. John-Denk, K. D. Modibane, C. J. Arendse, and E. I. Iwuoha, "Synthesis and photovoltaics of novel 2,3,4,5-tetrathienylthiophene-co-poly(3-hexylthiophene-2,5-diyl) donor polymer for organic solar cell," *Polymers*, vol. 23, no. 1. pp. 1–14, 2021. doi: 10.3390/polym13010002.

[6] T. Zheng, A. M. Schneider, and L. Yu, "Stille Polycondensation: A Versatile Synthetic Approach to Functional Polymers," *Synth. Methods Conjug. Polym. Carbon Mater.*, pp. 1–58, 2017, doi: 10.1002/9783527695959.ch1.

[7] M. L. Christ, S. Sabo-etienne, and B. Chaudret, "16-Electron Dihydrogen Complexes of Ruthenium," no. 14, pp. 3800–3804, 1994.

[8] Y. T. Chang, L. J. Liu, W. S. Peng, L. T. Lin, Y. T. Chan, and F. Y. Tsai, "Stille coupling for the synthesis of isoflavones by a reusable palladium catalyst in water," *J. Chinese Chem. Soc.*, vol. 68, no. 3, pp. 469–475, 2021, doi: 10.1002/jccs.202000478.

[9] X. Yang, "The 18-electron rule for main-group alkaline earth octacarbonyl complexes," *Natl. Sci. Rev.*, vol. 6, no. 1, pp. 8–9, 2019, doi: 10.1093/nsr/nwy129.

[10] M. M. Heravi, E. Hashemi, and F. Azimian, "Recent developments of the Stille reaction as a revolutionized method in total synthesis," *Tetrahedron*, vol. 70, no. 1, pp. 7–21, 2014, doi: 10.1016/j.tet.2013.07.108.

Chapter 4 – Results: Presentation and Discussion

This chapter presents the results generated from the different characterization techniques performed, their analysis and discussion. The following techniques were used, NMR for confirmation of the polymer chemical structure, FTIR for active bonding configurations to further confirm the chemical structure, TGA for thermal stability, HR-SEM and AFM for surface morphology, HR-TEM for particle size distribution, XRD for crystallinity, UV-Vis for absorbance, CV and EIS for electrochemical properties and I-V curve measurements for photovoltaic performance. The most important deductions and conclusions are based on measured photovoltaic parameters. The OPV device was fabricated in air with relative humidity of about 60% and because of the moisture in air and other atmospheric effects, the OPV fabrication is not totally reproducible, and the degree of degradation varies. Thus, the photovoltaic parameters of the prepared solar cell series are not fully comparable to each other.

4.1. Structural Confirmation Using NMR Analysis

The ^{1}H NMR spectrum shown in **Figure 4.1(a)** and **(b)** shows the region and integration of protons available from the monomer DTBT-2Th48Br and BDTOEHSn respectively. The two monomers were selected based on their desirable properties such as high degree of conjugation which allow easy electron movement, larger molecular plane structure, and a backbone made up of alternating electron donating and electron accepting fused rings. When these monomers react via Stille coupling reaction [1], theoretically they are producing a polymer with characteristics that resemble those of D18 which by far produce the highest efficiency in the field of OPVs. The number of protons obtained from the spectrum of the two monomers through integration of peak intensity is the same as the number of protons from the chemical structure of each monomer, these findings confirm good conditions of the starting nanomaterial at which the synthesis was carried out.

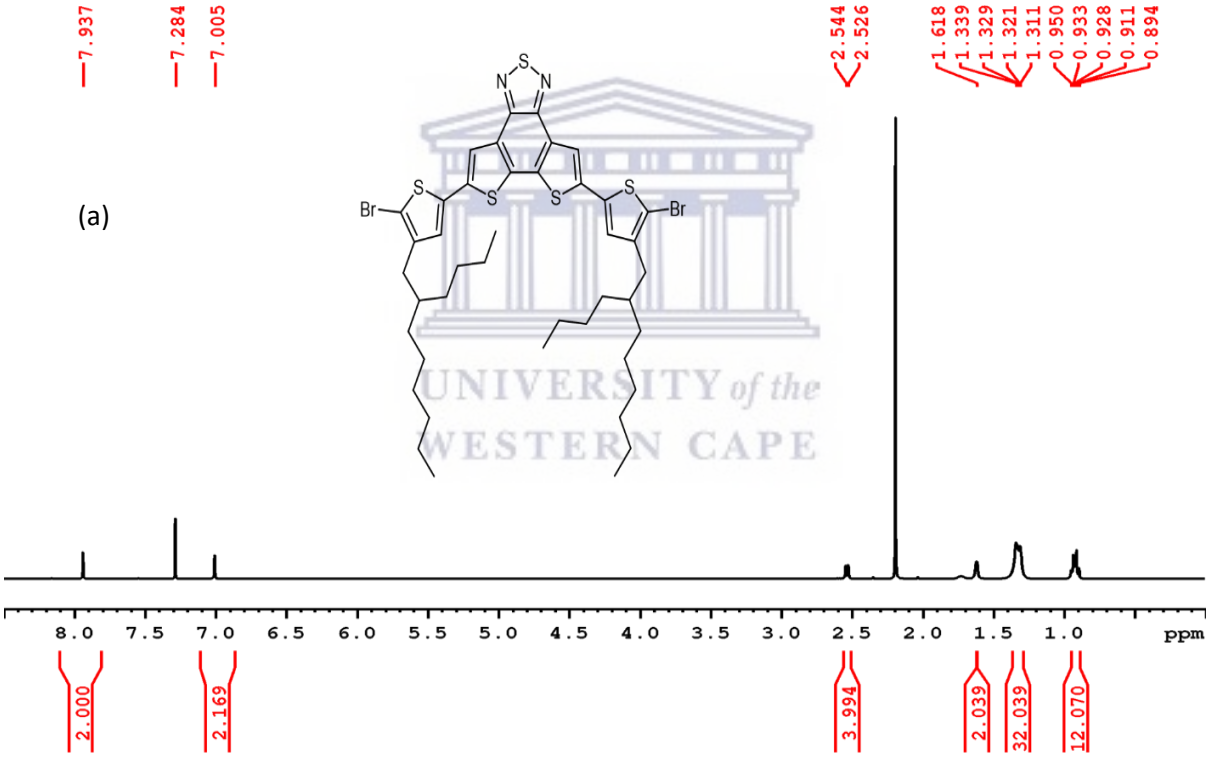

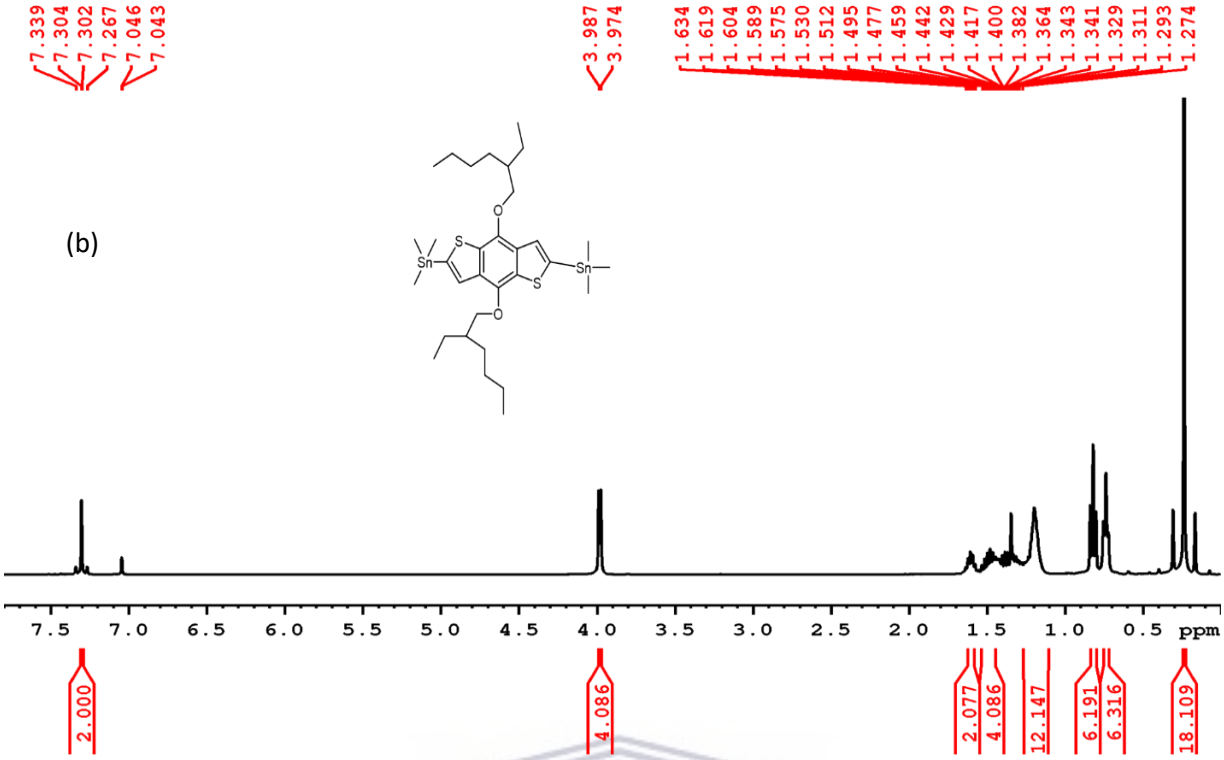

Figure 4.1 ^{1}H NMR spectrum of (a) DTBT-2Th48Br and (b) BDTOEHSn

In **Figure 4.1(a)** the multiplet signals between 0.89-1.62 ppm are due to CH, CH_2 and CH_3 aliphatic protons and they integrate to 2, 32 and 12 protons respectively. The doublet that integrates to 4 protons at 2,53 and 2,54 ppm are attributed to the CH_2 that is attached to the aromatic ring. Since the monomer DTBT-2Th48Br have a molecular plane of symmetry, the singlet aromatic protons that appear between 7,01-7,94 ppm overlap and thus, only 3 signals are observed, the results are confirmed from the derived number of protons from these signals. In **Figure 4.1(b)** the multiplet peaks between 1,27-1,63 ppm is due to CH, CH_2 and CH_3 aliphatic protons of monomer BDTOEHSn. The doublet that integrates to 4 protons at 3,97 and 3,99 ppm represent the 2 protons of the CH_2 that is attached to the O-atom. Since the monomer BDTOEHSn also have a molecular plane of symmetry, the singlet aromatic protons that appear at 7,30 ppm overlap and thus, only 1 distinct signal appears, but the integration confirm the number of protons that results this signal.

Figure 4.2 (a) and **(b)** shows carbon-13 spectra of monomers BDTOEHSn and DTBT-2Th48Br, respectively. The number of peak signals for each spectrum for the two monomers is in agreement with the number of peak signals that is theoretically expected and that confirms the cleanness and purity of the precursors. The signals between 11,4-40,6 and 14,2-38,2 ppm represents the CH, CH_2 and CH_3 aliphatic carbons for both BDTOEHSn and DTBT-2Th48Br respectively. The signals between 127,9-143,3 and 110,3-150,2 ppm are due to the aromatic carbons for BDTOEHSn and DTBT-2Th48Br, respectively.

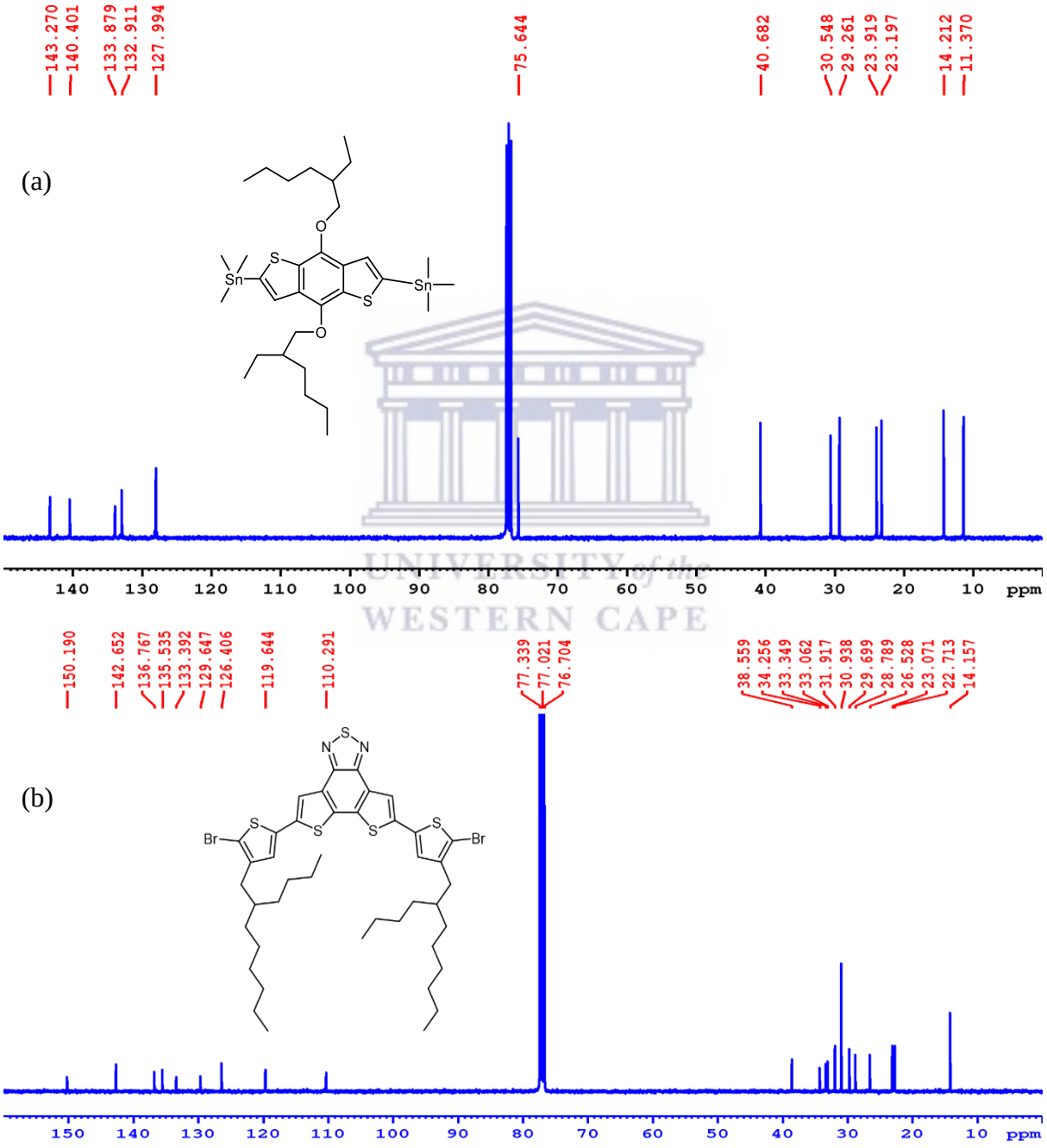

Figure 4.2 C-13 NMR spectrum of (a) BDTOEHSn and (b) DTBT-2Th48Br

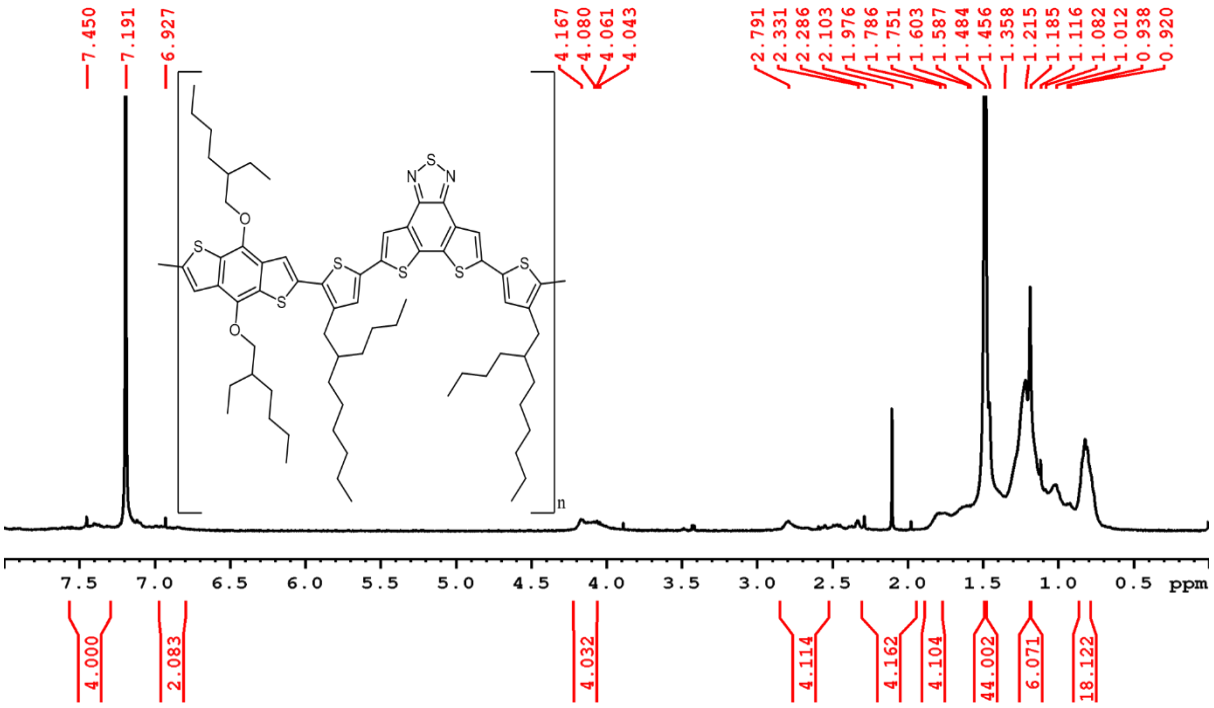

Figure 4.3 ^{1}H NMR spectrum of D18 derivative (D18-RM)

Figure 4.3 shows the ^{1}H NMR spectrum of the synthesized polymer D18 derivative (D18-RM). The polymer has a large molecular plane of symmetry as a result, majority of peaks due to the aliphatic protons (0.92-2.79 ppm) overlap and show intense peak signal. The number of protons obtained from the spectrum of the polymer through integration is the same as the number of protons from the chemical structure of the polymer, these findings confirm the theoretical results that were expected to ensure that the synthesis of this polymer was successful. The multiplet signals between 0,92-2,79 ppm are due to the CH, CH_2 and CH_3 aliphatic protons, and the distinct multiplet at 4,07 ppm is due to the protons of the CH_2 thatwas attached to the O-atom. The singlet aromatic protons that appear between 6.93-7,45 ppm overlap and thus, only 2 signals appear, but the integration confirm the number of protons that results these signals. This once again confirms the success of polymerization synthesis of D18-RM since the signals due to both monomers are also present in the polymer.

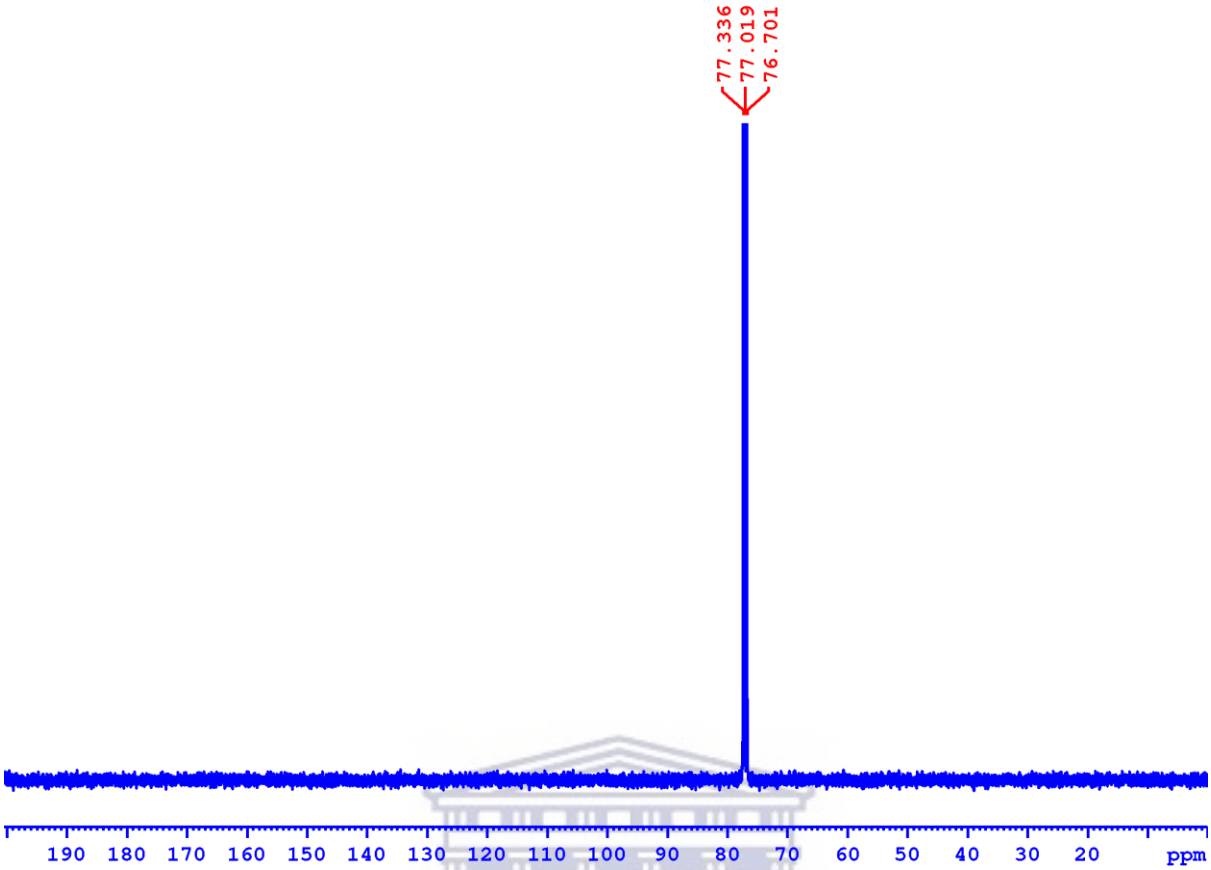

Figure 4.4 C-13 NMR of D18-RM after 2048 scans.

As shown in **Figure 4.4** C-13 NMR of the synthesized polymer show no peaks. This is because of lack of nuclear Overhauser effect and slow relaxation of D18-RM carbons [2]. The interaction involved is the direct magnetic coupling (the dipolar coupling) between nuclei, which does not usually have any observable effect on spectra recorded in solution, hence there are no peaks visible in the spectrum [3]. Nevertheless, these findings about the non-fullerene polymers are consistent throughout the literature, thus we are confident that we have successfully synthesized the desired non-fullerene polymer that acts as a donor in the fabrication of the OPV device.

4.2. Analysis of IR active bonding configurations by FTIR

FTIR was used to determine the functional groups and bonds present in the synthesized D18-RM polymer. The spectrum of the polymer was then compared with that of the monomers as shown in the overlaid FTIR spectra in **Figure 4.5**. The reason for the comparison was to confirm the unique bond stretches. Physically it is expected that the as-synthesized polymer spectrum is intertwined from the spectra of the two monomers, however, since the synthetic process was chemical instead, there are unusual observations from the spectrum of the polymer which suggest that there is a long-range intermolecular interaction that is taking place within the polymer.

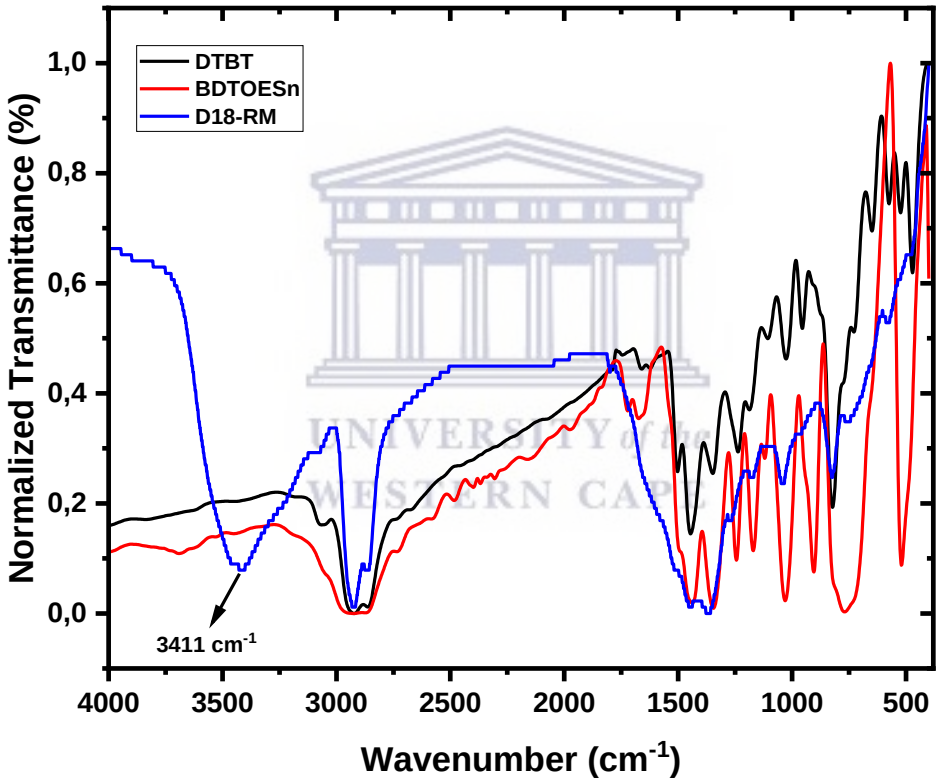

Figure 4.5 Overlaid FTIR spectra of D18-RM polymer with its building monomers.

There is a distinct strong and broad peak at 3411 cm^{-1} that is due to O-H functional group. This is an unusual peak for this polymer, according to the literature [4], these polymers have the ability to form intermolecular bonded O-H bonding, and thus the peak at 3411 cm^{-1} is a result of intermolecular bonded O-H group. Characteristic peak at 1300 cm^{-1} stretching vibrations was observed and ascribed to the C-O bond attached to the aromatic ring. The aliphatic CH, CH_2 and CH_3 vibrations are observed between 1000-500 cm^{-1} and they are identical for both

monomers, however, an aliphatic C-C shift towards lower frequencies was observed for the polymer and it was assigned to the isotope effect [5] that comes with the intramolecular vibration of the two polymerized monomers.

These findings compliment the NMR results discussed in section 4.1. Thus far, there is no scientific evidence that this aspect of intramolecular vibration is detrimental in the performance of an OPV device. Therefore, the as synthesized non-fullerene polymer displays a great potential to produce high efficiency.

4.3. XRD Analysis for Crystallinity and Atomic Arrangement

The phase composition and crystalline structure of the synthesized nanomaterial were analysed through powder X-ray diffraction (XRD). The donor polymer was crystallized in the monoclinic crystal system. XRD studies of D18-RM were done to investigate the phase composition and crystallinity. The crystallinity can be calculated using the following **Equation 4.1**

$$Crystallinity = \frac{Area\ of\ crystalline\ peaks}{Area\ of\ all\ peaks\ (crystalline+amorphous)} \times 100 \quad [4.1]$$

Figure 4.6 below shows that there were no amorphous peaks observed and that makes the donor polymer 99,9% crystalline or polycrystalline. The crystallinity of OPV nanomaterial is an important characteristic because it has a significant impact in the morphology of the active layer, concurrently the morphology of the active layer affects the stability of the OPV device and thus the performance also gets affected. According to the findings from Yi et al. [6] a stable BHJ blend active layer with a highly crystalline polymer can enhance the operation stability and thus high efficiency of an OPV device. This is promising feature for the synthesized D18-RM donor polymer towards operation stability since it also displays high degree of crystallinity.

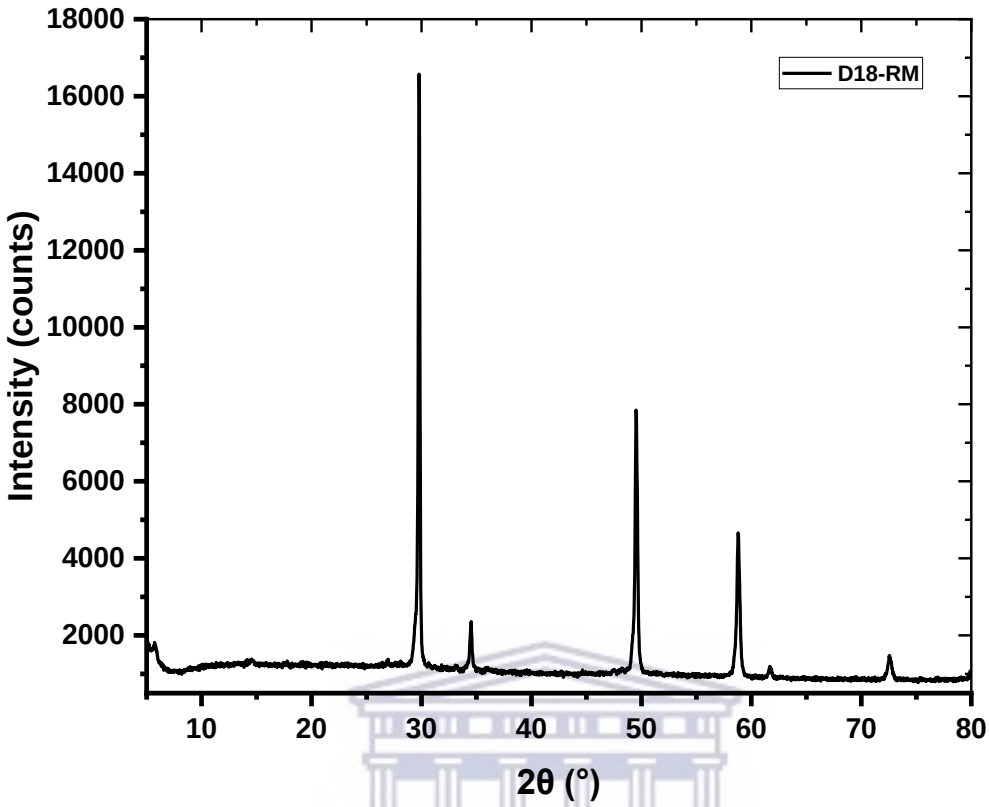

Figure 4.6 X-ray diffraction pattern for polymer D18-RM

4.4. Thermal stability analysis by TGA

Figure 4.6 shows the thermograms of D18-RM synthesized polymer. This technique was employed to investigate thermal stability of the synthesized D18-RM polymer under high temperatures in an inert gas ambient. It is well known that the effect of high pressure and temperature on a solid can promote the breaking and modification of chemical bonds, namely their bond length and bond angles [6]. Thermogravimetric analysis (TGA) results can be integrated with those obtained from FTIR to precisely establish the thermal nature and number of the functional groups or bonds that are susceptible to thermal degradation. This would help in picking up or choosing the right nanomaterial to functionalize with in order to improve the thermal stability. The thermodynamic activation parameters of the decomposition process of the polymer such as activation energy (Ea) and order of reaction (n) were evaluated graphically by employing the Freeman–Carroll method [7] using the following relation in ***Equation 4.2:***

$$\frac{\left[\left(-\frac{E_a}{2.303R}\right)\Delta\left(\frac{1}{T}\right)\right]}{\Delta log w_r} = -n + \frac{\Delta log\left(\frac{dw}{dt}\right)}{\Delta log wr} \qquad [4.2]$$

where T is the temperature in K, R is gas constant, wr=wc–w; wc is the mass loss at the completion of the reaction and w is the total mass loss up to time t. Ea and n are the energy of activation and order of reaction, respectively.

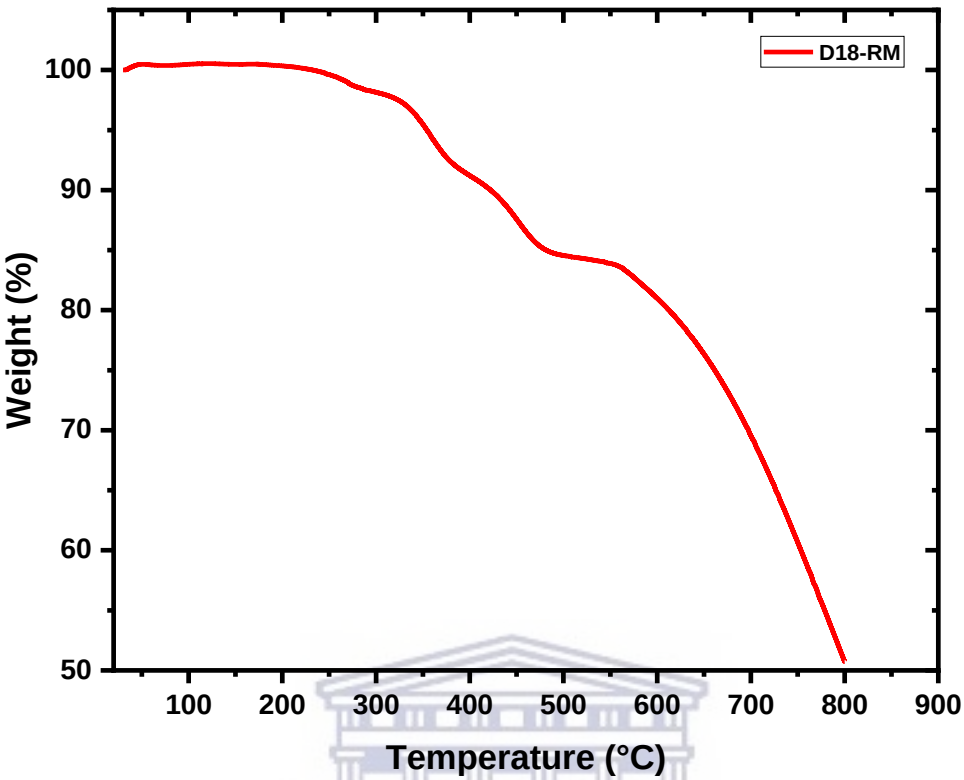

Figure 4.7 TGA thermograms of D18-RM observed from temperature range of 30 ºC to 800 ºC.

As shown in **Figure 4.7**, between 25 and 200 °C there was an unusual 0.54% weight increase for the sample since the system is hygroscopic and that was assigned to the formation of non-volatile oxides, possibly palladium dioxide. Usually these polymers are purified via Soxhlet extraction [8] which maintain the solubility of the polymer after synthesis is completed, thus the polymer was not 100% pure after purification (partial purification) and still had some of the content of the catalysts. However, between 250-300 °C there was a 2.33% weight loss that was due to the solvent vaporization [9], and the loss of one mole of solvent 1,2-dichlorobenzene molecule is of first order reaction and the value of enthalpy for the process is found to be 2.93 kJ mol^{-1} and that was followed by a noticeable 12.97% weight loss between 340-410 °C, which was ascribed to the decomposition of the long aliphatic chains, hexyl- and octyl-group, their enthalpy values were found to be -5.7 and -7.2 kcal/mol, respectively.

The shorter aliphatic chains ethyl- and butyl-group started to decompose between 402-472 °C and 33.18% weight loss was observed [10], their enthalpy values were reported to be 3.1 and 4.4 kcal/mol [11]. According to the literature by S. Chatterjee, Ie, and Aso [12] the fused thiadiazole and thiophene residues decompose at higher temperature above 700 and 800 °C

respectively, thus it is not easy to quantify their total weight loss within the temperature range in which the sample was analysed from. To further analyse where the decomposition temperatures occur, we looked at the derivative curve shown in **Figure 4.8**. The differentiation curve showed five main phases of decomposition, at 62, 134, 268, 360 and 452 °C. Therefore, it was observed that the synthesized non-fullerene polymer has a high degree of thermal stability which makes it a favourable potential candidate in the ongoing research for stable donor nanomaterial that produces high efficiency.

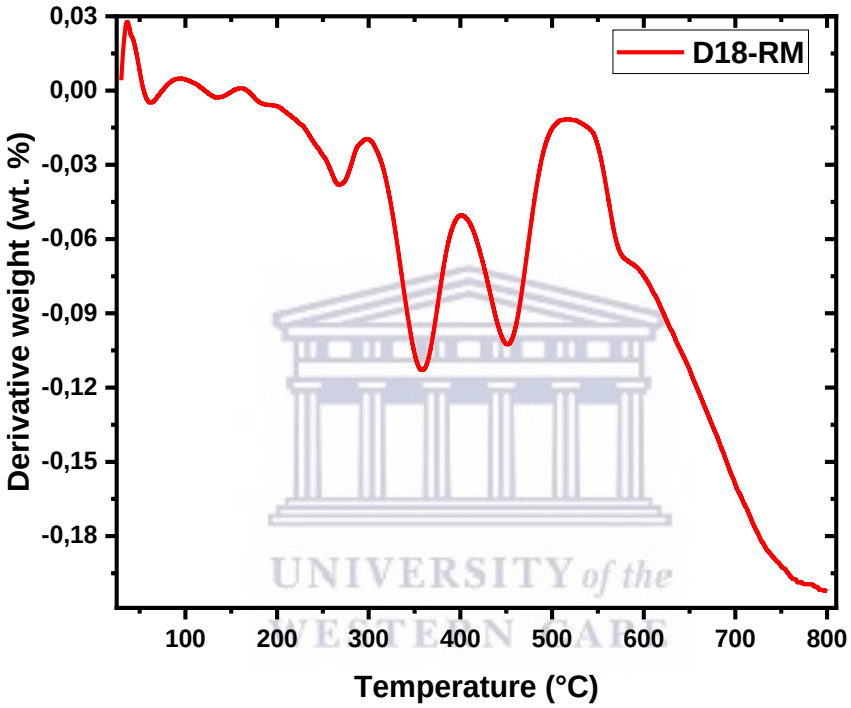

Figure 4.8 TGA differentiation curves for polymer D18-RM

4.5. The flow behavior of D18-RM using rheology

Rheological studies of polymers are one of the significant analyses that plays a vital role towards the performance an OPV device that is polymer-based. The flow behaviour of a sample is an important characteristic in the field of photovoltaic cells due to their different application such as outdoor (house or greenhouse roofing structures) or indoor applications (light-emitting diodes, fluorescent lamps etc) for deposition processes [14]. For this project, the flow behaviour of the donor polymer was investigated by employing rheological analysis. According to the claims from Glasser and co. [15], a fluid ink with a low viscosity (5−40 mPa.s) is needed for inkjet printing, while a viscous shear thinning ink with elastic behaviour or possessing a yield stress is required for doctor-blading and screen-printing deposition processes. Key properties that allow an ink to have good processability are therefore its viscosity and its rheological behaviour. The analysis provided below was performed under ambient conditions of temperature.

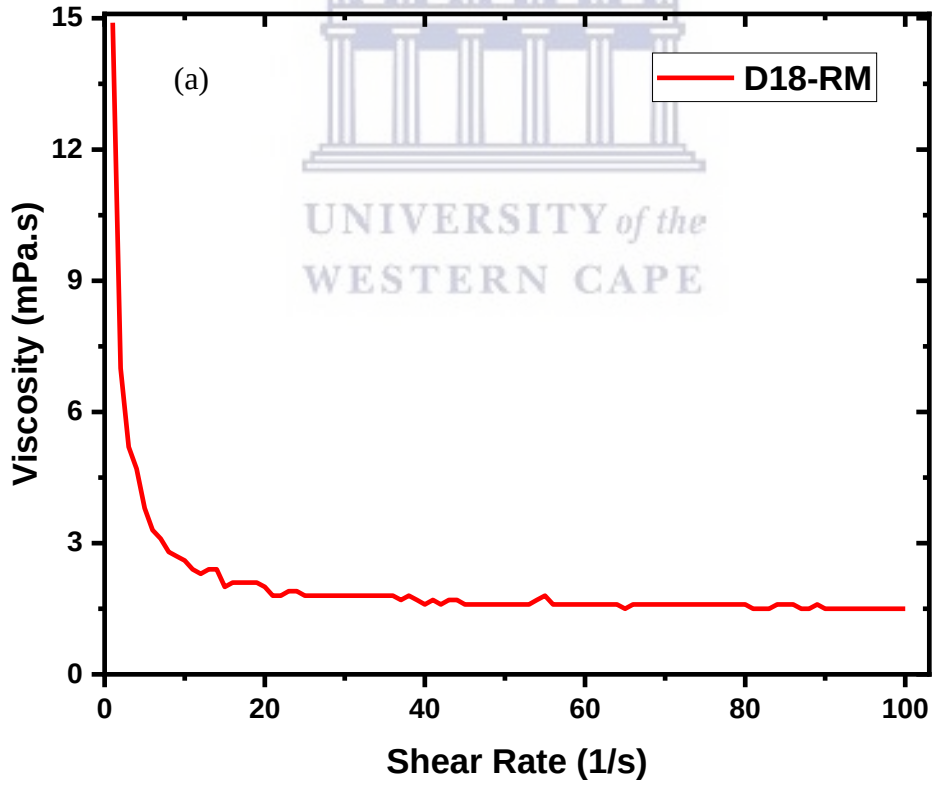

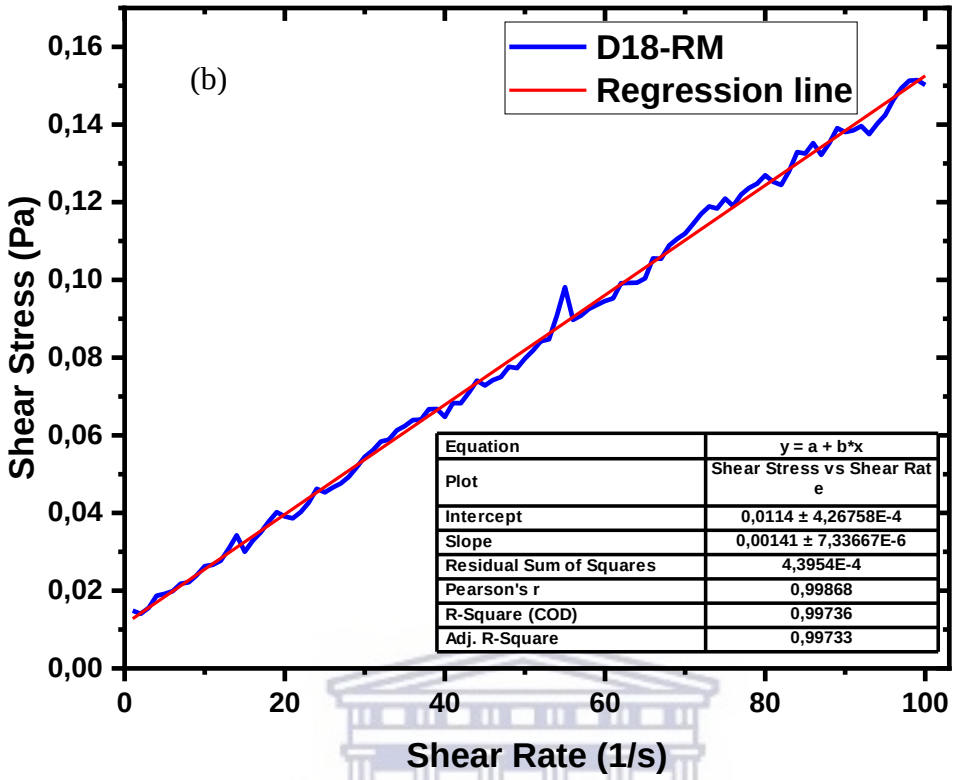

Figure 4.9: Rheological analysis of polymer D18-RM (a) viscosity curve and (b) flow curve.

Figure 4.9 (a) above shows the viscosity curve of donor polymer D18-RM that was analyzed at room temperature of the rheometer. Initially, the polymer displays a behavior of a pseudoplastic fluid (shear-thinning). However, after a shear rate of 1.34 s^{-1} the polymer becomes ideally viscous (Newtonian) and remains viscous at a viscosity reading of 1.81 mPa.s. This is a desirable property because it is within the range one would like nanomaterial to be for the fabrication processes of a highly efficient OPV device. The viscosity is calculated with the following **Equation 4.3:**

$$\eta = \frac{\tau}{\gamma} \qquad [4.3]$$

Where τ corresponds to shear stress, and γ represents shear rate. Newtonian fluids like D18-RM, follow the relation $\tau = \eta\gamma$ where viscosity η is constant (slope) and thus the relationship between shear stress and shear rate is linear. **Figure 4.9 (b)** shows the flow curve of D18-RM that represents the linear relation between shear stress and shear rate with a slope of 0.00141 Pa.s.

4.6. Optical Analysis Using Atomic Absorption and Photoluminescence Spectroscopy

4.1.1 UV-Vis Absorption for Maximum Absorbance and Bandgap Analysis

The optical absorption spectra of the synthesized D18-RM polymer, Y6 acceptor and composite D18-RM:Y6 were measured in solution in the range 350 - 700 nm. The mass ratio of composite D18-RM:Y6 was optimized to 1:0.8. The calibration of the OPV device was carried out using the dual beam method with 0% transmittance and 100% transmittance. **Figure 4.7 (a)** shows that a maximum absorbance of D18-RM in 1,2-dichlorobenze solution in the visible region corresponds to 487 nm. The shoulder peak at 387 nm in **Figure 4.7 (a)** is attributed to an unresolved vibrational-electronic (vibronic) transition [13] induced by the longer branched side chains. The shoulder is a result of the $\pi-\pi^*$ star transitions since the centre of the polymer is unsaturated and highly conjugated.

Due to the development of the shoulder, the spectrum was therefore de-convoluted to further interrogate the possible optical responses for maximum absorbance. **Figure 4.7 (b)** shows the de-convoluted absorbance of D18-RM. It can be deduced that the shoulder in the absorbance of polymer D18-RM does not affect the maximum absorbance of the nanomaterial however, it gives information about the $\pi-\pi^*$ star transitions that takes place when the polymer is exposed to light.

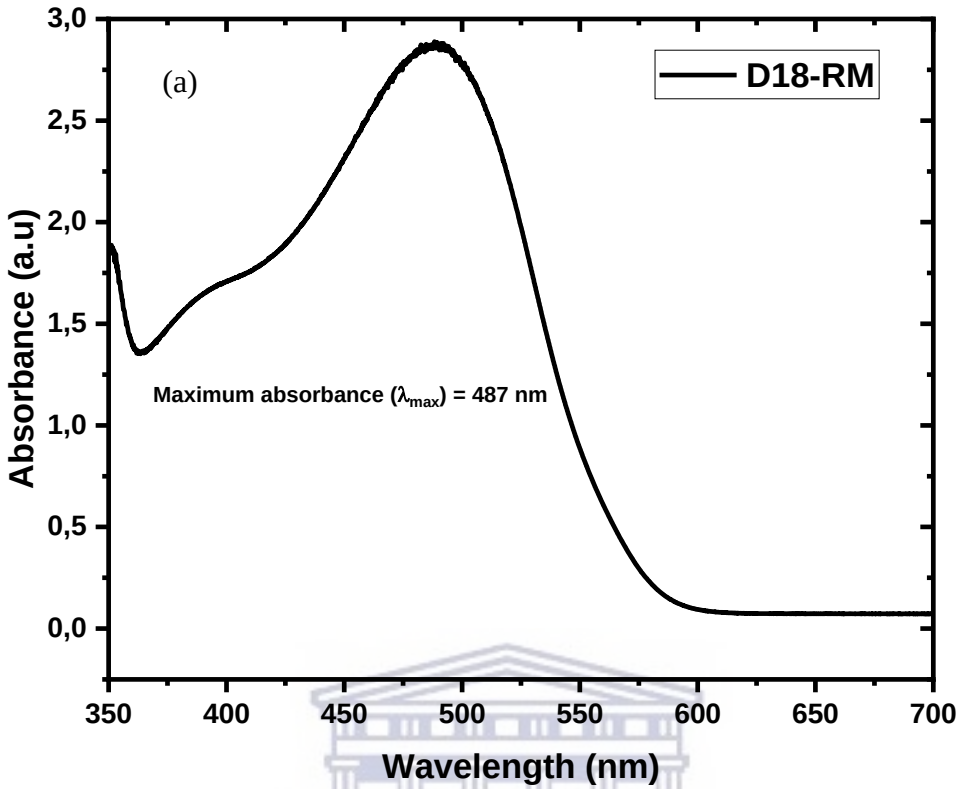

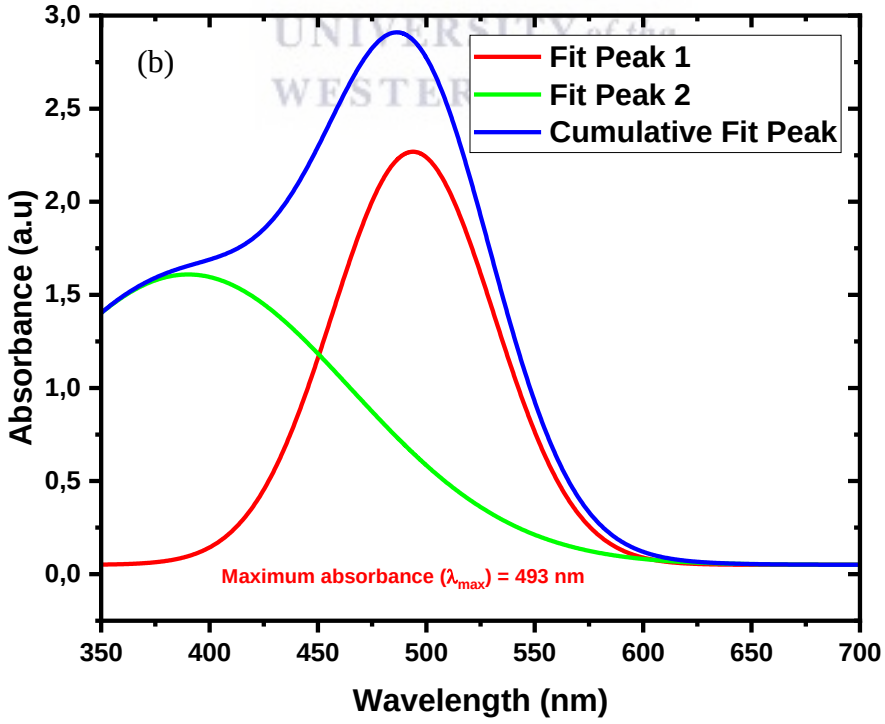

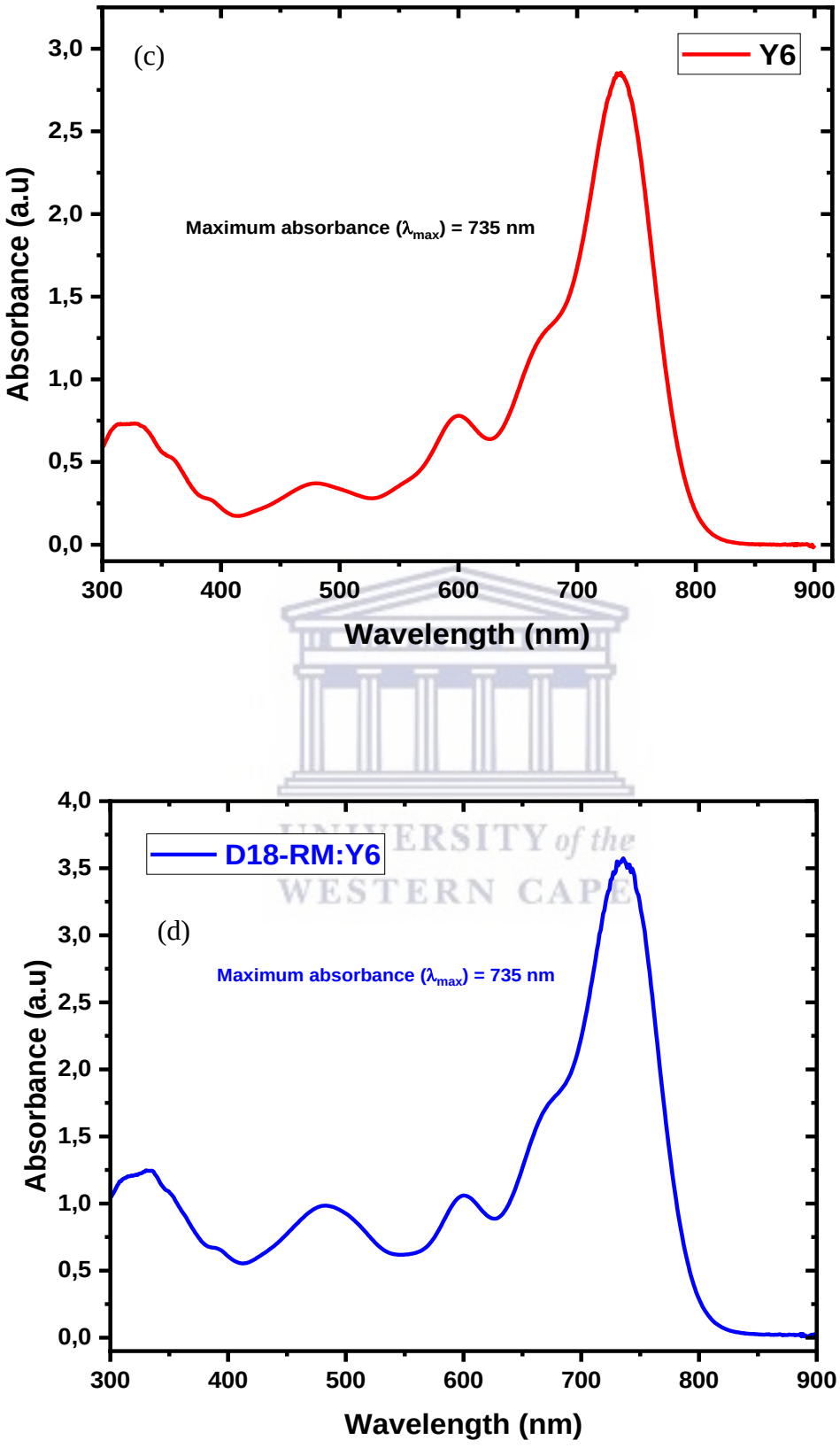

Figure 4.10 UV-Vis absorption for (a) D18-RM, (b) deconvoluted D18-RM (c) Y6 and (d) composite D18-RM:Y6

The absorbance of acceptor Y6 is given in **Figure 4.10 (c).** The maximum absorbance at 735 nm was observed that corresponds absorbance of Y6 that is also reported in literature [14] other peaks were attributed to the conjugation present in the structure. **Figure 4.7 (d)** shows the absorbance of composite D18-RM:Y6. The peaks at 600 and 345 nm are attributed to $\pi-\pi^*$ star transitions of the thienothienopyrrolo-thienothienoindole (TTP-TTI) and benzene ring of acceptor Y6, while the peak at 490 nm is due to the donor D18-RM. Therefore, this is an indication that the bulk heterojunction (BHJ) [15] was successfully formed. However, the intensity of the peak of acceptor in the BHJ is predominantly higher than that of the of the donor. This is an unfavourable characteristic which can be attributed to the quenching effect [16] that took place between the donor and the acceptor due to the optimization process for improved performance, this feature can potentially compromise the performance of the OPV device.

With the help of the optical absorption spectrum, it is well known that the Tauc analysis can be deduced to determine the optical band gap between the valence to conduction band transitions [17] as presented in **Figure 4.11** (a-b). The Tauc relation is given by the following **Equation 4.4:**

$$\alpha hv = A[hv - Eg]^n \qquad [4.4]$$

Where α is the absorption coefficient, hv is the photon energy, A is the band tailing parameter, Eg is the optical band gap, and n is either 2 for direct or ½ for indirect transitions. In this project, both transitions were examined, and the results for donor D18-RM and composite D18-RM:Y6 displayed that both nanomaterials are direct in nature, see **Figure 4.11** [18]. Hence, the bang gap of the absorption peak can be obtained by extrapolating from the Tauc plot of $(\alpha hv)^2$ vs hv to the energy axis. The optical band gaps of the nanomaterial D18-RM and D18-RM:Y6 were determined to be 2.25, and 1.57 eV, respectively. This observation enables the latter to be promising for use in organic photovoltaic cells.

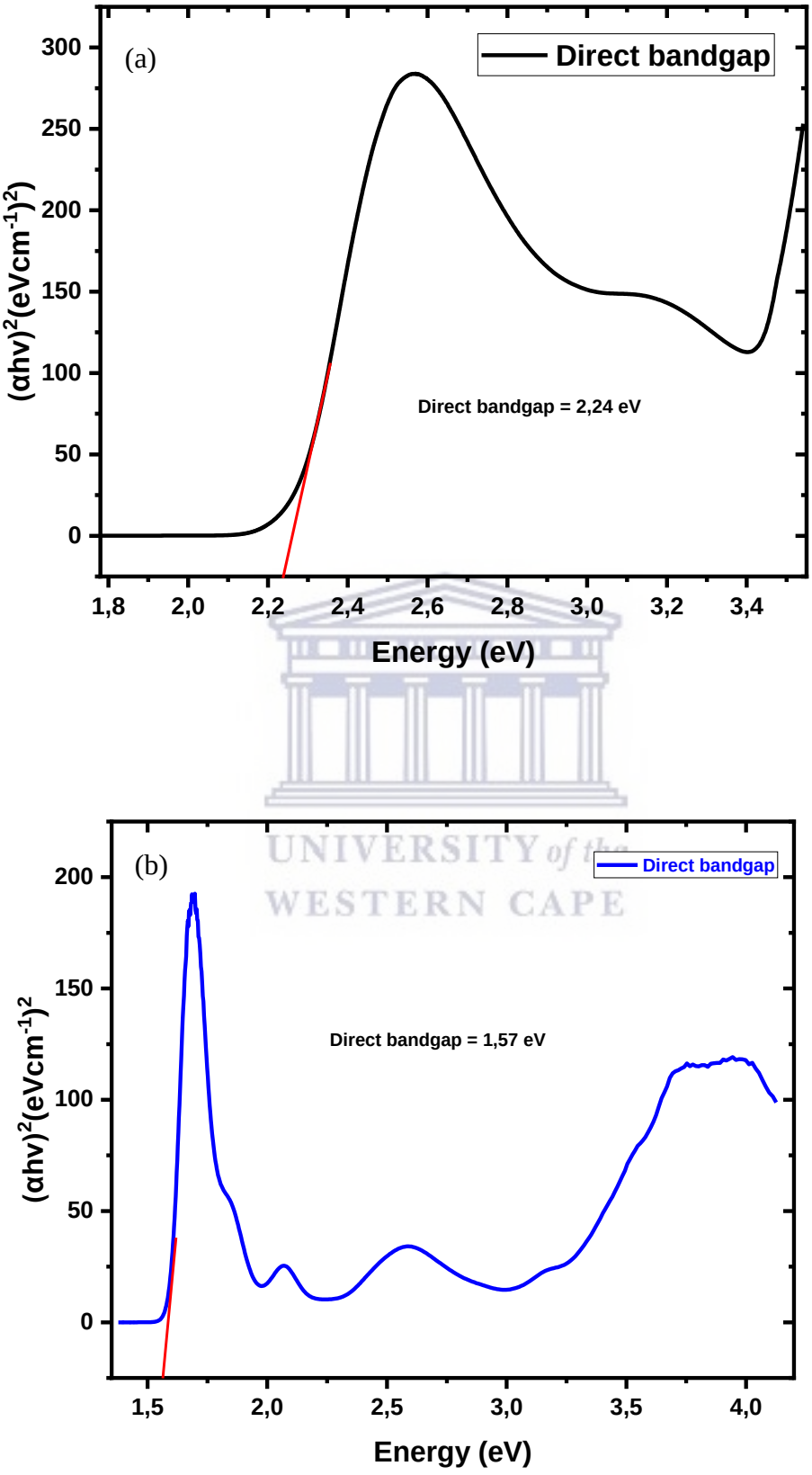

Figure 4.11 Tauc plots for bandgap calculations for (a) DM-RM and (b) D18-RM:Y6

4.1.2 Quenching Effect Using Photoluminescence Spectroscopy

Photoluminescence is a form of luminescence that occurs with a photoexcitation via photon absorption. This light emission occurs when a substance absorbs electromagnetic radiation and re-emits the radiation. This process initiates with photoexcitation. The photophysical properties of D18-RM:Y6 blend were also investigated using photoluminescence spectroscopic technique. The emission spectra were obtained using the excitation wavelength of 420 nm. The effect of photoluminescence quenching was used to study the behaviour of electron-hole pair movement [19]. From Figure 4.9 photoluminescence intensity of D18-RM decreased after blending with Y6. This photoluminescence quenching effect [20] is associated with transfer of charges between D18-RM and Y6. Consequently, the carrier charges from donor which were meant to return from excited state to ground state are transferred to the acceptor leading to the reduction in photoluminescence intensity.

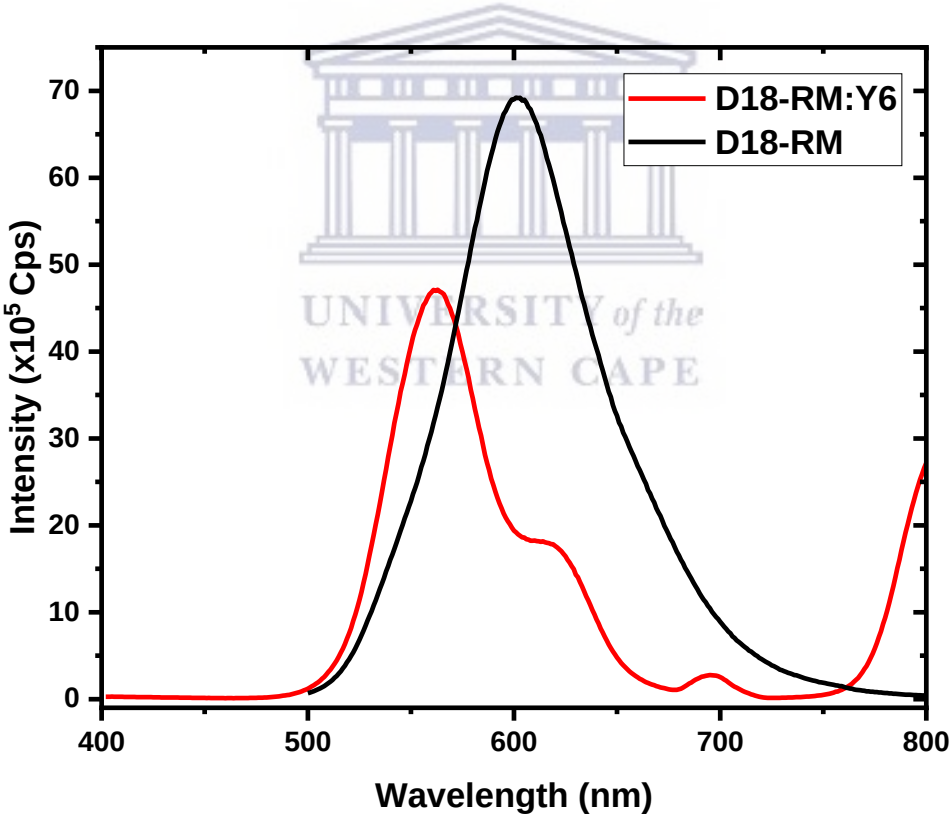

Figure 4.12 Overlaid Photoluminescence spectra of D18-RM polymer and D18-RM:Y6 blend.

To further understand this quenching effect, one can introduce a relative quenching coefficient (η) [21] that is calculated by following **Equation 4.5:**

$$\eta = (I_D - I_A)/I_A \quad [4.5]$$

Where I_D and I_A are the intensities of the PL peak of the polymer and composite, respectively. About 74% of the photoluminescence intensity of donor D18-RM was quenched when it was blended with Y6 acceptor. This quenching effect of D18-RM intensity indicates successful splitting of electron-hole pair and transfer of electrons from donor, D18-RM to acceptor, Y6. Theoretically, all the intensity of the donor and acceptor blend must not give any intensity to indicate a complete electron-hole pair separation and charge transfer [22]. Therefore, a blend that result to higher quenching percentage has sufficient electron-hole pair separation and charge transfer.

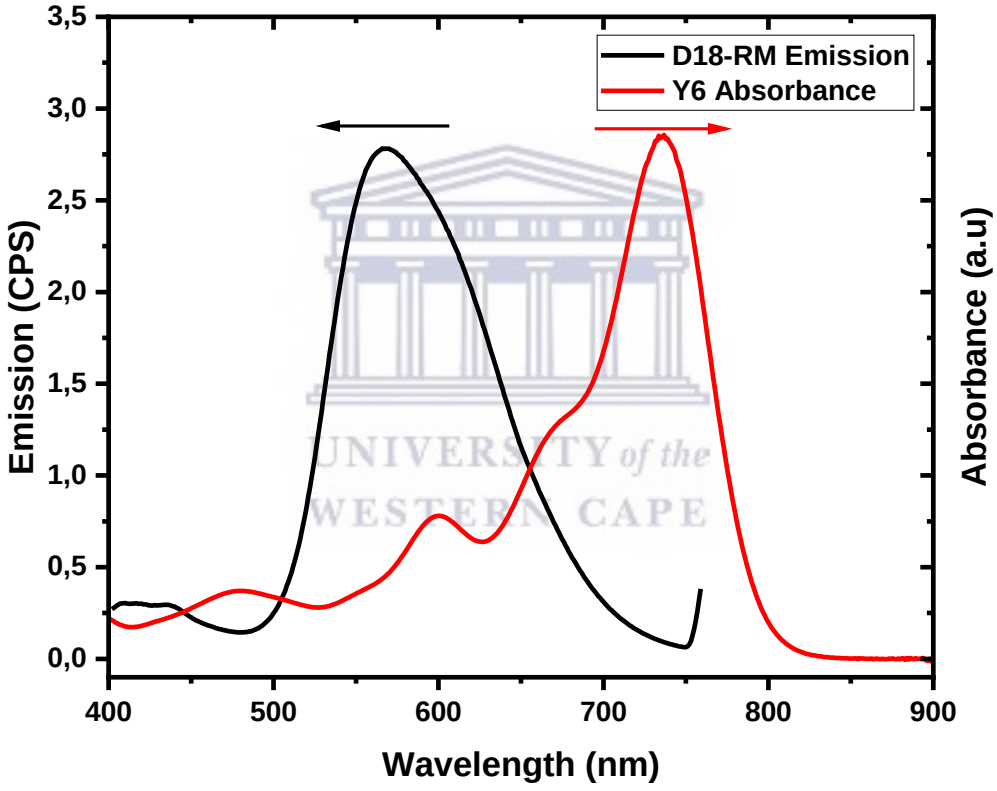

Figure 4.13 Absorption and emission spectra of D18-RM (donor) and Y6 (acceptor) as a fluorescence resonance energy transfer pair.

For a highly efficient OPV device, it is strongly recommended to employ orthogonal solvents [23] for layer deposition for a minimal layer intermixing, and choose active nanomaterial pairs with strong resonant overlap for interlayer Förster resonance energy transfer analysis [24], along with high absorption coefficients and low Stokes shifts [25] to maximise exciton diffusion lengths relative to absorption length within layers. The Stokes shift between D18-RM (donor) and Y6 (acceptor) was found to be 170 nm. However, it is more difficult to find

suitable orthogonal solvents as displayed in **Figure 4.13**, since they are typically dissolved in similar solvents with conjugated polymers. One simple way is by forcibly dissolving insulating polymers into the solvent, which requires heating and a long agitation time which is the method that was utilised during the fabrication of the OPV device of this project.

4.7. Morphological and Elemental Analysis.

The morphology of the synthesized polymer and composite was investigated using Scanning electron microscope (SEM), Atomic Force Microscope (AFM) and Transmission Electron Microscopy (TEM). All the analysis were performed on a thin film. The significance of using SEM even though it has small domains was to determine the surface shape of the synthesized nanostructured polymer. The micrographs obtained from TEM were utilized to analyse any form of agglomeration that could be formed by the nanoparticles of the polymer while AFM images were taken to study the roughness of the surface formed by the nanomaterial of the polymer when it is coated on an ITO. AFM showed a good homogeneity as there are no pinholes in between the single crystals. Pinholes influence the efficiency of solar cells; they specifically affect the short circuit current and open circuit voltage in contrasting ways as reported by Zhu *et al.* [26].

4.7.1 Shape and Surface Analysis by SEM

As part of morphological studies, SEM technique was employed as one of the techniques to study the surface arrangement of the polymer and the composite. The SEM results for both polymer donor and composite are presented with different magnifications in Figure 4.10 below. The SEM image of polymer D18-RM shown in **Figure 4.14 (a-c)** depicted flake-like structures with a cubic shape along with a large number of aggregated globular structures, which is in accordance with the observations made by Leonard et al [27]. The introduction of Y6 acceptor on the backbone of D18-RM shows morphological changes as small particles are observed on the surface of D18-RM and there is also an agglomeration, as shown in **Figure 4.10 (d-f)**. No pinholes were apparent from all magnifications that were done during the analysis. This then confirms the presence of Y6 on D18-RM forming a composite D18-RM: Y6.

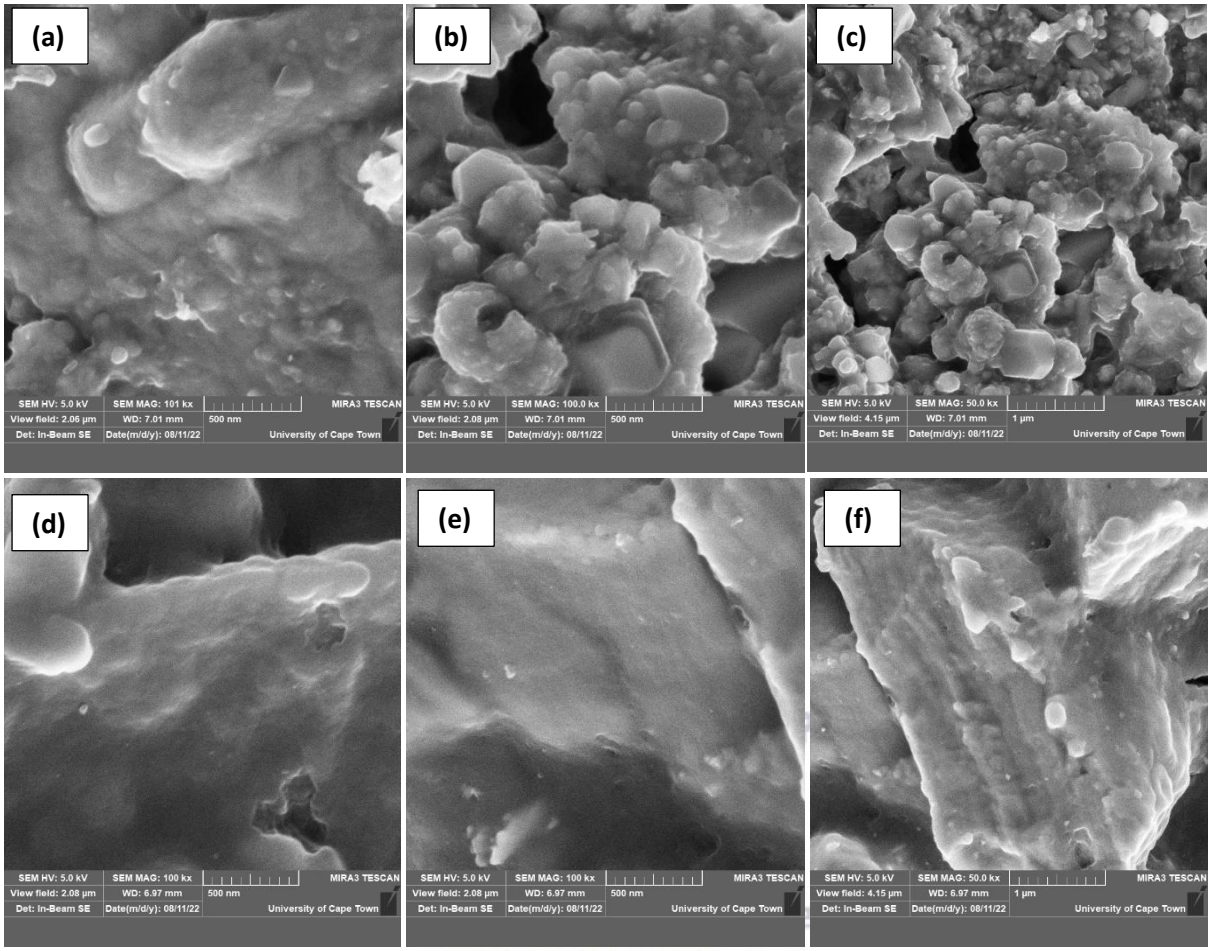

Figure 4.14 SEM images of (a-c) D18-RM and (d-f) D18:Y6 composite annealed at 60°C for 5 minutes

4.7.2 Surface Roughness and Topographical Analysis by AFM Scanning Mode

AFM technique was utilised to further interrogate the surface morphology of the polymer and the composite. As it is well known, AFM provide information about the surface roughness of the sample which has a substantial impact on the electrons and quasi particle holes movement between the donor and acceptor nanomaterial, thus also affecting the overall performance of the OPV device.

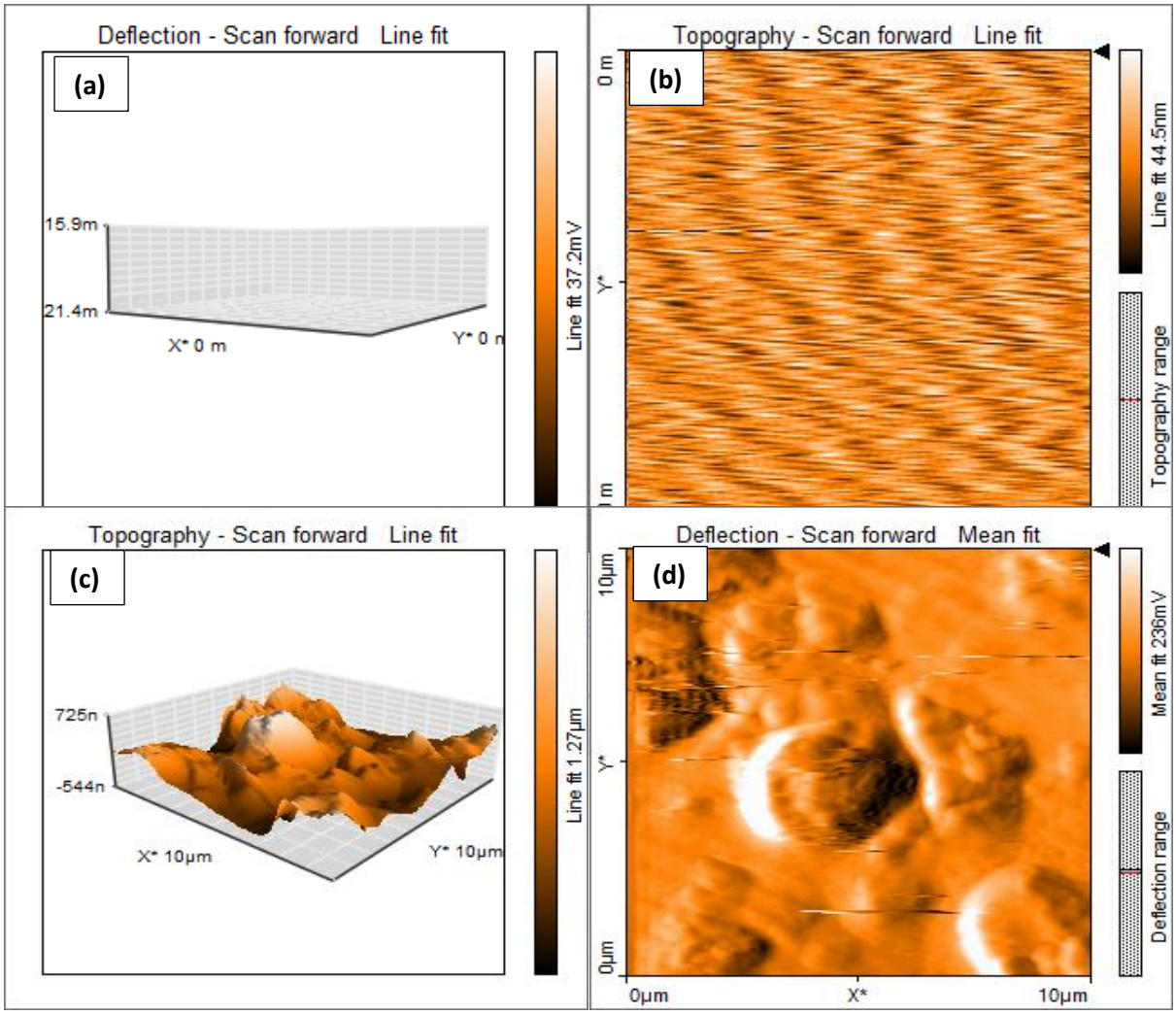

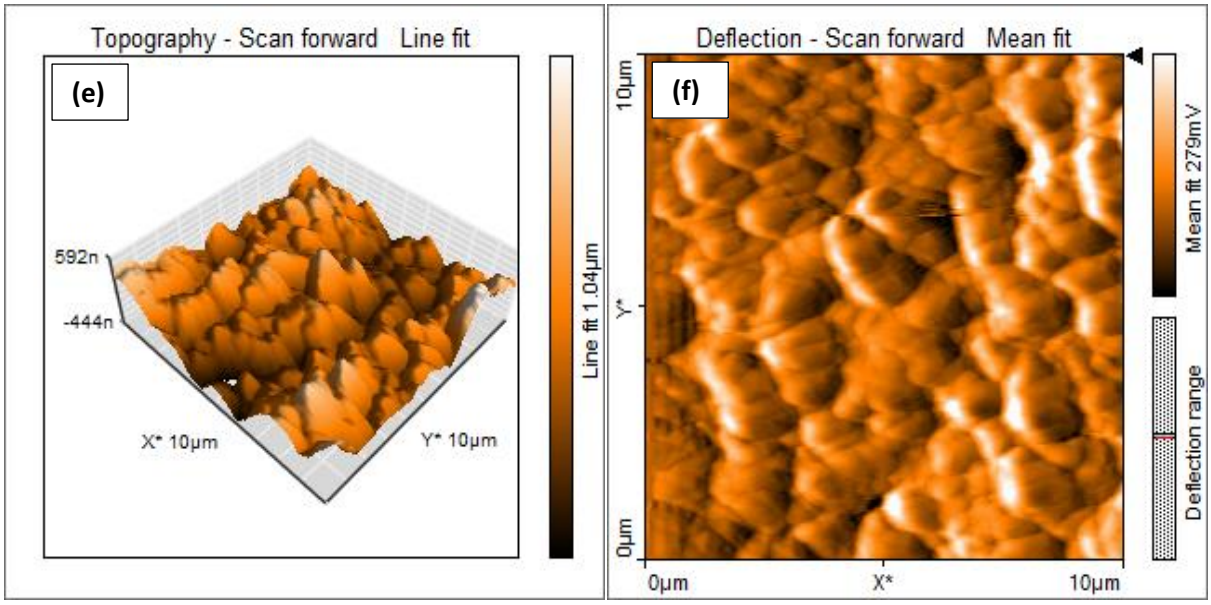

Figure 4.15 AFM images for (a-b) blank ITO substrate and (c-d) D18-RM thin film and (e-f) D18-RM:Y6 thin film coated on ITO substrate

Figure 4.15 above show two different sets of AFM images that carries information for a blank ITO substrate **Figure 4.15** (a-b), D18-RM thin film **Figure 4.15 (c-d)** and D18-RM:Y6 composite thin film coated on ITO substrates **Figure 4.12 (e-f)**. The average roughness (Ra) and root mean square roughness (Rq) for polymer D18-RM was found to be 259.41 nm and 315.95 nm respectively, and for composite D18-RM:Y6 Ra and Rq was 118.92 nm and 145.6 nm. These were indeed quite higher than expected and the way in which this issue can be addressed is to find the thickness of the thin films, which will lead to suitable spin coating speed and sample size. According to the literature from Kumar et al [28], for a Gaussian distribution of asperity height, statistical theory shows that the ratio of Rq and Ra should be 1.25.

According to the calculations Ra/Rq is 1.22 for both D18-RM and D18-RM:Y6. These results are important since they indicate that the imaging scale, the asperity height of distribution of these surfaces are approximately Gaussian and the statistical relationships for surface roughness are applicable and that show that the synthesized nanomaterial promise to have a positive impact on the performance of the OPV device.

4.7.3 HR-TEM Analysis for Particle Size Distribution

The size distribution (**Figure 4.16**) of the synthesized nanomaterial of the polymer was studied and evaluated. **Figure 4.16 (a-b)** shows the images particle size and **(c-f)** are the TEM images of D18-RM and composite D18-RM:Y6 respectively. The micrographs acquired from TEM showed that the nanoparticles of the polymer were agglomerated forming large nanoparticle clusters. The average particle size for D18-RM is 14 and 12,5 nm for D18-RM and composite D18-RM:Y6 respectively. These results showed that the aim to synthesize and form a D18-RM:Y6 composite nanostructured nanomaterial for the OPV device was successfully achieved.

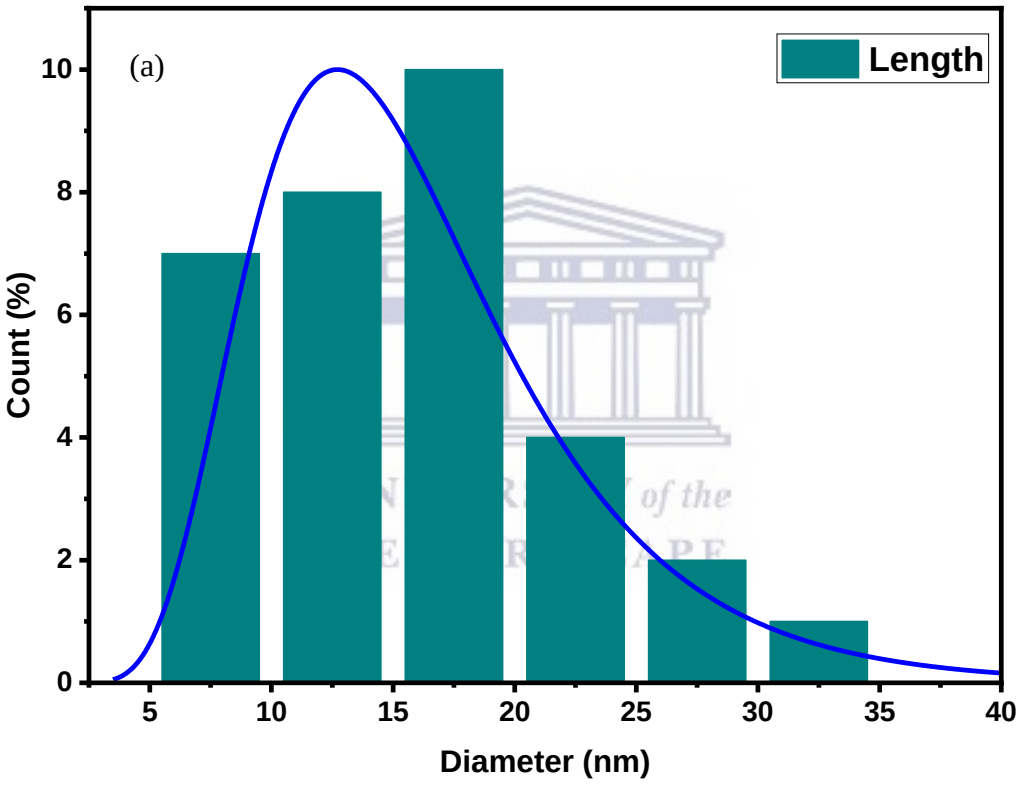

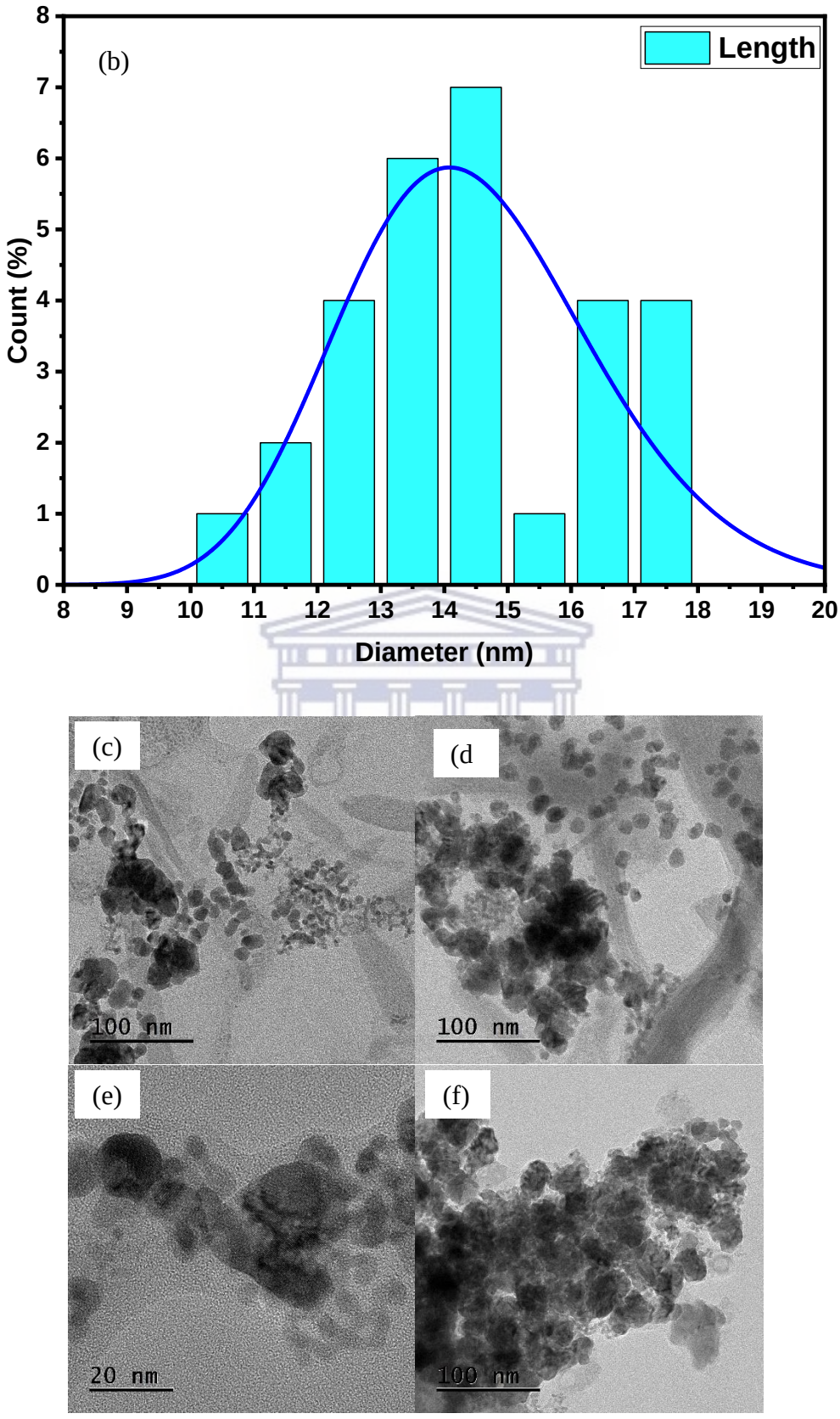

Figure 4.16 HR-TEM images (a-b) and (c-d), (e) and (f) shows the particle size distribution for polymer D18-RM and composite D18-RM:Y6

4.8. Electrochemical Kinetics of Electron-Hole Pair

Electrochemistry of active nanomaterial is one of the most important analysis for potential usage of these nanomaterials as semiconductors for photovoltaic applications [29]. In order to decide the possible usage of a nanomaterial as a semiconductor, its electrochemical response should be generally determined. For these purposes in this work, the electrochemical characterisation of D18-RM and D18-RM:Y6 was investigated with voltametric measurements such as cyclic voltammetry (CV) and square wave voltammetry (SWV) to determine the HOMO and LUMO which leads to the determination of the electrochemical band gap. Electrochemical Impedance Spectroscopy (EIS) was also utilised to get information about the impact of the morphology of the nanomaterial on the charge transfer dependency and the resistance of the nanomaterial thereby fitting the appropriate Randle circuit cell onto the EIS plot to get parameters such as charge transfer resistance (Rct) and series resistance (Rs).

4.8.1 CV Analysis for Electron-Hole Movement

In order to understand the electrochemical response of the synthesized polymer D18-RM, CV measurements for donor D18-RM, acceptor Y6 and composite D18-RM:Y6 were all carried out at 100 mV/s scan rate to acquire redox information about the three nanomaterials and the voltammograms are shown in **Figure 4.17**. It was observed that the oxidation peaks from CV were 1.27, 1.60 and 1.72 eV, while the reduction peaks were -1.47, -1.75 and -1.45 eV for D18-RM, Y6 and D18-RM:Y6 respectively. A huge dispersion from the redox values above is noticeable and also it was observed that D18-RM, Y6 and composite D18-RM:Y6 nanomaterials have characteristics of either reversible or quasi-reversible behaviour. However, to fully describe electrochemical reversibility of a nanomaterial it is important to consider not only the value of the electron-hole transfer rate constant, but the scan rate as well.

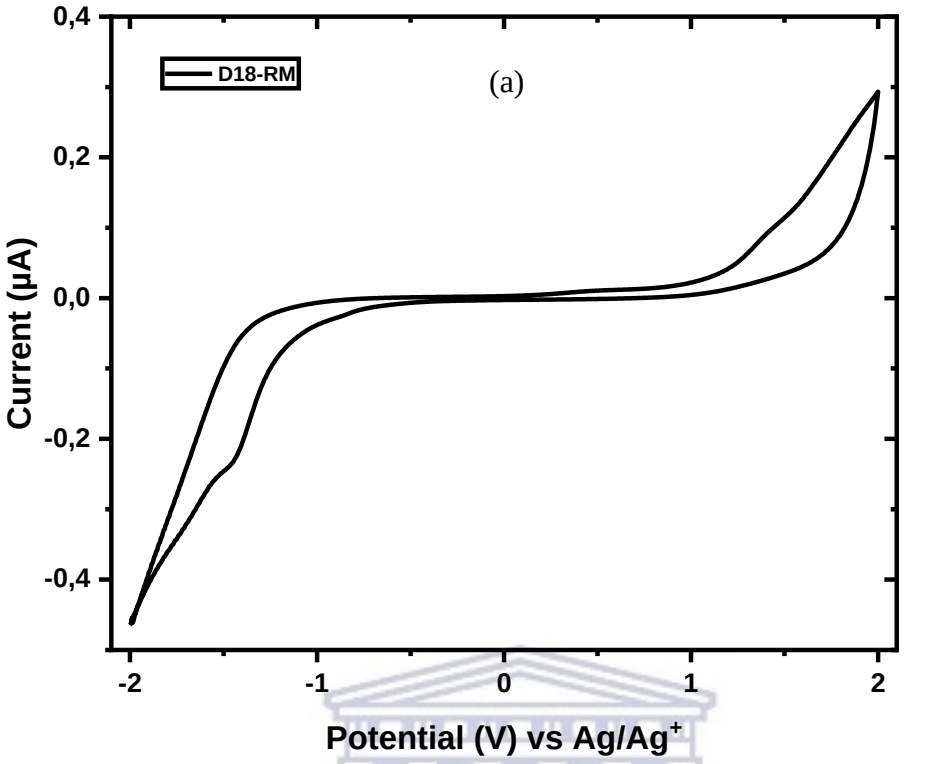

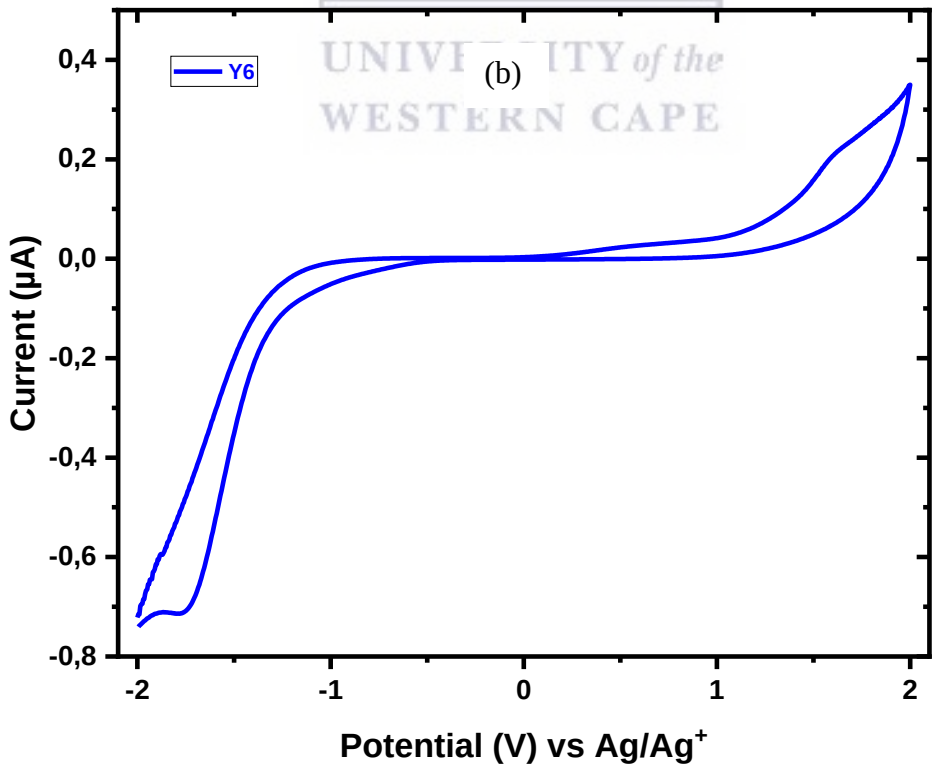

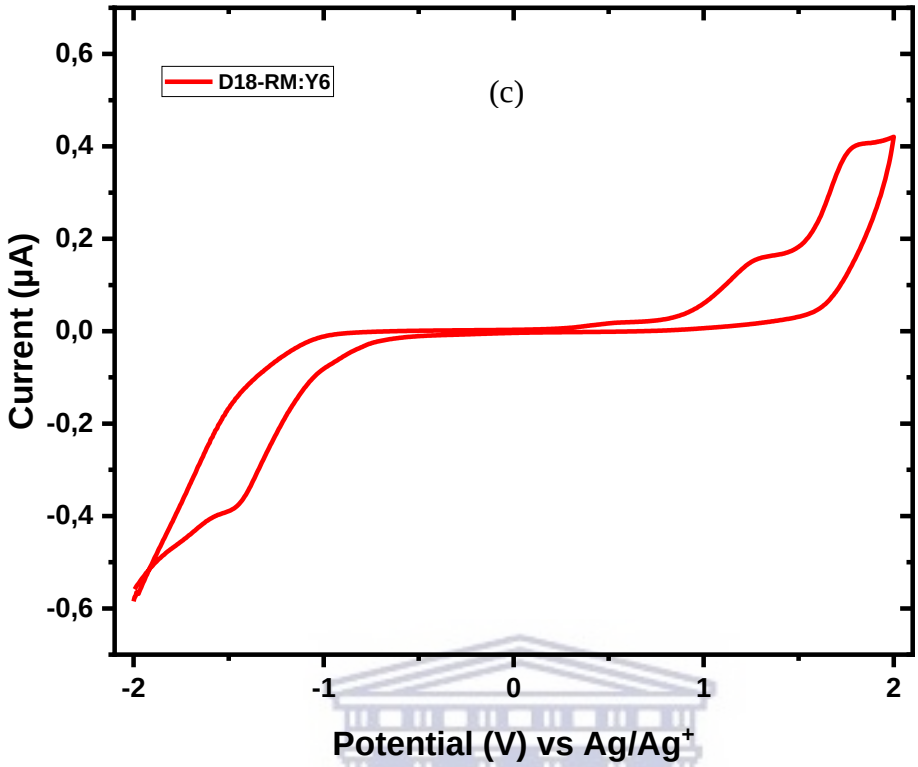

Figure 4.17 Cyclic voltammograms of (a) D18-RM, (b) Y6 and (c) D18-RM:Y6 at 100 mV/s scan rate

As stated above, the electrochemical reversibility cannot be deduced from the rate constant only, scan rate is also an important parameter to confirm this behaviour. Hence, the scan rate study from CV was performed for D18-RM, Y6 and D18-RM:Y6 using different scan rates, starting from 100 to 10 mV/s. From **Figure 4.18** It was apparent that redox peak currents increase linearly as a function of scan rate. The unfavourable dispersion between the redox values for D18-RM, Y6 and D18-RM:Y6 was still apparent even after the 10 scans of each nanomaterial. It is also worth mentioning that electrochemical reversibility of Y6 is limited to higher scan rates, this was deduced from the voltammograms of Y6 in **Figure 4.1 (b)**. After the scan rate of 30 mVs Y6 displayed no clear peak for oxidation and reduction.

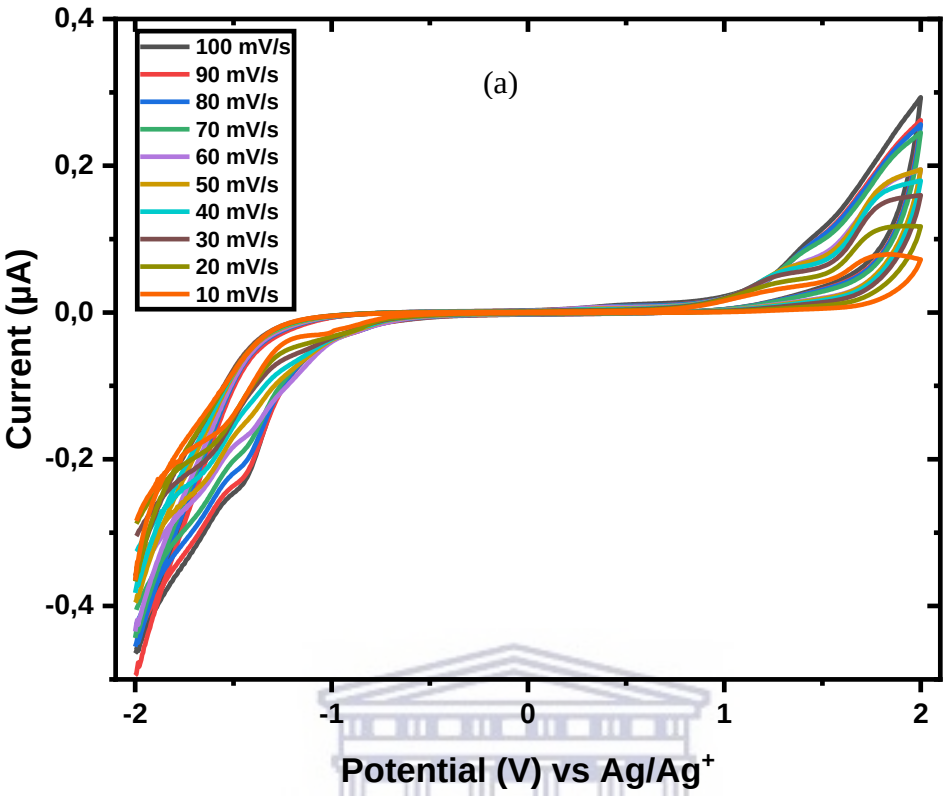

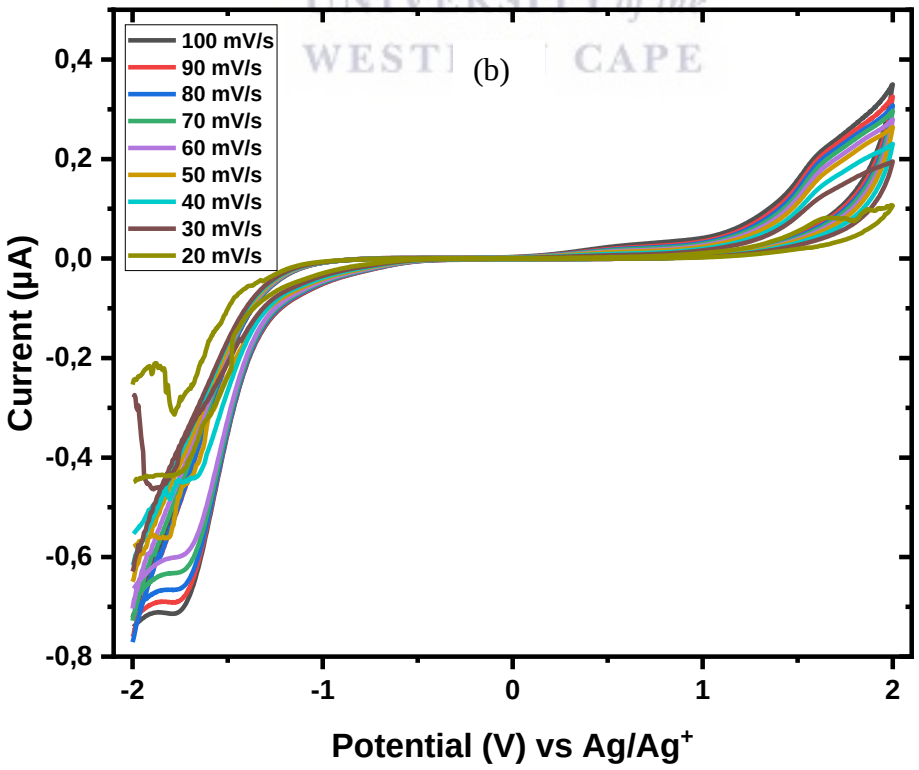

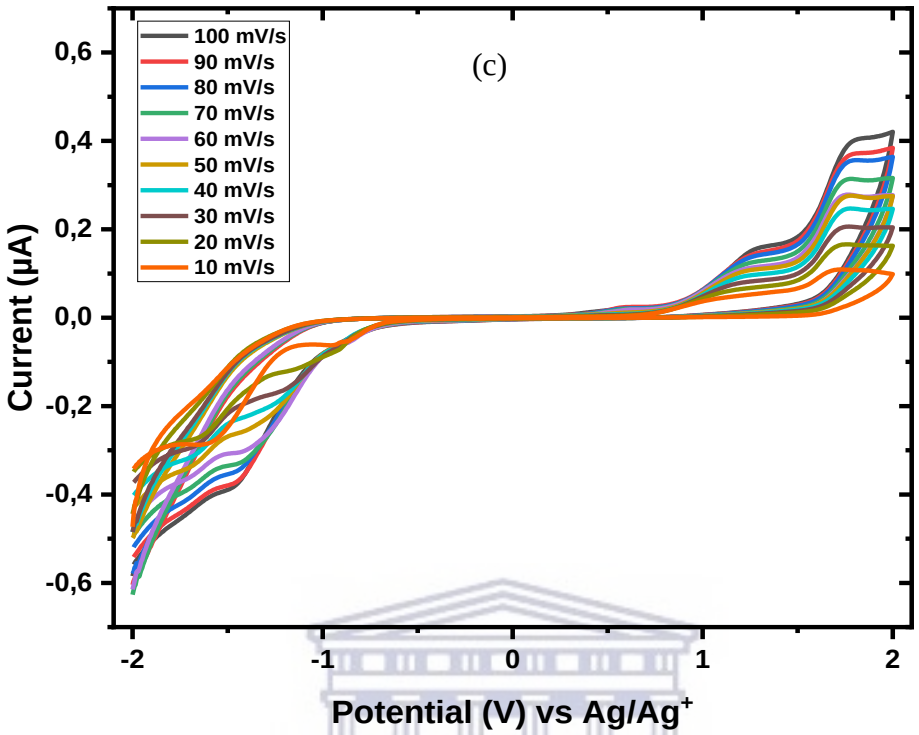

Figure 4.18 Cyclic voltammograms of (a) D18-RM, (b) Y6 and (c) D18-RM:Y6

4.8.2 Square-Wave Voltammetry for redox value confirmation

CV measurements solely are not 100% accurate for in-depth analysis of electrochemical reversibility behaviour of nanomaterials, as a result, another technique is required to confirm the results from CV and SWV is one of the most reliable and accurate technique that can be employed. This is because square-wave is a more sensitive voltammetry technique than CV and can easily detect any electroactivity on the electrode surface faster and produce more pronounced redox peak currents. In this work, SWV was utilised to confirm the oxidation and reduction peaks discussed in section 4.8.1 above. **Figure 4.19** below shows the SWV voltammograms measured within the same potential range as those for CV. As expected, the voltammograms show different oxidation and reduction peaks for all 3 nanomaterials.

Oxidation peak for donor polymer D18-RM was observed to be 0.71 eV, meanwhile Y6 acceptor showed two peaks at 0.84 and 1.26 eV and composite D18-RM:Y6 displayed three peaks at 0.64, 1.24 and 1.70 eV. The dispersion that was encountered under CV analysis was eliminated and these values were then used as formal potential to conduct the EIS analysis.

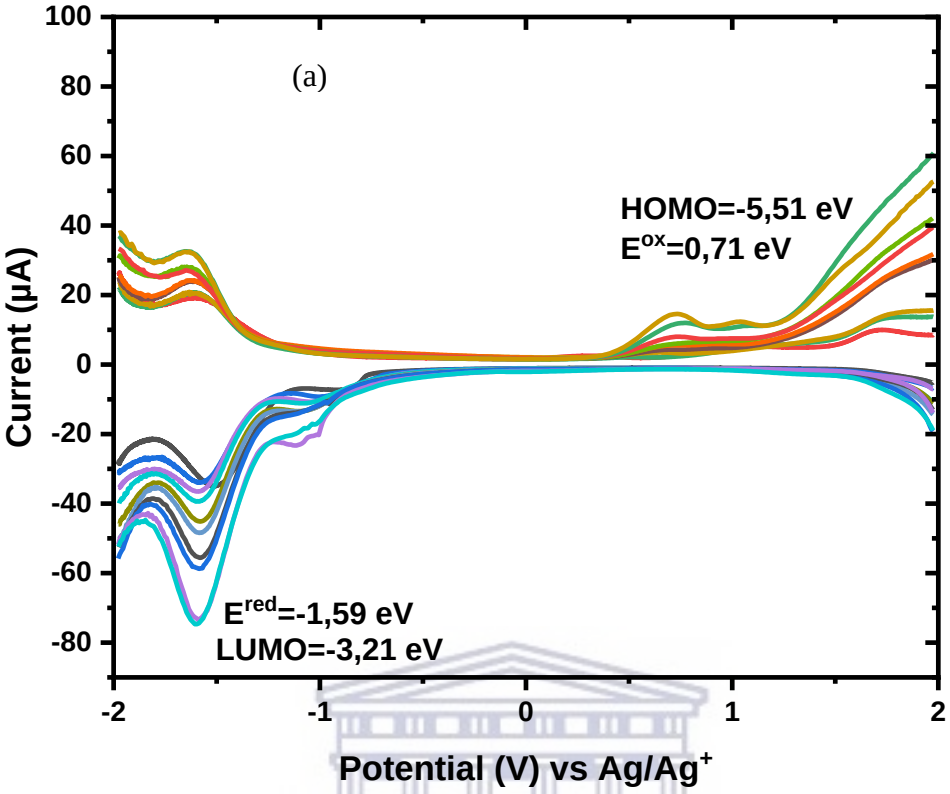

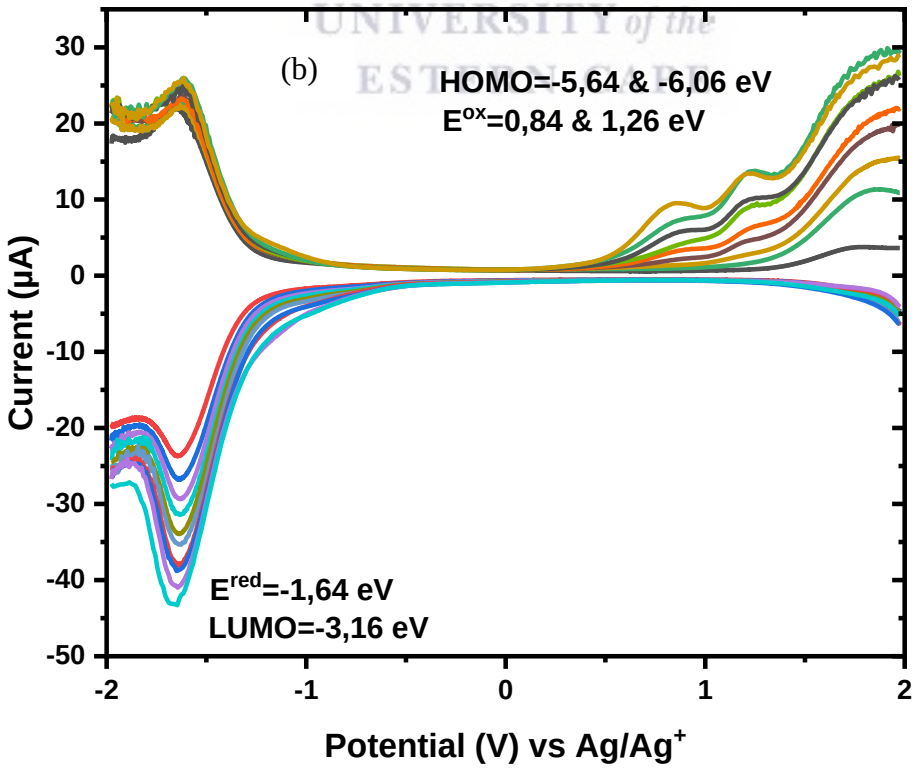

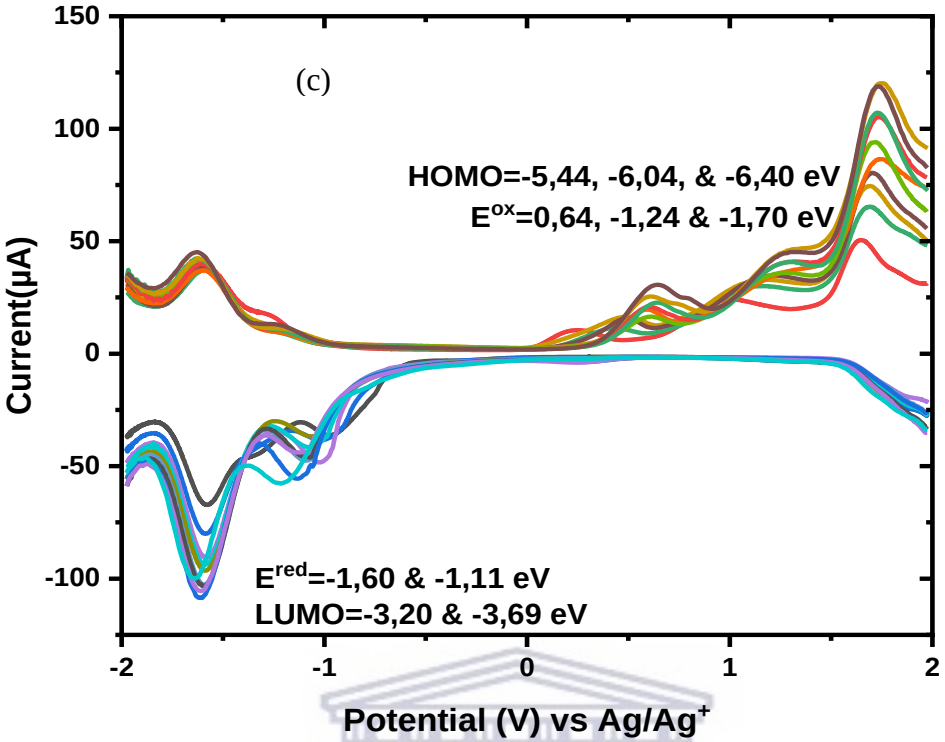

Figure 4.19 Square-wave voltammograms of (a) D18-RM, (b) Y6 and (c) D18-RM:Y6

4.8.3 Randle Sevcik Scan Rate Study

The scan rate study was also carried out in solution for D18-RM, Y6 and D18-RM:Y6 nanomaterial with 1,2-dichlorobenzene as solvent. The produced information about electron generation and charge transfer (CT) was used to calculate the diffusion coefficient of the three nanomaterials. According to De Menezes *et al.* the diffusion ascribes to changes in viscosity due to mass transport particularly for these polymers [30] thus, thermal activation at constant rate is important. The diffusion coefficient of the three nanomaterials was calculated by plotting the anodic and cathodic peak current values against the square root of the different scan rates (10 mV/s to 100 mV/s) as shown in **Figure 4.20** below. With the help and estimation from CV, the number of electrons transferred for the polymers was calculated using **Equation 4.6:**

$$| E_p - E_{\frac{p}{2}} | = \frac{2.303RT}{nF} \qquad [4.6]$$

Rearranged as:

$$n = \frac{59.19mV}{| E_p - E_{\frac{p}{2}} |}$$

Where n is the number of electrons, Ep is the formal potential, Ep/2 is half-peak potential, R is gas constant, T is temperature in Kelvin and F is Faraday constant. By making n the subject of

the formula and 2.303 RT divided by F having a value of 59.19 mV at 25 ˚C, where 2.303 RT has a value of 0.593 kcal/mol at 25 ˚C and F is 23.06 kcal/mol V. The number of electrons transferred during the redox reaction was calculated to be 2. Knowing this number of electrons transferred, the Brown Anson equation [31] was used to estimate the concentration (c) of the adsorbed electro-active species using the anodic peak current (Ipa) obtained at 100 mV/s. We used surface concentrations instead of bulk concentrations because the equilibrium position for the redox reaction. The surface concentration of the adsorbed electro-active species of D18-RM, Y6 and D18-RM:Y6 was calculated to be $1.31 \times 10^{-3}, 9.98 \times 10^{-3}$ and 7.94×10^{-3} $mol.cm^{-3}$ respectively, see Brown Anson equation ***Equation 4.7:***

$$i_p = \frac{n^2 FcAv}{4RT} \quad [4.7]$$

Since the donor-acceptor (D-A) interface is a 3D surface due to the bulk heterojunction formed, the surface concentration does not necessarily determine the total number of electro-active species in the bulk heterojunction of OPV. Therefore, the values of the surface concentration above still require further interpretation. The rate of diffusion of the nanomaterials is the speed at which a nanomaterial can diffuse through another nanomaterial through mass transfer and it can be calculated using the Nicholson-Shain equation [32]. A condensed Randle-Sevcik equation for a temperature condition of 25 ˚C was used to evaluate the diffusion coefficient of the three nanomaterials. The is given as **Equation 4.8:**

$$i_p = 2.69 \times 10^5 n^{\frac{3}{2}} Ac\sqrt{vD} \quad [4.8]$$

Rearranged as:

$$D = \sqrt{\frac{slope}{2.69 \times 10^5 n^{\frac{3}{2}} Ac}}$$

where slope = i_p divided by square root of scan rate, n is the number of electrons during redox reaction which has the value of 2 from calculation, A is the surface area of the electrode (ITO substrate electrode surface area of used 0.020 cm^2) and c is the concentration of the nanomaterial studied for analysis. The D value was for the forward half-reaction was determined to be 7.85×10^{-5} cm^2/s. This implies that electron transfer processes of polymer D18-RM are occurring at a much faster rate, and this can be attributed to the combination of the unique properties of monomer DTBT and BDTOESn when forming D18-RM which seem to act as a polyelectrolyte, thus accelerating the rate of flow of ions going in and out of the electrode surface. The rest of the other D values are summarized in **Table 1** below.

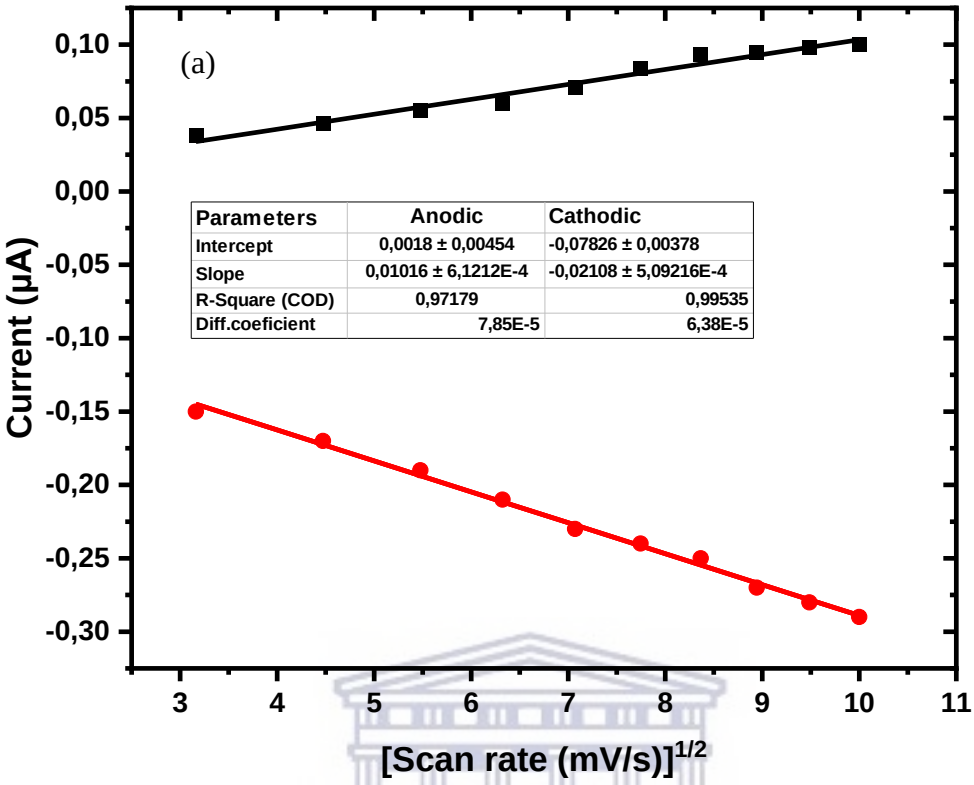

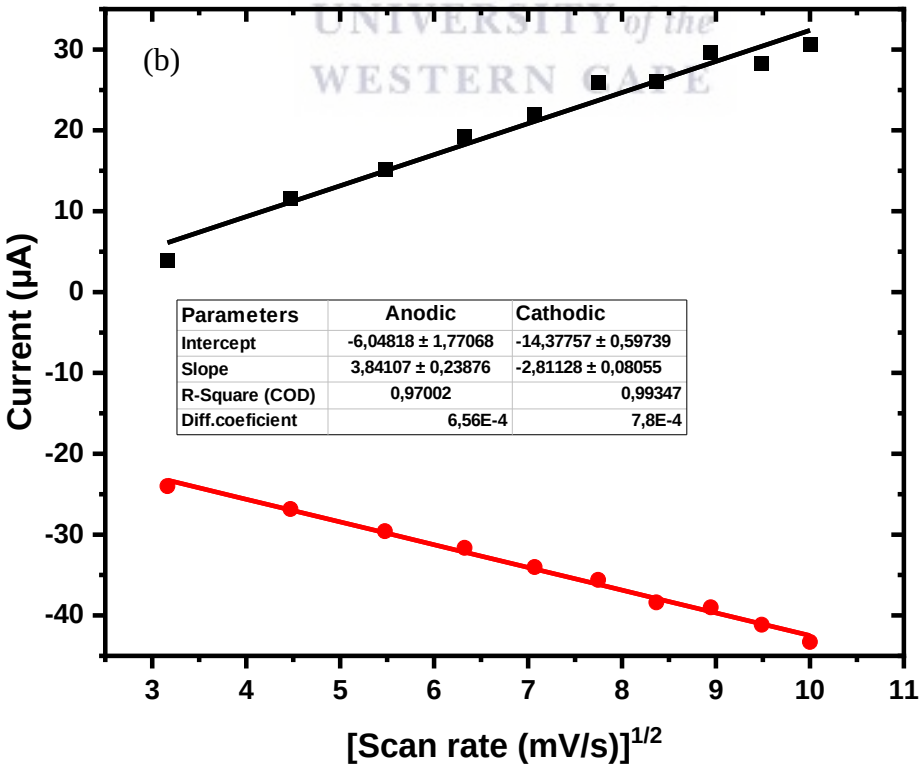

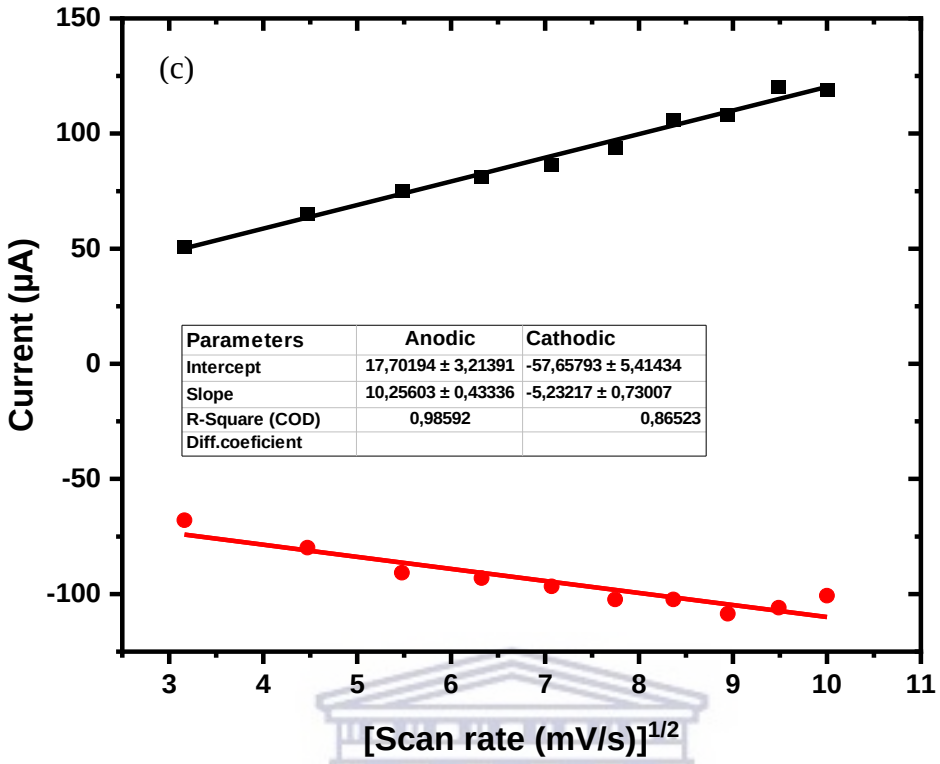

Figure 4.20 Randles-Sevcik plot for (a) D18-RM, (b) Y6 and (c) D18-RM:Y6

Table 4.1 Electrochemical parameters of all the polymers

	D18-RM	Y6	D18-RM:Y6
Surface concentration, c, (mol/cm^2)	0.0013100	0.0099800	0.0079400
Anodic diffusion coefficient, D, (cm^2/s)	0.0000786	0.0006560	0.0000409
Cathodic diffusion coefficient, D, (cm^2/s)	0.0000638	0.0007800	0.0000377
No. of electrons, n	4	2	2

4.8.4 EIS Analysis

EIS is an important electrochemical technique in that its spectra can be analysed to determine the different types of resistance. It is well suited for characterizing intra-gap states in fully functional photovoltaic cells under controlled conditions [33]. The resistive losses in the electrodes and bulk resistance in the active layer are represented by series resistance (Rs) and, charge transfer resistance (Rct) represents an aggregate of interfacial resistance between the active layer and cathode interfacial layers, and donor/acceptor interfacial resistance. The spectra can be plotted in two ways Bode plot and Nyquist plot. Nyquist plot shows the relation

between the imaginary impedance and real impedance and Bode plot is the plot of total Impedance (sometimes called magnitude) against frequency both as logarithm values and phase angle against frequency where frequency is in logarithm form.

For the purposes of this study, the EIS experiment was conducted in solution. The equivalent circuit was used to fit the semicircle curves as shown in **Figure 4.21**, and the extracted parameters are summarized in **Table 4.2**.

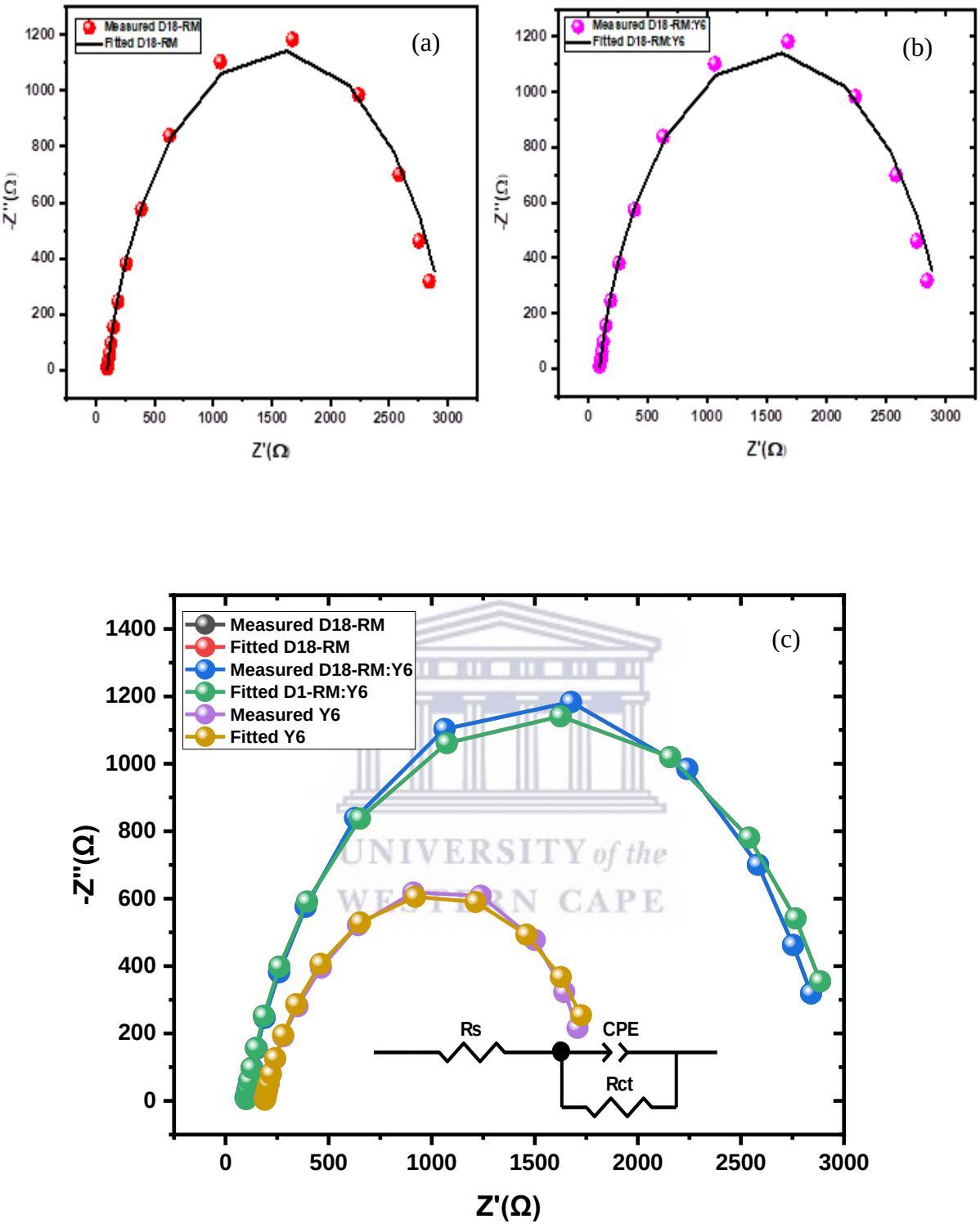

Figure 4.21 Fitted Nyquist plot of (a) polymer donor D18-RM, (b) composite D18-RM:Y6 and (c) overlaid plots of donor, acceptor and composite

The electrochemical impedance spectra obtained for D18-RM, Y6 and D18-RM:Y6 are depicted in **Figure 4.21** above. Due to overlapping, D18-RM plots (both measured and fitted) are not visible in **Figure 4.21 (c)**, their individual plots are displayed in **Figure 4.21 (a)** and **(b)**. The Nyquist plot was used to study charge carrier migration in an electrochemical cell in the form of two types of resistance, namely: solution resistance (Rs) and charge transfer resistance (Rct). Rs account for the overall resistance of the cell while Rct is related to the diameter of the semicircle at the interface of an electrode and sample [34]. The smaller the diameter of the semicircle, the fast the diffusion of charges through the sample to the electroactive surface of the electrode [35]. The Nyquist plot showed one semicircle at the higher frequency that corresponds to the mass transfer of the three nanomaterials. From the fitted Nyquist plots of figure 4.16, the Rs for D18-RM, Y6 and D18-RM:Y6 were found to be 117.6, 190.1 and 98.63 Ω respectively. Concurrently, the Rct values for D18-RM, Y6 and D18-RM:Y6 were 2383, 1663 and 2924 Ω respectively.

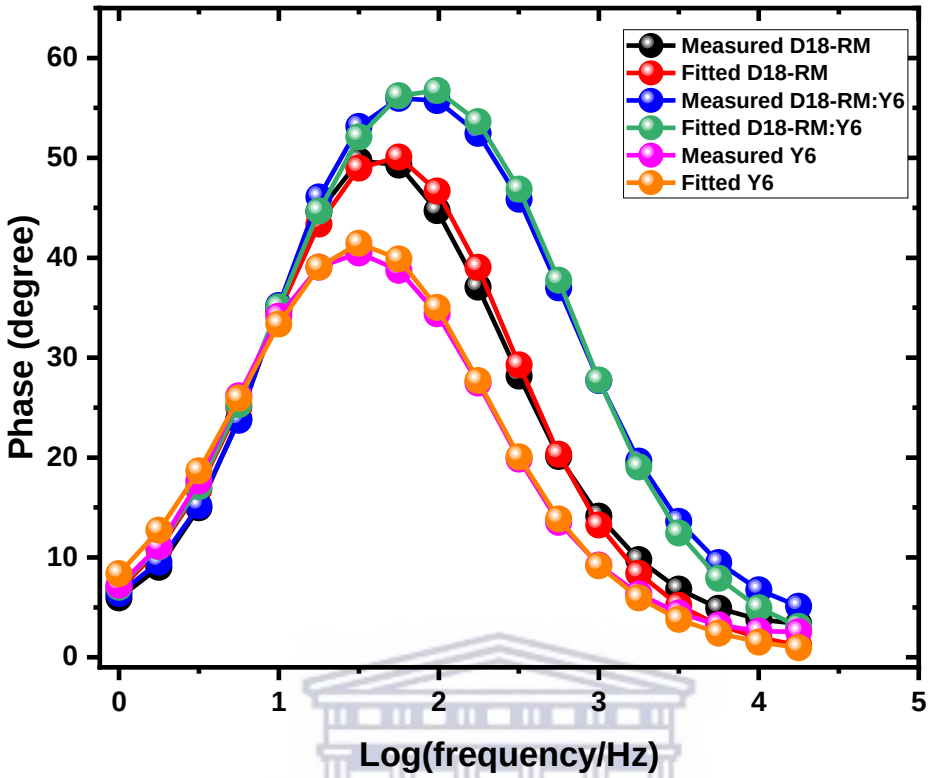

Figure 4.22 Overlaid fitted and measured Bode-Phase plot of polymer donor D18-RM, acceptor Y6 and composite D18-RM:Y6

The model to determine the recombination rates from the EIS data is to utilise vacuum processing system because in a vacuum processing, the Fermi level E_F is shifted towards the HOMO and holes are generated in the anode phase, which fill up intra-gap states. Hence, the signal can be attributed to holes only [36]. The Bode-phase plots for the three nanomaterials are indicated in **Figure 4.22** above. It is observed that the peak of composite D18-RM:Y6 shifts towards lower frequency range in **Figure 4.22**. This observation confirms the increase of recombination rate and shorter electron lifetime (τ) [37]. Electron lifetime in organic photovoltaic cells is a central quantity to determine the recombination dynamics in the cell to understand the overall performance of the OPV device. An increase in τ relates to blocking of electrode electrolyte at the interface due to hindrance of insertion/extraction of electrolyte ions. The values of τ were calculated using **Equation 4.9:**

$$\tau = \frac{1}{2\pi f_{max}} \qquad [4.9]$$

f_{max} is the angular frequency at the maximum impedance [38]. The values of τ for D18-RM, Y6 and D18-RM:Y6 were calculated to be 0.0925, 0.105 and 0.0829 s respectively. The constant phase element (CPE) is a capacitive element with a frequency-independent negative phase between current and voltage which interpolates between a capacitor and a resistor [39]. In this project, CPE behaviour was interpreted as a statistical distribution of time constants due to the crystal orientation, surface roughness, and resistance distribution in the polymer layer of the electrode surface. A summary of the CPE values is provided in **Table 4.2** below.

Table 4.2 Resistance properties

	D18-RM	**Y6**	**D18-RM:Y6**
Series resistance, Rs (Ω)	117.6	190.1	98.63
Constant phase element, CPE-T (Ω)	0.000011569	0.000024929	0.0000098104
Constant phase element, CPE-P (Ω)	0.862480000	0.807410000	0.8445900000
Charge transfer resistance (Ω)	2383.000000	1663.000000	2924.0000000
Time constant, τ (s)	0.092500000	0.105000000	0.0829000000

Figure 4.23 below depicts the bode plot of impedance against frequency for the three nanomaterials. It was observed that D18-RM:Y6 has maximum impedance at higher frequency than D18-RM and Y6, this feature was attributed to the high conjugation of the polymer which advocates for the circulation movement of π-electrons within the molecule, thus enhancing the electrochemical impedance of the composite. These findings suggest poor conduction of composite D18-RM:Y6 and are in agreement with the higher Rct and shorter lifetime value obtained above.

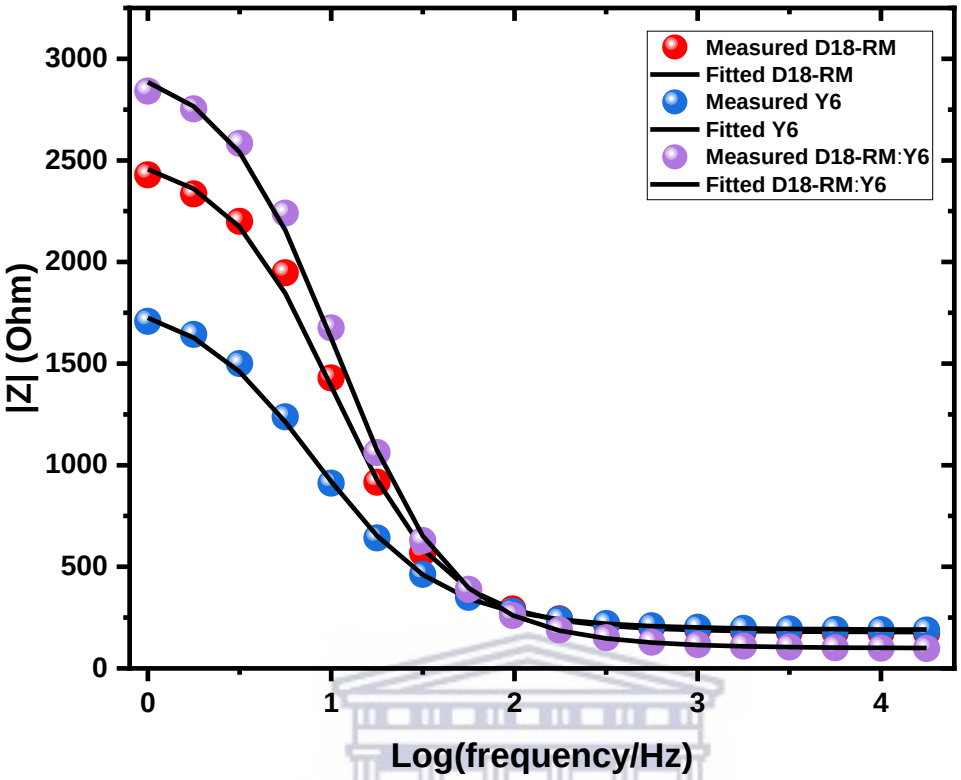

Figure 4.23 Overlaid measured and fitted Impedence-Bode plot of polymer donor D18-RM, acceptor Y6 and composite D18-RM:Y6

4.9. Photovoltaic properties of D18-RM:Y6

The photovoltaic properties of this OPV nanomaterials were investigated with J-V characteristics. J-V analysis of D18-RM and D18-RM:Y6 was performed to further analyse the charge transfer kinetics at the interface of counter electrode (CE) and electrolyte using a symmetric cell configuration. **Figure 4.24** shows the Tafel curves for the D18-RM and D18-RM:Y6.

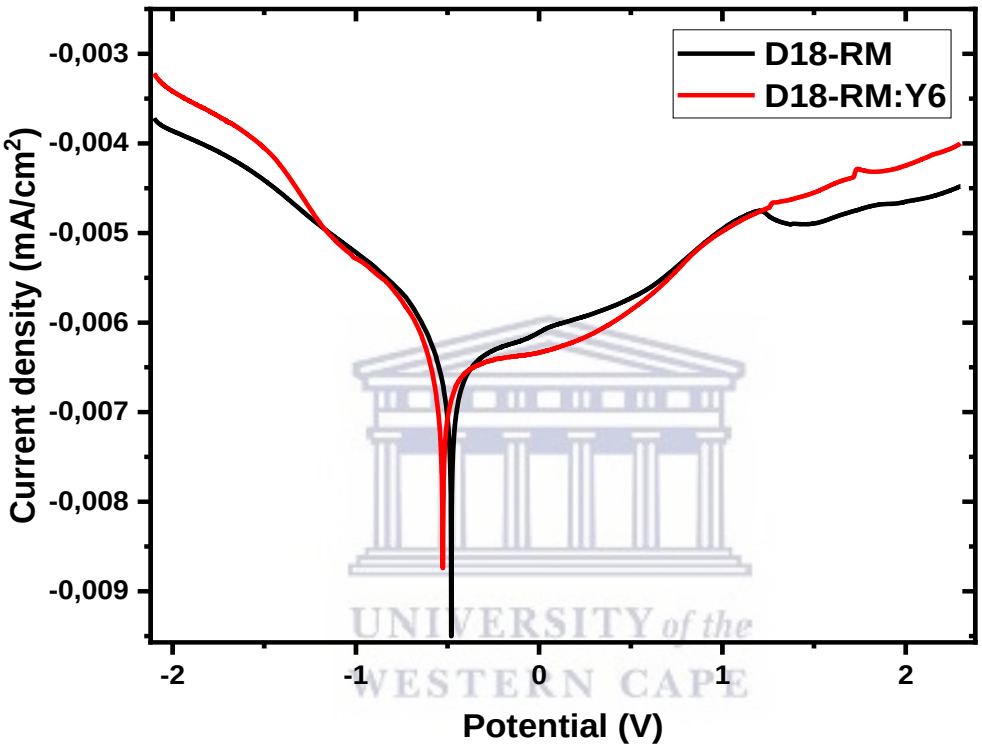

Figure 4.24: Tafel plot of polymer D18-RM and composite D18-RM:Y6

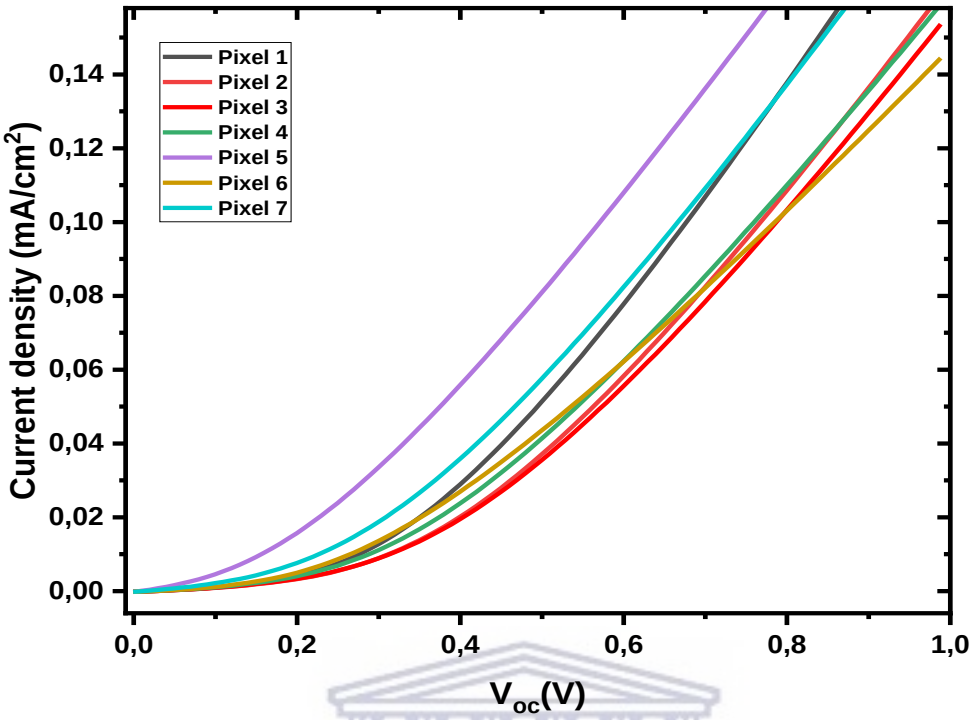

Figure 4.25 J-V characteristics of OPV device D18-RM:Y6 measured outside glovebox

In the J-V curve, the tangent slope of the cathodic or anodic branch with the equilibrium potential details the information about the exchange current density (J_0) [40] on the electrode. The J_0 value for D18-RM:Y6 is a higher than that of D18-RM although they display to have equal potential (0.5V). This confirms the better catalytic activity of the as-synthesized D18-RM. The exchange current density (J_0) can be calculated using **Equation 4.10:**

$$J_O = \frac{RT}{nFR_{ct}} \quad [4.10]$$

Where R is a gas constant, T is absolute temperature, n is the number of electrons involved in the redox reaction and F is the Faraday's constant. From the equation, the higher J_0 value implies the lower Rct involvement of the electrode. Branch of the cathodic line with the y-axis illustrates that the slopes for the anodic/cathodic lines of the D18-RM:Y6 are only slightly steeper than those of the D18-RM CE [41]. From **Figure 4.25**, the diffusion zone showed a slightly higher limiting diffusion current density (J_{lim}) value for D18-RM:Y6 than D18-RM CE, showing its good diffusion property.

The current density-voltage (J-V) curve of the OPV device with the structure of glass|ITO|ZnO|D18-RM:Y6|Ag conductive paste is shown in **Figure 4.25** below. The maximum performance of the OPV device gave PCE of 0.0011%, short circuit current (J_{SC}) of 21.04 mA/cm^2, fill factor (FF) of 27.7% and open circuit voltage (V_{OC}) of 0.024 V. The PCE and the fill factor (FF) can be calculated according to the following **Equations 4.11*:***

$$PCE = \frac{Voc \times Jsc \times FF}{P_{max}} \quad [4.11]$$

And

$$FF = \frac{V_{max} \times Jmax}{Voc \times Jsc} \quad [4.12]$$

where Voc (V), Jsc (mA/cm^2), FF, and Pmax (mW/cm^2) are the open-circuit potential, short-circuit current density, fill factor, and incident-light power, respectively. Vmax (V) and Jmax (mA/cm^2) are the voltage and current density at the point of the maximum power output, respectively.

4.10. References

[1] T. Kosugi, M.; Sasazawa, K.; Shimizu, Y.; Migita, "Stille-coupling," pp. 1–38, 2014.

[2] G. E. Bachers and T. Schaefer, "Applications of the intramolecular nuclear overhauser effect in structural organic chemistry," *Chem. Rev.*, vol. 71, no. 6, pp. 617–626, 1971, doi: 10.1021/cr60274a002.

[3] "Nuclear Overhauser Effect (NOE)".

[4] Chemistry Database, "Infrared spectroscopy absorption Table - OChemOnline," *LibreTexts*, pp. 1–6, 2020, [Online]. Available: https://chem.libretexts.org/@go/page/22645

[5] F. Huang *et al.*, "Can Isotope Effects Enable Organic Solar Cells to Achieve Smaller Non-Radiative Energy Losses and Why?," *Cite This Chem. Mater*, vol. 2022, pp. 6009–6025, 2022, doi: 10.1021/acs.chemmater.2c01067.

[6] X. Yi *et al.*, "Effects of polymer crystallinity on non-fullerene acceptor based organic solar cell photostability," *J. Mater. Chem. C*, vol. 8, no. 45, pp. 16092–16099, 2020, doi: 10.1039/d0tc03969a.

[7] A. Zerr, G. Serghiou, R. Boehler, and M. Ross, "Decomposition of alkanes at high pressures and temperatures," *http://dx.doi.org/10.1080/08957950600608931*, vol. 26, no. 1, pp. 23–32, Mar. 2007, doi: 10.1080/08957950600608931.

[8] E. S. Freeman and B. Carroll, "The application of thermoanalytical techniques to reaction kinetics. The thermogravimetric evaluation of the kinetics of the decomposition of calcium oxalate monohydrate," *J. Phys. Chem.*, vol. 62, no. 4, pp. 394–397, 1958, doi: 10.1021/j150562a003.

[9] J. Lim *et al.*, "Selective Soxhlets extraction to enhance solubility of newly-synthesized poly(indoloindole-selenophene vinylene selenophene) donor for photovoltaic applications," *Nano Converg.*, vol. 7, no. 1, 2020, doi: 10.1186/s40580-020-0219-9.

[10] A. Tripodi and I. Rossetti, "Aspects of the thermogravimetric analysis of liquid mixtures as predictive or interpretation tool for batch distillation," *J. Therm. Anal. Calorim.*, vol. 147, no. 12, pp. 6765–6776, 2022, doi: 10.1007/s10973-021-10990-1.

[11] K. Otsuka, S. Kobayashi, and S. Takenaka, "Catalytic decomposition of light alkanes, alkenes and acetylene over Ni/SiO2," *Appl. Catal. A Gen.*, vol. 210, no. 1–2, pp. 371–379, 2001, doi: 10.1016/S0926-860X(00)00831-0.

[12] E. Gallicchio, M. M. Kubo, and R. M. Levy, "Enthalpy-entropy and cavity decomposition of alkane hydration free energies: numerical results and implications for theories of

hydrophobic solvation," *J. Phys. Chem. B*, vol. 104, no. 26, pp. 6271–6285, 2000, doi: 10.1021/jp0006274.

[13] S. Chatterjee, Y. Ie, and Y. Aso, "Naphtho[1,2- c:5,6- c′]bis[1,2,5]thiadiazole-Based Nonfullerene Acceptors: Effect of Substituents on the Thiophene Unit on Properties and Photovoltaic Characteristics," *ACS Omega*, vol. 3, no. 5, pp. 5814–5824, 2018, doi: 10.1021/acsomega.8b00350.

[14] L. Lu and M. Effendy, "Application of organic photovoltaic materials (OPV) as greenhouse roof structures: A review," *J. Agric. Food Eng.*, vol. 1, no. 3, pp. 1–5, 2020, doi: 10.37865/jafe.2020.0019.

[15] A. Glasser, É. Cloutet, G. Hadziioannou, and H. Kellay, "Tuning the Rheology of Conducting Polymer Inks for Various Deposition Processes," *Chem. Mater.*, vol. 31, no. 17, pp. 6936–6944, 2019, doi: 10.1021/acs.chemmater.9b01387.

[16] H. T. Sato, M. Araki, T. Oyama, and K. Tsukiyama, "Laboratory Optical Spectroscopy of Vibronic Transitions of the Thiophenoxy Radical," *Astrophys. J.*, vol. 899, no. 1, p. 32, 2020, doi: 10.3847/1538-4357/ab9d8a.

[17] R. Ma *et al.*, "Improving open-circuit voltage by a chlorinated polymer donor endows binary organic solar cells efficiencies over 17%," *Sci. China Chem.*, vol. 63, no. 3, pp. 325–330, 2020, doi: 10.1007/s11426-019-9669-3.

[18] Y. Zhou, M. Eck, and M. Krüger, "Bulk-heterojunction hybrid solar cells based on colloidal nanocrystals and conjugated polymers," *Energy Environ. Sci.*, vol. 3, no. 12, pp. 1851–1864, 2010, doi: 10.1039/c0ee00143k.

[19] Z. Liu *et al.*, "Quenching Dynamics of Ultraviolet-Light Perception by UVR8 Photoreceptor," *J. Phys. Chem. Lett.*, vol. 5, no. 1, p. 69, Jan. 2014, doi: 10.1021/JZ402396K.

[20] R. Woods-Robinson *et al.*, "Wide Band Gap Chalcogenide Semiconductors," *Chem. Rev.*, vol. 120, no. 9, pp. 4007–4055, 2020, doi: 10.1021/acs.chemrev.9b00600.

[21] W. G. Lee, S. Chae, Y. K. Chung, W. S. Yoon, J. Y. Choi, and J. Huh, "Indirect-To-Direct Band Gap Transition of One-Dimensional V2Se9: Theoretical Study with Dispersion Energy Correction," *ACS Omega*, vol. 4, no. 19, pp. 18392–18397, 2019, doi: 10.1021/acsomega.9b02655.

[22] M. Stolterfoht, V. M. Le Corre, M. Feuerstein, P. Caprioglio, L. J. A. Koster, and D. Neher, "Voltage-Dependent Photoluminescence and How It Correlates with the Fill Factor and Open-Circuit Voltage in Perovskite Solar Cells," *ACS Energy Lett.*, vol. 4, no. 12, pp. 2887–2892, 2019, doi: 10.1021/acsenergylett.9b02262.

[23] T. P. A. van der Pol, K. Datta, M. M. Wienk, and R. A. J. Janssen, "The Intrinsic Photoluminescence Spectrum of Perovskite Films," *Adv. Opt. Mater.*, vol. 10, no. 8, pp. 1–7, 2022, doi: 10.1002/adom.202102557.

[24] M. E. Ramoroka, S. B. Mdluli, V. S. John-Denk, K. D. Modibane, C. J. Arendse, and E. I. Iwuoha, "Synthesis and photovoltaics of novel 2,3,4,5-tetrathienylthiophene-co-poly(3-hexylthiophene-2,5-diyl) donor polymer for organic solar cell," *Polymers*, vol. 23, no. 1. pp. 1–14, 2021. doi: 10.3390/polym13010002.

[25] T. T. Thao, D. N. Chung, N. N. Dinh, and V. Van Truong, "Photoluminescence Quenching of Nanocomposite Materials Used for Organic Solar Cells," *Commun. Phys.*, vol. 24, no. 3S1, pp. 22–28, 2014, doi: 10.15625/0868-3166/24/3s1/5073.

[26] K. J. Baeg *et al.*, "Polymer dielectrics and orthogonal solvent effects for high-performance inkjet-printed top-gated P-channel polymer field-effect transistors," *ETRI J.*, vol. 33, no. 6, pp. 887–896, 2011, doi: 10.4218/etrij.11.0111.0321.

[27] P. Held, "An Introduction to Fluorescence Resonance Energy Transfer (FRET) Technology and ... Page 1 of 8 An Introduction to Fluorescence Resonance Energy Transfer (FRET) Technology and ... Page 2 of 8," pp. 1–8, 2006, [Online]. Available: www.biotek.com

[28] S. Y. Park *et al.*, "Photophysical pathways in efficient bilayer organic solar cells: The importance of interlayer energy transfer," *Nano Energy*, vol. 84, no. December 2020, p. 105924, 2021, doi: 10.1016/j.nanoen.2021.105924.

[29] W. Zhu *et al.*, "Benign Pinholes in CsPbIBr2 Absorber Film Enable Efficient Carbon-Based, All-Inorganic Perovskite Solar Cells," *ACS Appl. Energy Mater.*, vol. 2, no. 7, pp. 5254–5262, 2019, doi: 10.1021/acsaem.9b00944.

[30] N. G. Leonard, S. W. Lee, D. W. Chang, J. M. Hodgkiss, and D. Vak, "Organic Photovoltaic New Renaissance: Advances Toward Roll-to-Roll Manufacturing of Non-Fullerene Acceptor Organic Photovoltaics," *Adv. Mater. Technol.*, vol. 2101556, 2022, doi: 10.1002/admt.202101556.

[31] B. Rajesh Kumar and T. Subba Rao, "AFM studies on surface morphology, topography and texture of nanostructured zinc aluminum oxide thin films," *Dig. J. Nanomater. Biostructures*, vol. 7, no. 4, pp. 1881–1889, 2012.

[32] J. Liu *et al.*, "5H-dithieno[3,2-b:2′,3′-d]pyran-5-one unit yields efficient wide-bandgap polymer donors," *Sci. Bull.*, vol. 64, no. 22, pp. 1655–1657, 2019, doi: 10.1016/j.scib.2019.09.001.

[33] L. C. Wouk De Menezes *et al.*, "Charge Transfer Dynamics and Device Performance of

Environmentally Friendly Processed Nonfullerene Organic Solar Cells," *ACS Appl. Energy Mater.*, vol. 1, no. 9, pp. 4776–4785, 2018, doi: 10.1021/acsaem.8b00884.

[34] M. E. G. Lyons, H. G. Fay, T. McCabe, J. Corish, J. G. Vos, and A. J. Kelly, "Charge percolation in electroactive polymer films," *J. Chem. Soc. Faraday Trans.*, vol. 86, no. 16, pp. 2905–2910, 1990, doi: 10.1039/FT9908602905.

[35] M. Bogdan, D. Brugger, W. Rosenstiel, and B. Speiser, "Estimation of diffusion coefficients from voltammetric signals by support vector and gaussian process regression," *J. Cheminform.*, vol. 6, no. 1, pp. 1–13, 2014, doi: 10.1186/1758-2946-6-30.

[36] J. Fischer *et al.*, "Density of states determination in organic donor-acceptor blend layers enabled by molecular doping," *J. Appl. Phys.*, vol. 117, no. 24, 2015, doi: 10.1063/1.4922587.

[37] W. Yang, Z. Ye, T. Liang, J. Ye, and H. Chen, "Facilitate charge transfer at donor/acceptor interface in bulk heterojunction organic photovoltaics by two-dimensional nanoflakes," *Sol. Energy Mater. Sol. Cells*, vol. 190, no. September 2018, pp. 75–82, 2019, doi: 10.1016/j.solmat.2018.10.003.

[38] P. Zhu and Y. Zhao, "Effects of electrochemical reaction and surface morphology on electroactive surface area of porous copper manufactured by Lost Carbonate Sintering †," 2017, doi: 10.1039/c7ra04204c.

[39] M. L. Tietze, K. Leo, and B. Lüssem, "Quantification of deep hole-trap filling by molecular p-doping: Dependence on the host material purity," *Org. Electron.*, vol. 14, no. 9, pp. 2348–2352, 2013, doi: 10.1016/j.orgel.2013.05.036.

[40] C. M. Proctor, M. Kuik, and T. Q. Nguyen, "Charge carrier recombination in organic solar cells," *Prog. Polym. Sci.*, vol. 38, no. 12, pp. 1941–1960, Dec. 2013, doi: 10.1016/J.PROGPOLYMSCI.2013.08.008.

[41] P. C. Application and M. E. Ramoroka, "NOVEL AROMATIC DENDRITIC-CO-POLY (3-," no. November, 2021.

[42] T. Orange, D. N. Ross, and P. C. Arendse, "The Nano-optimization of P- and E-type Semiconductor Films for Efficient Perovskite Photovoltaics," *Univ. West. Cape*, no. 8.5.2017, pp. 2003–2005, 2022.

[43] M. Jahandar *et al.*, "Highly efficient flexible organic photovoltaic modules for sustainable energy harvesting under low-light condition via suppressing voltage-drop by metal-mediated cross-linkable polymer interfacial layer," *Chem. Eng. J.*, vol. 448, no. June, p. 137555, 2022, doi: 10.1016/j.cej.2022.137555.

[44] B. R. Patil *et al.*, "Area dependent behavior of bathocuproine (BCP) as cathode interfacial

layers in organic photovoltaic cells," *Sci. Rep.*, vol. 8, no. 1, pp. 1–9, 2018, doi: 10.1038/s41598-018-30826-7.

Chapter 5 – Conclusions and Recommendations

5.1. Conclusions

In this study, we explored the potential application of a newly developed nanostructured material based on a D18 derivative (D18-RM) as a donor and Y6 as an acceptor to form a 3D bulk heterojunction (D18-RM:Y6) active layer. A substitution reaction of a halogenated-thiophene monomer with a stannane via Stille coupling reaction was utilized in the chemical synthesis of D18-RM polymer. NMR technique displayed anticipated peak signals and integration. However, the issue of C-13 not showing any peak signals is still a research gap. The red shift of the aliphatic C-C bond and the O-H stretch from FTIR analysis confirmed the success of Stille coupling synthesis as initially confirmed with NMR.

The XRD results revealed interesting crystalline peaks at for polymer D18-RM. Up to date, there has not been a reported crystalline polymer in this class of compounds. The polymer showed a good thermal stability under TGA, approximately 50% of the nanomaterial decompose at very high temperatures that are beyond 800 °C. This allows the use of D18-RM even at high temperatures without the wary of decomposition. When optical absorption was analysed to obtain information about maximum absorbance and optical band gap of D18-RM, Y6 and D18RM-Y6, a narrow optical band gap of 2.24 was achieved onset for donor polymer D18-RM. These findings were also confirmed using redox measurements from electrochemical CV.

The morphological analysis from SEM showed that the as synthesized donor polymer has a flake-like structures which can be easily deposited for fabrication. However, the results from AFM showed that the surface roughness is quite high although it still lies under Gaussian distribution, this potentially affected the OPV device thickness, which also affects the device performance. The results from TEM were mainly aimed at obtaining the particle size of the synthesized donor polymer since the focus was to synthesize a donor material that is nanostructured due to the benefits that comes with that characteristic. The redox measurements from CV were used as formal potential in the EIS analysis. All the Nyquist plots were first fitted using a suitable Randle cell prior to the analysis. After fitting charge transfer of 2383, 1663, and 2924 Ω was obtained, quite high for an OPV device.

The OPV device was and achieved a maximum PCE of 0.0022%, short circuit current (J_{SC}) of 21.04 mA/cm^2, fill factor (FF) of 27.7% and open circuit voltage (V_{OC}) of 0.024 V. This OPV was fabricated outside glovebox. Ag conductive paste that was used as metal contact can diffuse through the active layer and this will alter the semiconducting properties of a polymer.

The forward diffusion coefficient was calculated to be 0.0000786, 0.000656, and 0.0000409 cm^2/s, the reverse diffusion coefficient was calculated to be 0.0000638, 0.000780 and 0.0000377 cm^2/s for D18-RM, Y6 and D18RM-Y6, respectively. The exposure of the OPV device to air can result in active layer degradation and oxidation of the electrode. These factors explain why low PCE, and V_{OC} was achieved for D18-RM:Y6 OPV device.

Given its highly crystallinity structure and the other characteristics stated above, D18-RM may make a viable candidate for the role of an electron-donor in organic photovoltaic devices. The lowered optical band gap can also be attributed to photo-induced intramolecular charge transfer (ICT) process, which may be connected to the donor unit's high-lying HOMO and the acceptor unit's low-lying LUMO. This suggests that the designed nanostructured polymer is a potential n-type polymer material for making future OPVs.

5.2. Recommendations

In the absence of the dark characteristics, it is very difficult to infer about the OPV device characteristics, nominally one would expect that the device exhibits the asymmetric diode like behaviour in the dark. The molecular ordering, which is determined by crystallinity, has a considerable impact on the film optoelectronic properties as a result. As a matter of fact, much progress is required to develop highly ordered multipolymers that can result in higher levels of molecular organization and, thus, better crystallinity. In the continues effort to improve the performance of OPVs and eventually replace the current inorganic counterparts, the following aspects can add to the development of highly efficient OPV devices.

- The use of 2D carbon NMR can help in understanding the carbon-hydrogen interactions since C-13 does not give enough information about these types of compounds. 2D carbon NMR such as COSY, HSQC, HMBC etc. provides in depth information about carbon-carbon, carbon-hydrogen, and hydrogen-hydrogen interactions. This information can help to elucidate precise structures of the synthesized organic compounds.
- Small-angle X-ray scattering (SAXS) and wide-angle X-ray scattering (WAXS) are some of the techniques that can be employed to obtain size, shape, and arrangement of nanostructures and their macroscopic behaviour.
- The surface roughness from AFM of a fabricated OPV device should be kept low to avoid degradation of layers that also affects the morphology and ultimately the performance.
- After testing the efficiency of a fabricated OPV device, SEM analysis should be repeated to obtain the cross-section of the device that will give information about the arrangement of layers, and any diffusion process that could/has occurred.
- Due to the polymerization process that influences the necessary qualities of materials for PVs, gas permeation chromatography (GPC) should be used to study the molecular weight and polydispersity of the nanomaterial polymer.
- It was suggested that the use of silver paste in the OPV device fabrication enables high resolution electrode structures to be produced that exhibit both high electrical conductivity and low contact resistance. However, it was found to be problematic by diffusing into the active layer.